KATHOLIEKE UNIVERSITEIT LEUVEN

FACULTEIT WETENSCHAPPEN

DEPARTEMENT NATUURKUNDE & STERRENKUNDE

INSTITUUT VOOR KERN- EN STRALINGSFYSICA

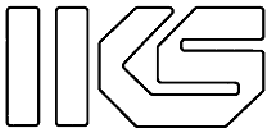

ELECTRON CAPTURE DELAYED FISSION OF ^{180}TL

door

Jytte Elseviers

Promotor:
Prof. Dr. Andrei Andreyev

proefschrift ingediend tot het
behalen van de graad van
master in de natuurkunde

2008-2009

Dankwoord

In de eerste plaats zou ik graag Mark Huyse en Piet Van Duppen willen bedanken om mij de mogelijkheid te geven een thesis te kunnen starten in de kernspectroscopiegroep en mij te introduceren in de boeiende wereld van het kernfysisch onderzoek. Concerning the latter, I should of course also thank my promotor Andrei Andreyev to give me the change to participate in the fascinating research of ECDF.

Further, I would like to give a big thank you to Dieter, Martin and Thomas to help me with all my problems I had concerning ROOT and the 'Ana.cc'-program. I really appreciate that you were always willing to explain me something or to help solve my problems, even if you did not have much time.

Ook alle andere leden van het IKS, en in het bijzonder deze van de kernspectroscopiegroep, die mee zorgden voor de ontspannen sfeer op het IKS, moeten vermeld worden. Kortom, het was me een waar genoegen om een thesis te kunnen voltooien in de kernspectroscopiegroep.

Er zijn echter ook een aantal mensen van buiten het IKS die ik niet mag vergeten. Hierbij denk ik eerst en vooral aan een aantal jaargenootjes die het voor mij plezierig maakten hier in Leuven te studeren. In het bijzonder wil ik hier Annelore en Nadia bedanken.

Verder zou ik ook graag Ellen, Katia en Annelore bedanken voor de fantastische reizen die we de voorbije twee zomers hebben gemaakt. Hopelijk mogen er nog veel volgen!

Ook mijn kotgenootjes van het voorbije jaar, Ellen, Katia, Katrien, Annelore en Christine, verdienen een vermelding voor de gezellige babbels en kookmomenten.

De vrienden van het thuisfront mogen ook niet vergeten worden, daarom bedankt allemaal voor de ontspannende avonden in het weekend.

Als laatste in dit rijtje, wil ik nog een speciaal woordje van dank richten tot Bart. Bedankt voor alle ontspannende en gezellige momenten, maar vooral bedankt om er steeds voor mij te zijn!

Tenslotte wil ik moeke en vake bedanken om mij de kans te geven in Leuven te kunnen studeren en om mij de voorbije vijf jaar altijd te blijven steunen.

Leuven - Sint-Mariaburg
Juni 2009

Samenvatting

Dit werk concentreert zich op het radioactief verval van de zeer neutronarme kern ^{180}Tl (Z = 81, N = 99), welke α-verval of elektronvangst kan ondergaan. Meer specifiek wordt de vervalwijze *elektronvangst-vertraagde-fissie* van ^{180}Tl onderzocht. Dit is een van de drie mogelijke vervalprocessen wanneer de meer algemene beta-vertraagde-fissie beschouwd wordt. In dit vervalproces ondergaat de kern, in dit geval ^{180}Tl, eerst een β-verval, hier elektronvangst, waarbij het een geëxciteerde toestand in de dochterkern, ^{180}Hg (Z = 80, N = 100), bezet. Als deze toestand een excitatie-energie heeft die vergelijkbaar of hoger is dan de fissiebarrière van de dochterkern, kan deze laatste met een eindige, detecteerbare waarschijnlijkheid fissie ondergaan. Dit zal gebeuren in competitie met gamma en/of deeltjes verval. Er zijn verschillende kernen in de U en Pb regio die, theoretisch gezien, deze elektronvangst-vetraagde-fissie kunnen ondergaan. Echter, tot voor het huidige experiment waren er slechts twaalf kernen gekend waarbij deze vervalwijze werkelijk werd geoberveerd.

Meerdere redenen maken het interessant om elektronvangst-vertraagde-fissie te bestuderen. Dit vervalproces maakt het bijvoorbeeld mogelijk om fissie-eigenschappen, zoals de vervalwaarschijnlijkheid of de totale kinetische energie, af te leiden voor exotische dochterkernen die niet vervallen via spontane fissie, en die ongewone N/Z verhoudingen hebben. Tot nu toe zijn deze fissie-eigenschappen enkel gekend voor kernen in de buurt van de β-stabiliteitslijn. Algemene eigenschappen van het beta-vertraagde-fissie proces, afgeleid uit de studie van elektronvangst-vertraagde-fissie, kunnen gebruikt worden in r-proces berekeningen. Verder kunnen schileffecten een belangrijke rol spelen. Zo werd verwacht dat de massaverdeling in de fissie van ^{180}Hg gedomineerd zou worden door de N = 50 schilsluiting, welke zou leiden tot een symmetrische massaverdeling. Dit werd echter niet geobserveerd!

Het experiment werd uitgevoerd aan de ISOLDE faciliteit in CERN. Om het radioactieve verval van ^{180}Tl te detecteren, wordt gebruik gemaakt van de zogenaamde *windmolen kamer*. De ^{180}Tl-bundel, komende van de massaseparator, wordt geïmplanteerd in een koolstoffolie. Dit is het implantatiestation. Tien van deze koolstoffolies zijn gemonteerd op een roterend wiel. Op het einde van een zogenaamde *supercyclus* wordt het wiel geroteerd naar het vervalstation, waar dan gekeken kan worden naar het verval van langlevende dochterkernen.

Om de energie van de α-deeltjes en fissiefragmenten, komende van het radioactief verval van ^{180}Tl en de dochter ^{180}Hg, te meten wordt gebruik gemaakt van twee silicium detectoren gepositioneerd tegenover elkaar op het implantatiestation. De langlevende activiteit van dochterkernen wordt gedetecteerd door ook twee silicium detectoren op het vervalstation te plaatsen. Verder wordt er buiten de kamer, op de positie van het implantatiestation, een Miniball Ge cluster geplaatst om γ-stralen te kunnen detecteren.

De eerste stap die genomen wordt in de analyse van de data is de kalibratie van de

gedetecteerde fissiefragmenten. Hierbij moet in eerste instantie aandacht geschonken worden aan het concept van *pulshoogte defect* (PHD) in halfgeleider detectoren. Dit effect zorgt ervoor dat de pulshoogte geregistreerd in een detector ten gevolge van een invallend zwaar ion, kleiner zal zijn dan de pulshoogte die gecreëerd wordt door een licht ion van dezelfde energie. Dit PHD kan in rekening gebracht worden met behulp van de Schmitt kalibratie methode, welke veronderstelt dat de geregistreerde pulshoogte in de detector ten gevolge van een inkomend fragment niet enkel afhankelijk is van de energie van het fragment maar ook van zijn massa. Met deze kalibratie methode kunnen dan de massa- en energieverdelingen van de fissiefragmenten berekend worden. Ook de totale kinetische energie van de fissie van ^{180}Hg kan bepaald worden. Deze resultaten zullen echter gecorrigeerd moeten worden voor het energieverlies dat de fragmenten ondergaan tijdens hun vlucht door de koolstoffolie. Verder zal ook het effect van een neutronemissie door een van de fragmenten op de massa- en energieverdelingen onderzocht worden.

In een tweede deel wordt de halfwaardetijd $t_{1/2}$ van ^{180}Tl bepaald. Deze kan berekend worden via het α-verval van ^{180}Tl, maar ook via de elektronvangst-vertraagde-fissie, vermits de fissie van ^{180}Hg, na elektronvangst van ^{180}Tl, kan aanzien worden als onmiddellijk.

Als laatste punt worden de elektronvangst vertakkingsverhouding b_{EC} van ^{180}Tl en de elektronvangst-vertraagde-fissie vervalwaarschijnlijkheid P_{ECDF} bepaald. Deze laatste zal vergeleken worden met de waarde die beschikbaar is in de literatuur.

Tenslotte zal dit werk afgesloten worden met een besluit over de uitgevoerde analyse van het radioactief verval van ^{180}Tl.

Summary

This thesis concentrates on the radioactive decay of the very neutron deficient nucleus ^{180}Tl (Z = 81, N = 99), which can decay through α decay or electron capture. More specific, the decay mode *electron capture delayed fission* of ^{180}Tl will be investigated. This is one of the three possible processes when the more general beta delayed fission is considered. In this decay process the nucleus of interest, here ^{180}Tl, first undergoes a β decay, in this case electron capture, whereby it populates an excited state in the daughter nucleus, ^{180}Hg (Z = 80, N = 100). If this state has an excitation energy comparable to or even higher than the fission barrier of the daughter nucleus, the latter may fission with a finite, detectable probability. This will happen in competition with gamma and/or particle decay. Several nuclei in the U and Pb region could, theoretically, undergo the electron capture delayed fission process. However, before the current experiment, only twelve nuclei were known in which this decay process was observed.

Different reasons make it interesting to study the electron capture delayed fission. This decay process permits for example to deduce fission properties, such as the decay probability or the total kinetic energy, of exotic nuclei that do not decay by spontaneous emission, and that have unusual N/Z ratios. Until now these properties are only known for nuclei in the vicinity of the β stability line. General features of beta delayed fission, deduced from the study of electron capture delayed fission, can be used in r-process calculations. Further, shell effects can play an important role. It was expected that the mass distribution of the fission of ^{180}Hg would be dominated by the N = 50 shell closure, which would lead to a symmetric mass distribution. This was however not observed!

The experiment was performed at the ISOLDE facility in CERN. To detect the radioactive decay of ^{180}Tl, the so-called *windmill chamber* is used. The ^{180}Tl beam, coming from the mass separator, is implanted in a carbon foil. This is the implantation station. Ten of these carbon foils are mounted on a rotating wheel. At the end of a so-called *supercycle* the wheel is rotated towards the decay station, at which the decay of long-living daughter nuclei can be registered.

To measure the energy of the α-particles and fission fragments, coming from the radioactive decay of ^{180}Tl and the daughter ^{180}Hg, two silicon detectors are used that are positioned across each other at the implantation station. The long-living activity of daughter nuclei is detected by also placing two silicon detectors at the decay station. Outside the chamber, at the position of the implantation station, a Miniball Ge cluster will be placed to be able to detect γ-rays.

The first step that will be taken in the analysis of the data is the calibration of the detected fission fragments. Initially, the concept of *pulse height defect* (PHD) in semiconductor detectors has to be explained. This effect accounts for the fact that the pulse height registered in a detector due to an incoming heavy ion is smaller than that of a light ion of

the same energy. This PHD can be taken into account by using the Schmitt calibration method, which assumes that the registered pulse height in the detector due to an incoming fragment does not only depend on the energy of the fragment but also on its mass. This calibration can then be used to deduce the mass and energy distributions of the fission fragments. Also the total kinetic energy of the fission of ^{180}Hg can be calculated. These results however have to be corrected for the energy loss the fragments suffer when they pass through the carbon foil. Further, the effect of one neutron emission by one of the fragments on the mass and energy distributions will be determined.

In a second part, the half-life $t_{1/2}$ of ^{180}Tl will be deduced. This can be done from the α decay of ^{180}Tl, but also from the electron capture delayed fission, since the fission of ^{180}Hg, after the electron capture of ^{180}Tl, can be treated as instantaneous.

As a final point the electron capture branching ratio b_{EC} of ^{180}Tl and the electron capture delayed fission decay probability P_{ECDF} will be deduced. The latter will be compared to the value that is present in the literature.

Finally, this thesis will end with a conclusion about the performed analysis of the radioactive decay of ^{180}Tl.

Contents

Chapter 1

Introduction

This chapter will start with a general introduction in nuclear structure, the basics of the nuclear shell model will be explained. Further, the different processes involving the decay of the nucleus of interest, ^{180}Tl, will be described. Finally, a short word will be said about the r-process.

1.1 Nuclear Structure

The atomic nucleus consists of positively charged protons and neutral neutrons, together these are often called the nucleons. The number of protons Z determines the place of the atom in the Periodic Table of Elements and thus the chemical element. A certain element can however have a variable number of neutrons N. Elements with the same proton number, but different neutron number are called isotopes. Therefore a nucleus is characterized by its charge Z and its mass number A (= N + Z), and is typically denoted by ^{A}X, where X is the chemical element. By considering the different number of protons and neutrons a Nuclear Chart can be built, in which the x-axis represents the number of neutrons and the y-axis the number of protons (see Fig. 1.1).

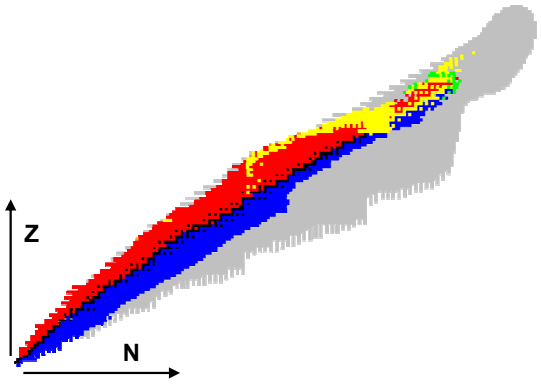

Figure 1.1: The Nuclear Chart [IKS09]. The different colors represent different decay modes (yellow: α decay, red: EC/β^+ decay, blue: β^- decay, green: spontaneous fission). The grey area are nuclei that are not yet observed but are theoretically predicted to exist.

The black squares in Fig. 1.1 represent the stable nuclei, which are said to lie on the *beta stability line*. This line follows the N = Z line for the light nuclei (up to about A = 40), while for the heavier nuclei the stability line bends over and the heavy nuclei will have more neutrons than protons. All other nuclei are radioactive. The different colors represent the different decay modes (α , EC/β^+ , β^- decay and spontaneous fission, see section 1.2). Nuclei far of stability, which thus have unusual N/Z-ratios, are often called *exotic* nuclei.

Since the Coulomb interaction causes a repulsive force to exist between the protons, another force has to be present to overcome this repulsion and keep the nucleons together. This force is the strong interaction, which is a short range interaction ($\sim 10^{-15}$ m). Besides the electromagnetic and strong interaction, also the weak interaction will be important, because this interaction is responsible for the radioactive β decay of nuclei (section 1.2).

The Hamiltonian describing the system of A nucleons has the general form:

$$H = \sum_{i=1}^{A} T_i + \frac{1}{2} \sum_{i,j=1}^{A} V_{i,j} \tag{1.1}$$

where T_i is the kinetic energy of the nucleons and $V_{i,j}$ is the two-nucleon interaction between nucleon i and j. To find the nuclear structure it suffices to solve the Schrödinger equation with this Hamiltonian. However, the exact potential of the strong interaction is not yet known, and thus the Schrödinger equation cannot be solved. Instead certain models have to be suggested from which the nuclear structure can be deduced. The most used model is the single-particle or shell model in which it is assumed that the nucleons move independently in an average potential caused by all the other nucleons. This approach is called a *mean field approximation*. The Hamiltonian can then be rewritten as

$$H = \underbrace{\sum_{i=1}^{A} (T_i + U_i)}_{H_0} + \underbrace{\frac{1}{2} \sum_{i,j=1}^{A} V_{i,j} - \sum_{i=1}^{A} U_i}_{H_1} \tag{1.2}$$

where U_i is the mean one-body potential [Hey90]. H_0 describes the movement of a single particle in the central potential U_i, independent of the other particles. The term H_1 takes the nucleon-nucleon interaction into account and is treated as a residual interaction. The Shrödinger equation can now be solved for H_0 by taking a certain shape for the potential U_i. This potential has to be determined as close to the real one as possible so that H_1 can indeed be treated as a small perturbation. Most often U_i is approximated by a harmonic oscillator, extended by an l^2-term, which makes the original (parabolic) potential resemble more a square well potential, and a spin-orbit $\vec{l} \cdot \vec{s}$-term. Solving the Schrödinger equation for this potential will result in discrete energy levels or *orbitals* (see Fig. 1.2). Since the nucleons are fermions, they need to fulfill the Pauli principle, which means a certain quantum state can only be occupied by one nucleon. Consequently, only a number of nucleons can fill a certain orbital. By filling the successive orbitals for the protons and neutrons separately, the ground state of a nucleus can be constructed. Nuclei can then be excited by moving one ore more nucleons to an orbital that is higher in energy than their ground state orbital.

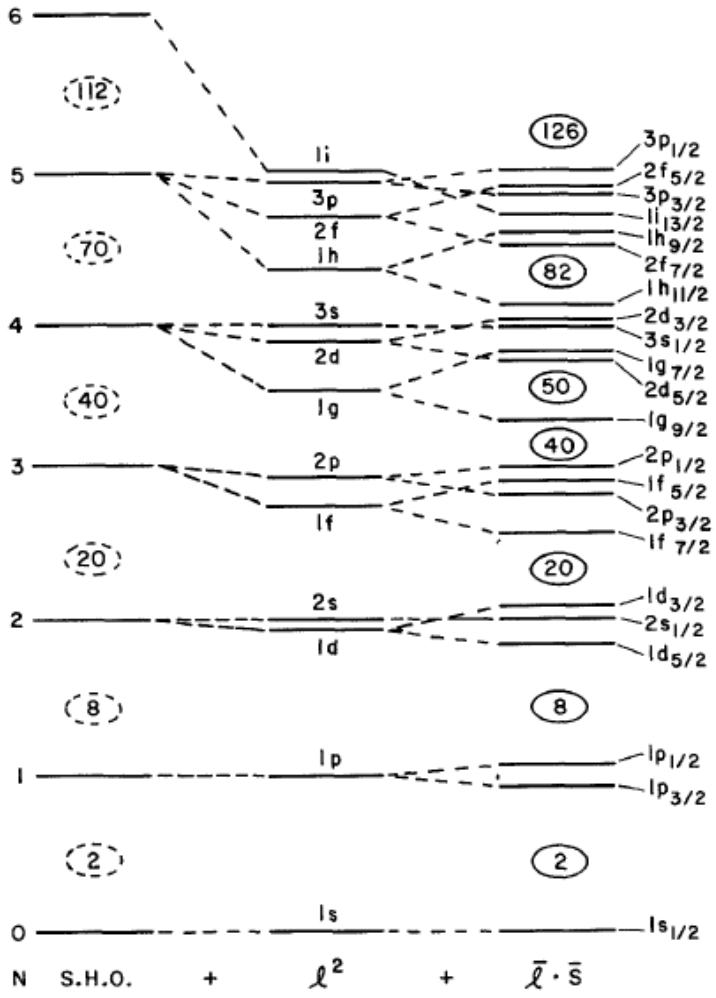

Figure 1.2: Energy states for a simple harmonic oscillator (SHO), an extended harmonic oscillator with an l^2-term and a realistic potential with l^2 and spin-orbit ($\vec{l}\cdot\vec{s}$) term [Cas90].

As Fig. 1.2 shows, the orbitals will be grouped in certain shells, with a rather large energy difference between the shells. This results in the so-called shell structure of the nuclei. At specific proton or neutron numbers (2, 8, 20, 28, 50, 82...), the *magic numbers*, a shell is completely filled and is then referred to as a *closed shell*. If the nucleus is magic in both proton and neutron number, it is called a *doubly magic nucleus*. Non-magic nuclei can then be considered as consisting of a closed core plus a number of *valence nucleons*.

The term H_1 describes the interaction between these valence nucleons, and will cause a shift in the energy levels of the shell model. The shell model gives good results as long as the number of valence nucleons is not too large, thus as long as H_1 remains a small perturbation. However, far from magic nuclei, this residual interaction will become more important and models where not only the valence nucleons, but rather all the nucleons are involved will probably give a better description of the nucleus. Furthermore, it is not yet known if the shell model is still a good description for exotic nuclei. In fact, it seems that the known magic numbers for N and Z depend on Z and N, respectively, such that certain

magic numbers can disappear and others appear far of stability. Therefore it is likely that the magic numbers will depend on the N/Z-ratio. This ratio is expressed through the quantum number isospin [Hey90].

In this work the exotic nucleus ^{180}Tl will be studied. In the following section this nucleus will be used to introduce the relevant radioactive decay processes, α and β decay and fission.

1.2 Decay of ^{180}Tl

The nucleus ^{180}Tl has 81 protons and 99 neutrons, thus it has one proton short to completely fill the Z = 82 shell. The orbitals where the unpaired proton and neutron will be in, cannot simply be read from Fig. 1.2, since this figure gives a more general diagram, which is too simplified. It is however known that the unpaired proton of the Tl nuclei will be in the $3s_{1/2}$ orbital [Fir99].

The N/Z ratio is equal to 1.22, hence ^{180}Tl is a very neutron deficient nucleus. It is positioned in the transition zone of the red region to the yellow region of the Nuclear Chart (Fig. 1.1), and therefore will decay through electron-capture (EC) or β^+ decay, in this case EC is dominant, and α decay. A schematic decay scheme of ^{180}Tl and the daughter ^{180}Hg, which results after EC of ^{180}Tl, is shown in Fig. 1.3.

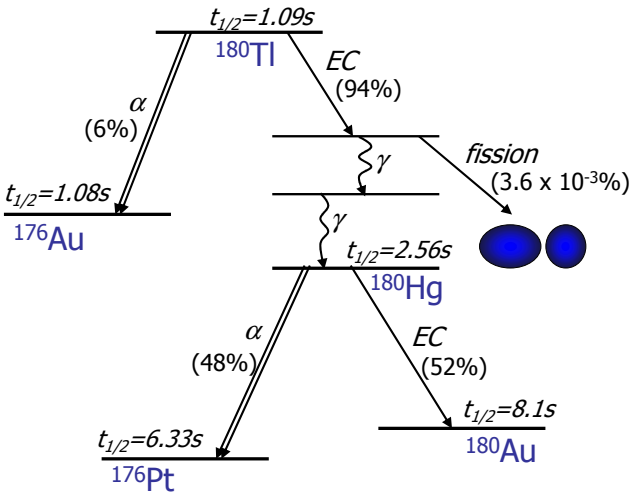

Figure 1.3: Schematic representation of the Decay of ^{180}Tl. The percentages in brackets are the branching ratios. No error bars are stated here, since the branching ratios and half-lives $t_{1/2}$ will be discussed in Chapter 5.

The figure shows that next to α decay and EC, there is also a small probability that the EC of ^{180}Tl results in the fission of ^{180}Hg, this is the *delayed* fission process. The main features of these three different decay modes will be discussed in the following sections.

1.2.1 Alpha Decay

When a nucleus undergoes an α decay, it emits an α-particle. This is actually a ^{4}He nucleus, thus consisting of two protons and two neutrons. The decay can be represented as follows:

$$^A_Z X_N \rightarrow ^{A-4}_{Z-2} X'_{N-2} + \alpha$$

The net energy released in the decay is called the Q-value and is given by the mass difference between the initial nucleus and the final nuclei:

$$Q = (m_X - m_{X'} - m_\alpha)c^2,$$

where e.g. m_X is the mass of isotope X and c is the velocity of light. The decay will only occur spontaneously if Q > 0 and the energy release in α decay will typically be of the order of 5 MeV. A striking feature of α decay, called the *Geiger-Nuttal rule*, is that α-decaying nuclei with large Q-values have short half-lives and vice versa [Kra88].

Many different final states in the daughter nucleus can be populated through the α decay. If the α decay leads to an excited state E*, the Q-value is given by

$$Q = Q_{ground} - E^*,$$

where Q_{ground} is the Q-value for decay to the ground state. Generally, the larger the Q-value, the larger the intensity to populate that final state. However, the intensity also depends on the wave functions of the initial and final states and on the angular momentum of the α-particle, namely through the centrifugal barrier. The larger the change in angular momentum between the initial and final state, the smaller the intensity to populate that final state and conversely, the smaller the angular momentum of the α-particle, the larger the intensity.

1.2.2 Beta Decay

The general name 'β decay' actually represents three types of nuclear decay processes:

- β^- decay in which a neutron is converted into a proton ($Z \rightarrow Z+1$, $N \rightarrow N-1$), together with the emission of an electron e^- and an anti-neutrino $\bar{\nu}$.

  $$^A_Z X_N \rightarrow ^A_{Z+1} X'_{N-1} + e^- + \bar{\nu}$$

  and

  $$Q_{\beta^-} = [m(^A X) - m(^A X')]c^2$$

- β^+ decay in which a proton is converted into a neutron ($Z \rightarrow Z-1$, $N \rightarrow N+1$) together with the emission of a positron e^+ and a neutrino ν.

  $$^A_Z X_N \rightarrow ^A_{Z-1} X'_{N+1} + e^+ + \nu$$

  and

  $$Q_{\beta^+} = [m(^A X) - m(^A X') - 2m_e]c^2,$$

  where m_e is the mass of the electron.

- Electron capture (EC) where also a proton is converted into a neutron. However, in this case an orbital electron is involved in the decay process, and thus, to fulfill conservation of charge, no positron but only a neutrino is emitted.

$$ {}^{A}_{Z}X_N + e^- \rightarrow {}^{A}_{Z-1}X'_{N+1} + \nu $$

and

$$ Q_{EC} = [m({}^{A}X) - m({}^{A}X')]c^2 - B_n, $$

where B_n is the binding energy of the captured electron.

The masses m in the Q-values are the atomic masses. It has to be noted that in the β decay processes the mass number A remains constant. The β^- decay will occur in neutron rich nuclei (the blue squares in Fig. 1.1), since by converting the excess of neutrons into protons, the nucleus will move to the beta-stability line while keeping A constant. The β^+ decay and EC will happen on the neutron deficient, proton rich side of the nuclear chart (red in Fig. 1.1), since, analog to the β^- decay, the nucleus will then move to the valley of beta stability.

Furthermore, as seen from the Q-values, there are nuclei were the EC process is energetically possible (Q $>$ 0), while the β^+ decay is not (Q $<$ 0), since for β^+ decay to occur the atomic mass difference must be at least $2m_e c^2 = 1.022$ MeV. In ^{180}Tl both decay processes are possible, but it is known that EC will be much more dominant ($>$ 95% intensity) than β^+ decay in heavy nuclei. Hence, the EC process is the decay of interest in this thesis. Due to the two-body final state in EC, the emitted neutrino will have a well-defined energy (*monoenergetic*). This in contrast to the three-body final state in $\beta^\pm$ decay, where two particles are emitted and thus where the neutrino (anti-neutrino) and the positron (electron) have a continuous energy distribution with a maximum energy of $Q_{\beta^\pm}$. The neutrino however is very hard to detect, hence another method has to be used to detect EC. This will be through emitted X-rays of the daughter nucleus. The captured orbital electron leaves a vacancy in the atomic shell. This vacancy will be filled by an electron coming from a shell that is higher in energy. X-rays will be emitted with an energy equal to the energy difference between the two involved shells.

As in the α decay, the larger the Q-value for the β decay to a specific final state, the larger the intensity to populate that final state. Furthermore, the so-called *allowed* decays are the most probable, these are the ones where the change in spin ΔI between the initial and final state is $\Delta I = 0, 1$ and no parity change $\Delta\pi$. The *forbidden* decays are less probable, but if for example π does change it must be a forbidden decay. The *first-forbidden* decays are those were $\Delta I = 0, 1, 2$ and there is a parity change. Similar the *second-forbidden* decays have $\Delta I = 2, 3$ and no $\Delta\pi$. In a similar way there are also third, fourth... order forbidden decays, but these are very unlikely since the higher the order of forbidenness the less probable the decay. The forbidden decays are mostly to weak to observe unless these are the only possible decay modes [Kra88].

1.2.3 Fission

Fig. 1.3 shows that with some, very low, probability the excited daughter nucleus ^{180}Hg, produced after EC of ^{180}Tl, can fission. The sequence of the EC of ^{180}Tl and fission of the daughter ^{180}Hg is the Electron Capture Delayed Fission phenomenon, which is the subject of this thesis and which will be explained in the next chapter. However, it is important to first discuss some general features of the fission process.

In the nuclear fission process, the nucleus decays into two fragments of comparable mass. This decay process is the result of the competition between the strong force and the Coulomb force in heavy nuclei, since the Coulomb repulsion ($\propto Z^2$) increases more rapidly than the nuclear binding energy ($\propto A$). Through this decay process, the total binding energy strongly increases, hence a lot of energy will be released (∼200 MeV in the actinide nuclei). However, the Coulomb barrier inhibits the fission process and therefore the *spontaneous* fission will only become important for nuclei with A > 250. The fission can also be *induced* by particles, such as neutrons or photons, whereby excited states are populated which are high enough in energy to overcome the barrier or to penetrate it [Kra88].

The fission barrier B_f is schematically drawn in Fig. 1.4. If an excited state is produced with an energy in the vicinity of the fission barrier height the nucleus can decay through fission, in competition with γ decay to the ground state or particle decay, whereby a particle such as a neutron or proton is emitted. In the spontaneously fissioning nuclei the energy released through the fission process is only just less than the Coulomb barrier energy, and hence the fragments can successfully tunnel through the Coulomb barrier. Spontaneous fission can then happen, in competition with other decay modes.

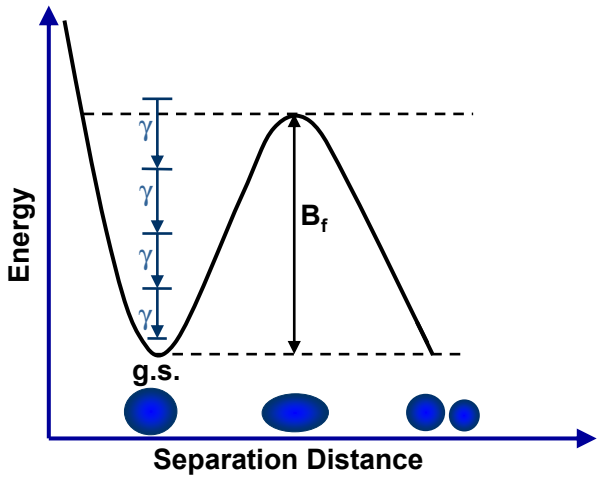

Figure 1.4: Schematic view of the fission barrier B_f (g.s. = ground state).

The two fragments resulting from fission will not always have the same mass, instead a mass distribution will be observed, which can be symmetric or asymmetric. In the symmetric case, the mass distribution is centered around one mean value (≈ A/2, with A the mass of the fissioning nucleus, if neutron emission is disregarded (see further)). In the asymmetric mass distribution, in general a lighter and heavier fragment will result, as such that the mass distribution consists of a so-called double-humped structure (see Fig. 1.5(b)). Moreover, in the fission process the N/Z ratio is conserved, and since for the heavy fissioning nuclei N ≫ Z, the two fission fragments will be very neutron rich. This can result in the prompt emission of one or more neutrons at the instant of fission (within 10^{-16} s). The number of emitted neutrons ν is not fixed but shows a distribution and depends on the fragment mass, see for example [Ter62].

In general, the masses of the fission fragments will be largely determined by shell effects. This is illustrated in Fig. 1.5(a), which shows the average light and heavy masses of the

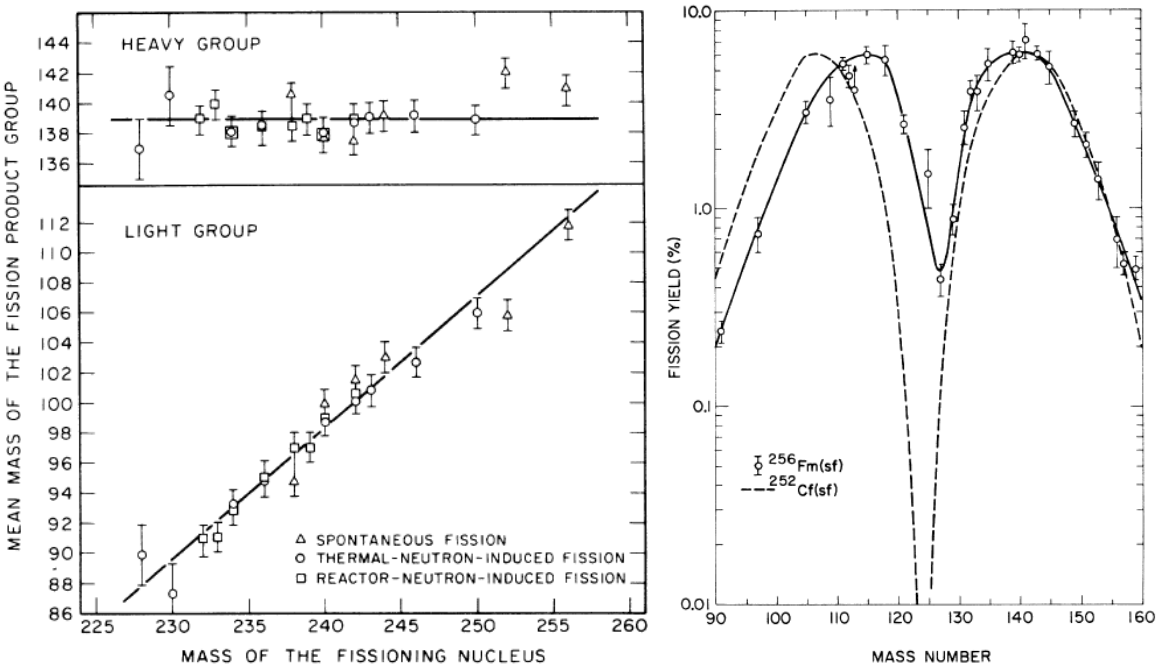

(a) (b)

Figure 1.5: (a) Average masses of the heavy and light fragment groups as a function of the mass of the fissioning nucleus. (b) Example of the double-humped structure in the asymmetric spontaneous fission of ^{256}Fm and ^{252}Cf [Fly72].

fragments over a mass range of A = 228 to 256 of the fissioning nucleus. A striking feature is that the average heavy fragment mass stays nearly constant around A $\approx$ 138-140, while the average light fragment mass increases linearly as A of the fissioning nucleus increases (see also Fig. 1.5(b)). This can be explained by taking the shell model into account. The heavy fragment mass distribution is situated around the shell closures Z = 50 and N = 82, which results in a very stable configuration. For the light fragment group there is not such an overlap with a shell closure, and consequently it will not be affected much by shell closures. Therefore, the average mass of the heavy fragment group will stay nearly constant and that of the light fragment group will increase as A of the fissioning nucleus increases.

Fig. 1.6(a) gives the different deformations the nucleus undergoes in the fission process and in Fig. 1.6(b) the time scale of the fission process is shown. When the fissioning nucleus passes the saddle in the potential energy surface (see Fig. 1.4), the fission becomes an irreversible process. It takes then about 2.2-6 $\times$ 10^{-21} s to reach the scission point. This is the point where the nucleus breaks into two fragments. 90% of the total kinetic energy of the fragments is reached within 10^{-20} s. As shown on the time scale it can be assumed that the prompt neutrons are emitted, after a time of about $10^{-17,18}$ s, from fully accelerated fragments, thus having their maximum kinetic energy [Wag91].

(a)

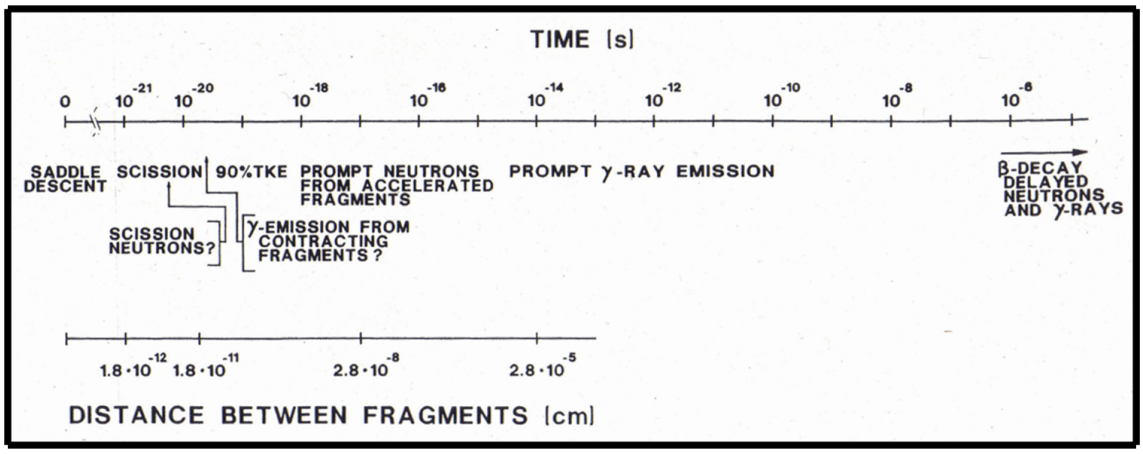

(b)

Figure 1.6: (a) Nuclear shapes in the fission process: ellipsoidal deformation, formation of the neck between the fragments and finally the rupture of the neck with two fission fragments as the result. (b) The fission process as a function of time [Wag91].

1.3 R-Process

After the Big Bang, of all the chemical elements only hydrogen en helium were present in the universe, next to small abundances of some light nuclei. The heavier nuclei have to be produced through nuclear reactions (*nucleosynthesis*). This will occur in the interior of stars through fusion of the light elements. These are exothermic reactions, since the nuclear binding energy per nucleon increases by going to heavier nuclei. Nevertheless, the binding energy per nucleon reaches a maximum for ^{56}Fe, which means that energy is required to produce heavier elements than iron by fusion. The fusion to heavier nuclei than iron is thus not possible in stars. Another obstacle to go to the heavier elements is the Coulomb barrier. With increasing charge (Z) of the nucleus the Coulomb barrier will rise, and at high enough Z the Coulomb barrier will inhibit the occurrence of nuclear reactions induced by charged particles.

Only nuclear reactions involving the capture of neutrons are then possible to produce the heaviest elements. There are two main neutron capture process, the (slow) s-process and the (rapid) r-process. By capturing neutrons, neutron rich nuclei will be produced. The more exotic these nuclei are, the shorter the mean lifetime t_β to undergo β decay. The time scale t_n in which a neutron will be captured depends on the neutron flux. If a neutron is captured, but the available neutron flux is low, the time scale t_n to capture another neutron is larger than t_β and the produced nucleus will most probably first decay, before capturing a new neutron. Therefore, the produced nuclei will stay close to the stability line. This is the s-process and will not be discussed further.

In the r-process the neutron flux is so high ($\sim 10^{22}/\mathrm{cm}^2\mathrm{s}$) that a number of neutrons can be captured before the produced nuclei will β decay ($t_n < t_\beta$), and thus very neutron rich

nuclei are produced [Cow91, Cow04]. This is the process of interest and is schematically drawn in Fig. 1.7. When the high neutron flux stops, the produced heavy nuclei will β decay to the beta stability line, and as such the stable nuclei heavier than iron can be produced. To understand and determine the path of the r-process nuclear studies have to be performed on the very neutron rich nuclei.

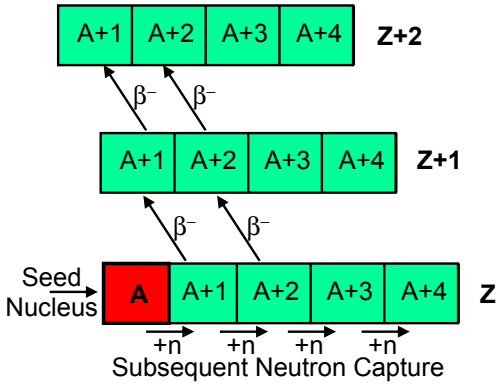

Figure 1.7: Schematic representation of the r-process.

The required high neutron fluxes will occur in stars with a mass larger than eight solar masses at the end of their life when they explode as a supernova. When these stars have completed the production of iron by fusion, there will be no more energy from nuclear reactions to balance the gravitational force. Consequently, the star will collapse, which causes a strong temperature increase. Due to the high temperature the photons will receive a high energy, high enough to start the photo-dissociation of the nuclei. This will eventually result in a mixture of protons, neutrons and electrons. However, due to a high density increase, the protons and electrons can combine to form neutrons

$$p + e^{-} \rightarrow n + \nu$$

The resulting release of energy in the form of neutrinos ν will provide the expulsion of the outer layers located around the neutron-core. This is the supernova explosion. Right before and during this explosion the r-process takes place [Aer06].

Chapter 2

Electron Capture Delayed Fission

In this chapter the phenomenon of Electron Capture Delayed Fission (ECDF) will be explained. First, a general introduction in the beta delayed fission process will be given. Subsequently, the regions where it can occur and the experimental evidence for beta delayed fission will be clarified. Finally, the reasons for studying ECDF will be discussed.

2.1 Beta Delayed Fission

Beta delayed fission is a rare decay process in which a parent nucleus first undergoes a β decay (β^+/EC or β^-), whereby it populates an excited state in the daughter nucleus. If this excited state has an energy comparable to or even higher than the fission barrier of the daughter nucleus, the latter may fission with a finite, detectable, probability. This will happen in competition with gamma and/or particle decay. The electron capture delayed fission will happen on the neutron deficient side of the nuclear chart, while the β^- delayed fission will occur on the neutron rich side. Fig. 2.1 shows a schematic diagram of ECDF, which is the case of interest in the experiment discussed in this thesis.

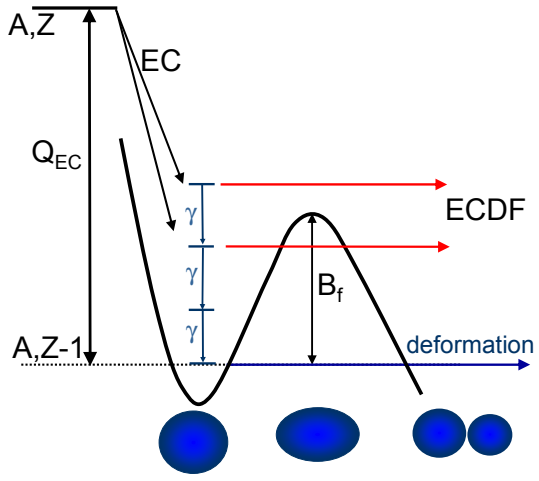

Figure 2.1: Simplified view of the ECDF process: A nucleus decays by EC, whereby it populates an excited state in the daughter nucleus which may then fission.

ECDF can only occur if, of course, the branching ratio for electron capture, b_{EC}, of the parent nucleus is different from zero and, more important, if the total Q-value for EC ,Q_{EC}, of the parent nucleus is comparable to or greater than the fission barrier, B_f, of the daughter nucleus. Only if the latter condition is met, a certain branch of the EC decay can populate excited states in the daughter nucleus, from which fission can occur (see Fig. 2.1). A number of nuclei in the Pb and U region fulfill these conditions [Ber69] (for experimental evidence see section 2.2). Typically, the populated excited states in the daughter nucleus only have an energy in the order of a few MeV. This makes ECDF an ideal process to study low energy fission in the region of nuclei that do not decay by spontaneous fission, far outside the region of the beta stability line. Because of these low excitation energies, it is expected that the shell effects will play an important role.

The probability for ECDF to occur, P_{ECDF}, is determined as the ratio of the number of nuclei that undergo electron capture followed by delayed fission, N_{ECDF}, to the total number of electron capture decays, N_{EC}.

$$P_{ECDF} = \frac{N_{ECDF}}{N_{EC}} \tag{2.1}$$

P_{ECDF} depends strongly on Q_{EC} of the parent nucleus and B_f of the daughter nucleus. The larger Q_{EC} or the smaller B_f, the larger P_{ECDF}. More precisely, the value Q_{EC}-B_f is important, the larger this is, the larger P_{ECDF} (see Fig. 2.3 below).

2.2 Experimental Evidence

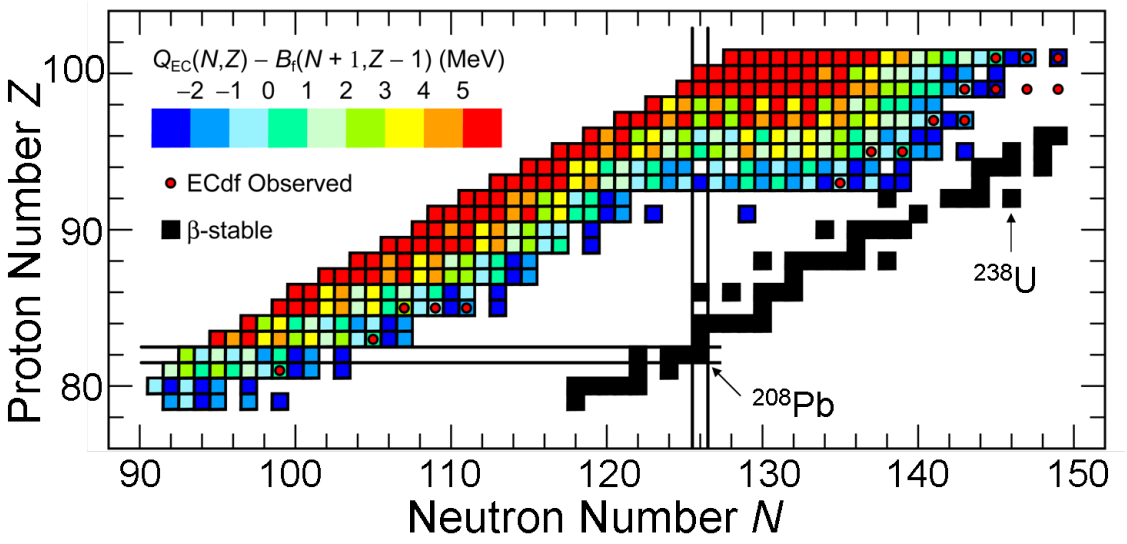

Figure 2.2: Region of the nuclear chart where ECDF would be possible based on an energy window of the Q_{EC}-B_f value [Möl08a] (Q_{EC} values from [Möl95], B_f values from [Möl08b].

As mentioned above a number of nuclei in the U and Pb region should, theoretically, be able to undergo the ECDF decay process. These nuclei are shown on the nuclear chart in Fig. 2.2, where the color code gives the value for Q_{EC}-B_f, the larger this value the larger the probability for ECDF to occur (if of course $b_{EC} > 0$). The diagram also shows the

nuclei were ECDF has already been observed (the dots). However, the observed ECDF could not be unambiguously addressed to those nuclei in all the cases. In the U region, there are only about ten cases where the observed ECDF decay process could certainly be addressed to the right nuclei. These nuclei are ^{228}Np, ^{232,234}Am, ^{242,244,246,248}Es, ^{238,240}Bk and ^{250}Md and have a low ECDF probability in the range of 10^{-6}-10^{-2} (see Fig. 2.3) [Gal83, Gan80, Hal90a, Hal90b, Kre94a, Kre94b, Sha00, Sha01, Sha02]. These low values suggest the sub-barrier nature of the ECDF decay process in the actinide nuclei. In the Pb region, in only three of the five cases the ECDF process was certainly observed (see further).

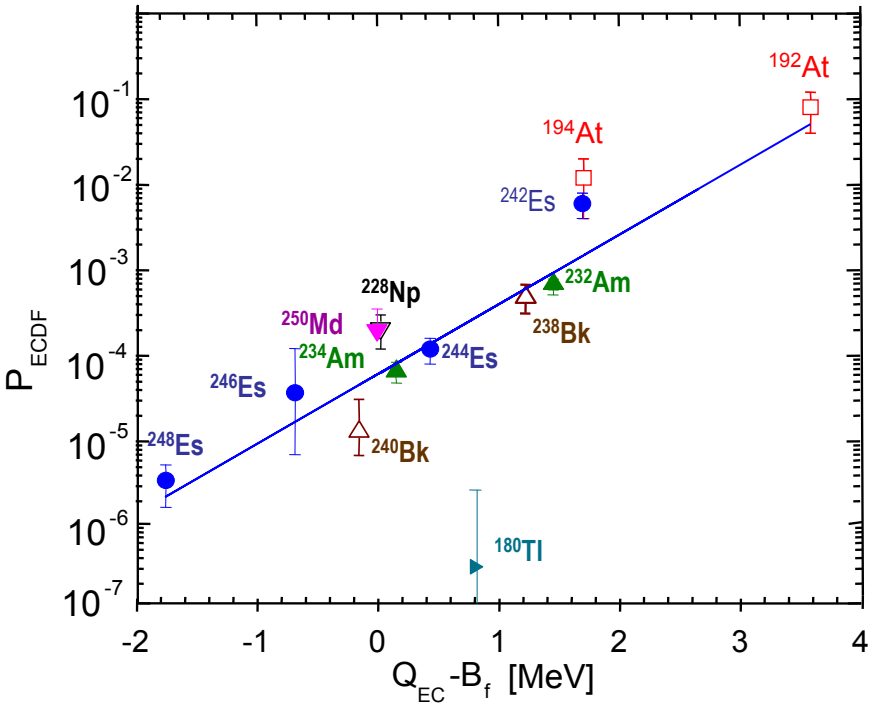

Figure 2.3: ECDF probability P_{ECDF} as a function of (Q_{EC}-B_f). The data are marked by the parent nuclei. The Q_{EC} values are taken from [Möl95] and the B_f values from [Mey99].

Fig. 2.3 shows the ECDF probabilities of the measured data as a function of the Q_{EC}-B_f difference. From the figure it follows that the P_{ECDF} values approximately lie on a straight line. This trend shows that P_{ECDF} increases exponentially with the increase of the Q_{EC}-B_f value (with the exception of ^{180}Tl, see below). This strong dependence makes the ECDF studies a very promising method to deduce fission barriers of very exotic nuclei, see e.g. [Sta90].

If it is possible to find nuclei with Q_{EC}-B_f = 3-4 MeV, P_{ECDF} values of several 10% could be found! In the actinide region relatively low values of Q_{EC} ~3-5 MeV are found, which then causes low (or even negative) values of Q_{EC}-B_f. These thus lead to low P_{ECDF} values. In the very neutron deficient Pb region, however, much higher Q_{EC} values of the order of 10 MeV are expected, which can lead to Q_{EC}-B_f differences of a few MeV and thus to much higher P_{ECDF} values.

The first experimental evidence for ECDF was found for the isotopes ^{232,234}Am in 1966 in Dubna [Kuz66]. In 1987, a successful experiment in which ECDF was observed in the Pb region was carried out [Laz87]. The authors of [Laz87] suggested that the observed ECDF found its origin in the decay of ^{180}Tl. However, an unselective production and identification method used in the experiment did not allow an unambiguous identification of A and Z of the produced nuclei. Therefore, only the *most probable* fissioning nucleus could be suggested. As such, the observed ECDF was assigned to the decay of ^{180}Tl, which was then produced in the reaction ^{40}Ca + ^{144}Sm $\rightarrow$ ^{180}Tl + p3n. A very low value of $P_{ECDF} = 3\times10^{-7\pm1}$ was deduced. This value does not fit the general trend of the P_{ECDF} values as a function of the Q_{EC}-B_f difference observed for the actinide region, as is shown in Fig. 2.3. Two possible reasons for this discrepancy have been suggested in [Laz87]: a different shape of the fission barrier in the actinide nuclei compared to the Pb region and the possible presence of a beta-delayed proton and alpha emission branch in the very neutron deficient nuclei in the Pb region. It has to be noted however, that in the calculation of the P_{ECDF} value an absolute production cross section of ^{180}Tl of σ_p = 0.1-1 mb was *assumed*. This value is in contradiction with modern calculations and estimations, which show that the cross section will be in the order of 2 μb [Anda], thus a factor of 50-500 lower than that was assumed. The recalculated P_{ECDF} would then be $P_{ECDF} = 1.5\times10^{-5}$-$1.5\times10^{-4}$. This value would fit the general trend in Fig. 2.3 very well. Further, next to ^{180}Tl, the authors of [Laz87] suggest that the ECDF can also happen in the nuclei ^{196}At and ^{188}Bi, but no P_{ECDF} values were deduced for these nuclei.

The first unambiguous measurement that showed that the ECDF decay process can also occur in the Pb region was performed by Andreyev et al. (paper to be published [Andb]). In this experiment the ECDF of the nuclei ^{192,194}At was measured. The P_{ECDF} value of these nuclei as a function of the difference Q_{EC}-B_f follows the general trend in Fig. 2.3. For ^{192}At the highest ever value of $P_{ECDF} = 0.08(6)$ was deduced. The ECDF process is also expected to occur in other nuclei of the Pb region, possible parent-daughter pairs are shown in Fig. 2.4.

These figures show that the more neutron deficient nuclei are, the higher the Q_{EC} value and the lower the B_f value, thus the higher P_{ECDF}. The staggering in the Q_{EC} value is also significant, this is due to the odd-even effect of the masses. This effect can be understood by the fact that even Z and even N nuclei are more stable than their odd-even or odd-odd neighbors. If an odd-odd nucleus undergoes EC, it will become an even-even nucleus, with a much larger binding energy, and thus larger stability and smaller mass, which leads to a higher Q_{EC}-value. An odd-even nucleus that undergoes EC stays however an even-odd nucleus, and thus the increase in binding energy will not be that large. This results in a lower Q_{EC}-value compared to its odd-odd neighbors. This is also the reason why ECDF will not occur starting from an even-even nucleus. Through the EC decay the even-even nucleus will become an odd-odd nucleus, which has two unpaired nucleons, and this will result in a low Q_{EC}-value.

Finally, it is well-known that nuclei with unpaired particles, thus odd-mass and odd-odd nuclei, have a higher fission barrier, or thus longer half-life than the even-even neighboring nuclei [Wag91]. Therefore, in the ECDF decay, the even-even daughter nuclei will be more fissile than the odd-mass daughters. These two arguments show that the neutron deficient odd-odd nuclei in the Pb region are more probable to show a detectable ECDF branch in their decay. The regions of interest are those with an EC branching ratio $b_{EC} > 1\%$ and for which (Q_{EC}-B_f) $\gtrsim 0$. It follows that a measurable ECDF branch is

expected for ^{178,180}Tl, $^{184-188}$Bi, $^{192-194,196}$At and $^{200-202}$Fr. In this thesis the ECDF of ^{180}Tl will be investigated.

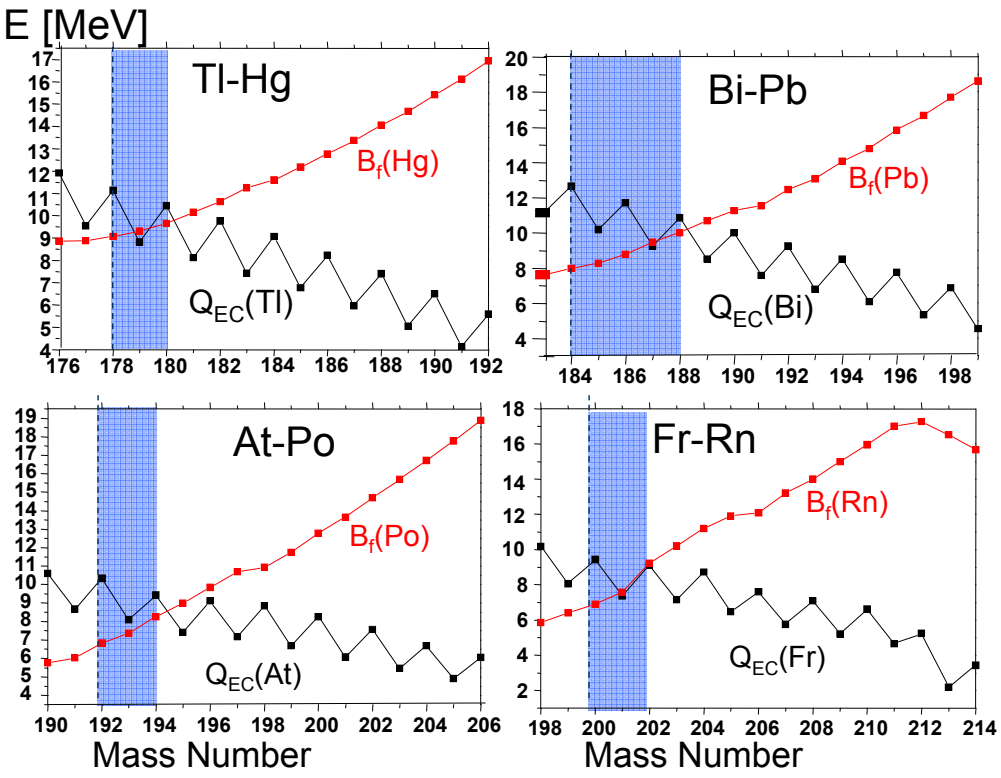

Figure 2.4: Q_{EC} values ([Möl95]) of the parent nucleus and B_f values ([Mey99]) for the daughter nucleus as a function of mass number. The regions in which ECDF is expected to be measurable are shown by the grey rectangles. The left border is determined by $b_{EC} < 1\%$.

2.3 Why study Beta Delayed Fission?

There are a number of reasons why it is interesting to study beta delayed fission. First of all, it is believed that β^- delayed fission, together with neutron induced and spontaneous fission, plays an important role in the r-process [Ber69, Pan05]. That is in the termination of the r-process, the fission recycling and production of the super heavy elements (Z > 92) [Cow91]. Due to the low excitation energy of the daughter in β^- delayed fission, the shell effects might still play an important role. This is important for the understanding of the super heavy elements (SHE), since these can only exist if shell effects are taken into account. If only the liquid drop model is considered, the fission barrier of the super heavy elements is zero, and thus these SHE could not exist.

The path of the r-process on the nuclear chart and a diagram of the fission recycling process is shown in Fig. 2.5. The most probable explanation for the termination of the r-process is fission (β^- delayed, neutron induced or spontaneous). The r-process can

continue until a mass A $\gtrsim$ 250, before fission occurs with a high probability. The fission fragments will then have a mass A/2 $\approx$ 125, and can be used again as a seed nucleus in the r-process. This is the fission recycling process.

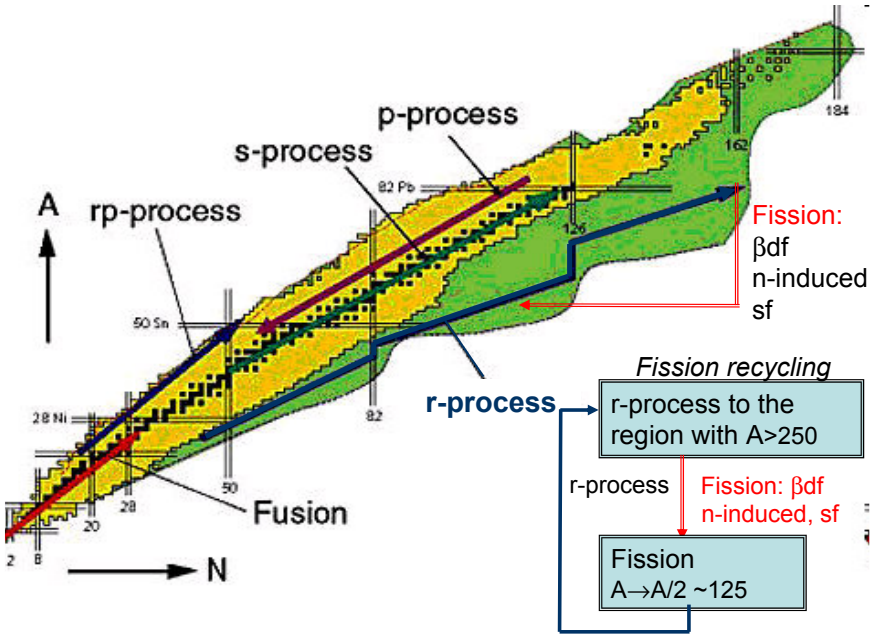

Figure 2.5: Visualization of the r-process on the nuclear chart and diagram of the fission recycling process [Nor09].

This r-process will only occur on the neutron rich side of the nuclear chart, this is the region where β^- delayed fission occurs. Therefore, to study the r-process it is desired to study nuclei which undergo β^- delayed fission. However, these extremely neutron rich nuclei are presently not available in the experimental facilities. The necessary fission data, such as e.g. fission barrier heights, could then be deduced from theoretical models. These models for the fission barrier heights, B_f, agree well with the available B_f values from experiment (see Fig.2.6), but deviate much from each other for nuclei on the neutron deficient and neutron rich side of the nuclear chart. Hence, the fission data from theoretical models for the very exotic nuclei are not reliable. The alternative is then to study the ECDF in neutron deficient nuclei in the Pb region, which are available. From these ECDF experiments general features of the beta delayed fission can be deduced, which could then be used in r-process calculations.

Further, ECDF, or beta delayed fission in general, allows to study fission properties (e.g. decay probability, fission barrier height, mass/charge distribution, total kinetic energy, gamma and neutron multiplicities) of exotic daughter nuclei which do not decay by spontaneous fission, and which have unusual N/Z ratios. Until now, fission barriers and fission properties are known only in the vicinity of the beta stability line, at which typical values for the N/Z ratio are ~1.59 (for ^{238}U) or ~1.54 (^{208}Pb) (see Fig. 2.6). ECDF, however, gives access to nuclei with very exotic N/Z ratios. As an example, the N/Z ratio for ^{180}Hg, the fissioning nucleus of interest, is only N/Z = 1.25. These unusual ratios could lead to unexpected properties, cold fission (no neutrons are emitted in this fission

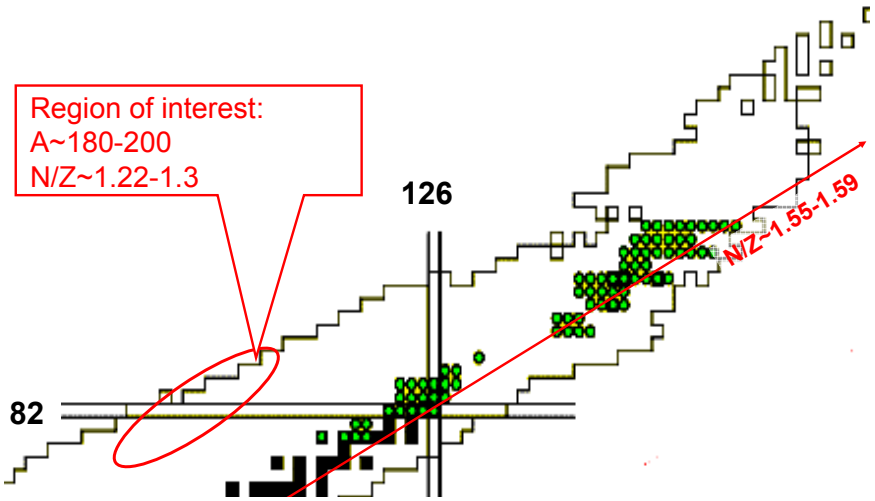

Figure 2.6: Region of the nuclear chart in the Pb-U region. The dots indicate the presently available fission barrier data ([Ref06]).

process), unexpected mass/charge distributions...

In the heavier nuclei it is known that the low energy fission is dominated by an asymmetric mass distribution, in which the shell closures Z = 50 and N = 82 play an important role. In the case of the ECDF of ^{180}Tl however, it is expected that the fission mass distribution will be dominated by the N = 50 shell closure. This would lead to nuclei in the vicinity of the (N = 50, Z = 40) region, such that the N/Z ratio of the fissioning nucleus, ^{180}Hg, is conserved. A *symmetric* mass distribution situated around the nucleus ^{90}Zr would thus be observed. This symmetric fission however is not what is measured in the fission of ^{180}Hg! This is described in Chapter 4.

Furthermore, as mentioned above, the theoretical models for the fission barrier heights, B_f, deviate from each other outside the valley of beta stability. The B_f values for some exotic nuclei can however be deduced with good precision from the ECDF process. Finally, the isospin dependence of the fission barriers can be studied more precisely, since ECDF gives access to exotic nuclei with exceptional N/Z ratios, and thus with large isospin values.

Chapter 3

Experimental Setup

The ECDF experiment was carried out at the ISOLDE facility in CERN. This chapter will deal with the experimental setup that was used. In the first section, general information will be given on CERN and the ISOLDE facility. Further on, details will be given about the experimental set up, especially about the detection chamber, time structure of the detected signal and detectors used. Finally, the data acquisition, which was carried out with digital electronics, will be discussed.

3.1 The ISOLDE Facility

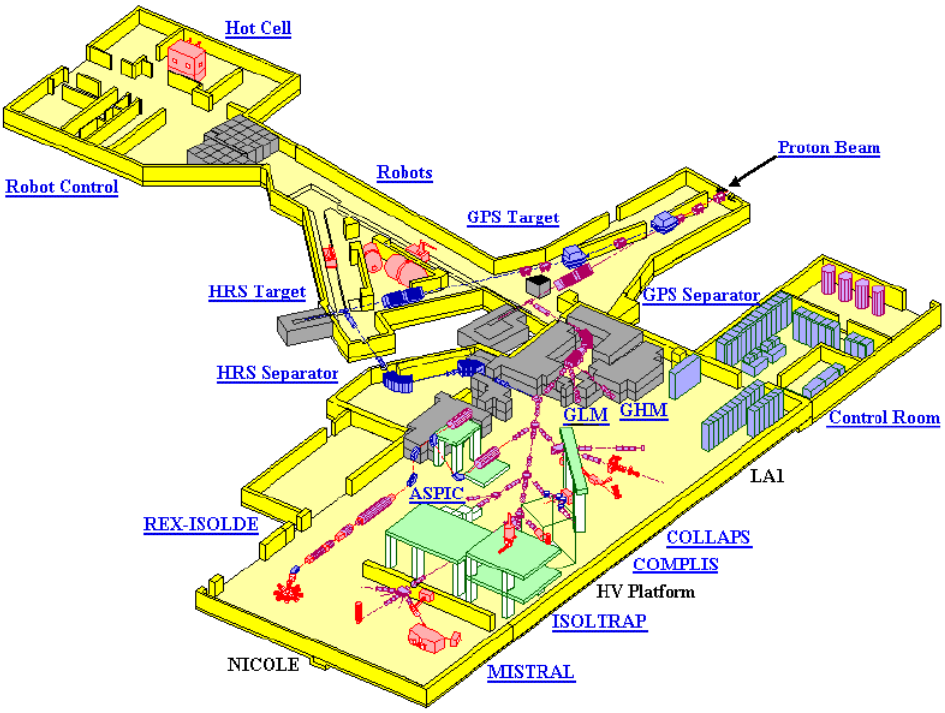

Figure 3.1: Layout of the ISOLDE facility at CERN [ISO09].

The ISOLDE facility [Kug00] is an on-line mass separator located at CERN (European Organization for Nuclear Research), which can deliver a wide variety of radioactive ion beams for different experiments in, for example, nuclear, atomic, surface and solid-state physics. A schematic overview of ISOLDE is shown in Fig. 3.1.

The radioactive nuclei of interest are produced by proton induced nuclear reactions. The protons have an energy of 1.4 GeV and the proton beam has an average intensity of 2.1 μA. They are delivered by the Proton-Synchrotron-Booster (PS-Booster), which is formed by four small synchrotrons. The proton beam consists of pulses that are 2.4 μs in length and have a period of 1.2 s. Those pulses can then be distributed among the different facilities of CERN. A sequence of 21 pulses is grouped into a so-called *supercycle*. The maximum number of protons per pulse equals 3.2×10^{13}.

These protons induce fission, spallation and fragmentation in the target material. The choice of target material depends on the desired radioactive isotopes, and is chosen as to maximize the production of the desired isotopes. In the case of the current experiment a UC_x target was used. The thallium nuclei are predominantly formed by spallation of the uranium in the target.

After the production of the radioactive nuclei, they diffuse out and effuse from the target material and drift to an ion source through a heated transfer line. To reduce diffusion, desorption (e.g. from the walls of the target chamber) and effusion times, the target-ion source is kept at high temperature of the order of ~2300 K. Since the desired (exotic) radioactive nuclei are mostly produced in a cocktail of much more abundantly produced isotopes, the ionization process has to be as selective as possible. There are three main ionization methods, surface ionization (suitable for elements with a low ionization potential), ionization by electron impact (suitable for elements with a high ionization potential) and resonant laser ionization. The latter was used in this experiment, and therefore only this method will be discussed (see section 3.1.2).

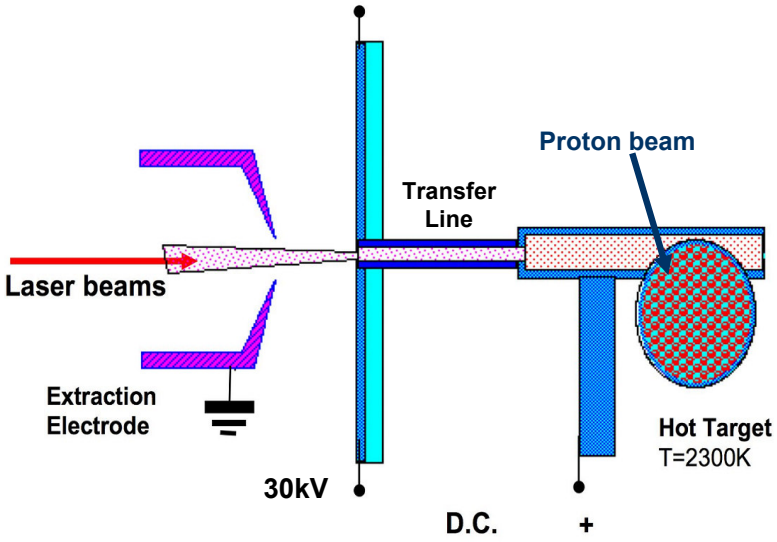

Figure 3.2: Schematic representation of the target-ion source at ISOLDE using resonant laser ionization [ISO09].

After the ionization the radioactive isotopes are extracted from the target-ion source by using extraction electrodes. The ion source is kept at high voltage (30 kV), while the extraction electrodes are kept at ground potential, as such that the produced ions are accelerated to 30 keV. A schematic picture of the complete target-ion source is shown in Fig. 3.2.

After acceleration, the ions are mass separated in the High Resolution Separator (HRS) or the General Purpose Separator (GPS). The former is used in the case of the Tl nuclei and has a mass resolving power $\Delta m/m$ of 5000. After the mass separation the isotopes are ready to be used in a certain experiment.

3.1.1 Time Profile

Since the proton beam consists of consecutive pulses, the ion beam will have a certain time structure as well. The diffusion, effusion and ionization processes take a certain amount of time, thus, when leaving the target-ion source, the ion beam will not form sharp pulses, but will be spread out in time. The release time profile defines the so-called *release curves*, of which a schematic drawing is shown in Fig. 3.3. The shape of the release curves depends heavily on the chemical element, and can be for example rather narrow, as in the case of Tl nuclei, which means the ions will be released fairly fast. For Tl 90% of the ions will be released within 2.5 s.

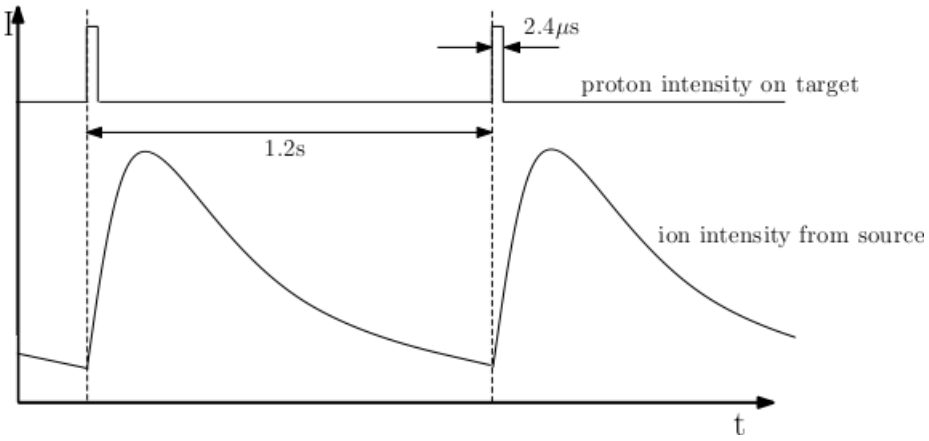

Figure 3.3: Schematic time structure of the proton and ion beam.

3.1.2 Resonant Laser Ionization

By using a *resonant laser ionization ion-source* (RILIS) [Fed00] a highly element selective ionization process can be obtained. This ionization method uses lasers of different wavelength to stepwise excite and eventually ionize a specific element by using different atomic transitions (see Fig. 3.4, for the case of Tl [Fed03]).

Since these atomic transitions are element specific, only the desired element will be ionized. However, due to the high temperature of the target-ion source, isotopes with low ionization potential will be ionized as well through surface ionization and can form an isobaric contamination of the beam. Nevertheless, this will not be a problem for the lightest Tl nuclei, such as ^{180}Tl, because, except for ^{180}Tl itself, there are no isobaric

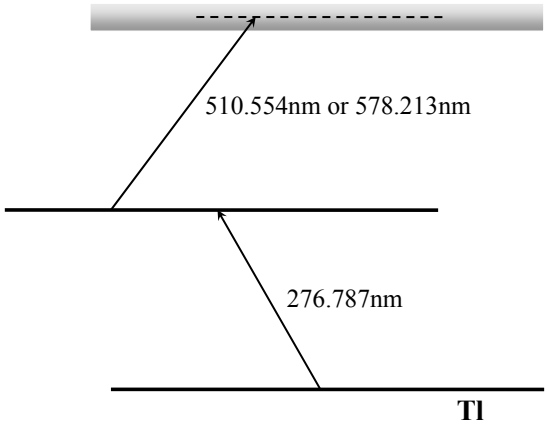

Figure 3.4: Resonant Laser Ionization of Tl.

isotopes that can be surface ionized with high enough intensity. For the heavier Tl nuclei however, a strong contamination due to surface ionized Fr will be present. Using RILIS, an ionization efficiency of 27% can be reached for the Tl nuclei [Fed03].

3.1.3 Yield of ^{180}Tl

The yield that can be reached at ISOLDE for ^{180}Tl equals 6.1×10^2 ions/μC or, assuming a current of 2.1 μA, 1.281×10^3 ions/s, when using a 50 g/cm^2 UC_x target. However, the measured average production rate for ^{180}Tl in the current experiment was only $\sim$200 ions/μC. A possible cause for this low yield was a problem with the beam transmission through the ISCOOL setup, a radiofrequency quadrupole cooler, at the HRS beam line. According to a measurement, the maximal transmission efficiency through the cooler was $\sim$70%.

3.2 Windmill Chamber

To detect the radioactive decay, fission fragments and α-particles, of the ^{180}Tl beam, the so-called windmill chamber is used [Den92]. A schematic representation of this system is shown in Fig. 3.5. The incident beam, coming from the separator, is implanted in a 20 μg/cm^2 or 888 Å thick carbon foil. This makes the foil thin enough so that the α-particles suffer only a small energy loss, as such to obtain a good α-energy resolution. Of course, the fission fragments will, because of their higher mass, lose more energy and this will anyway result in a lower energy resolution.

Ten of these carbon foils are mounted on a rotating wheel. The wheel is rotated by using a step motor, which takes 200 steps to rotate over 360°. By rotating this wheel over 144° or 80 steps the implanted radioactivity can be transported from the implantation station to the decay station. The time necessary to rotate the wheel is approximately 1 s. This suggests that in the case of the Tl beam, most of the decay will already happen in the implantation station, because of the relatively short half-life of about 1 s (section 5.1). During a measurement only five of the carbon foils are used. After a certain measurement it is then possible to move to the other five carbon foils. As such, any long-living radioactivity

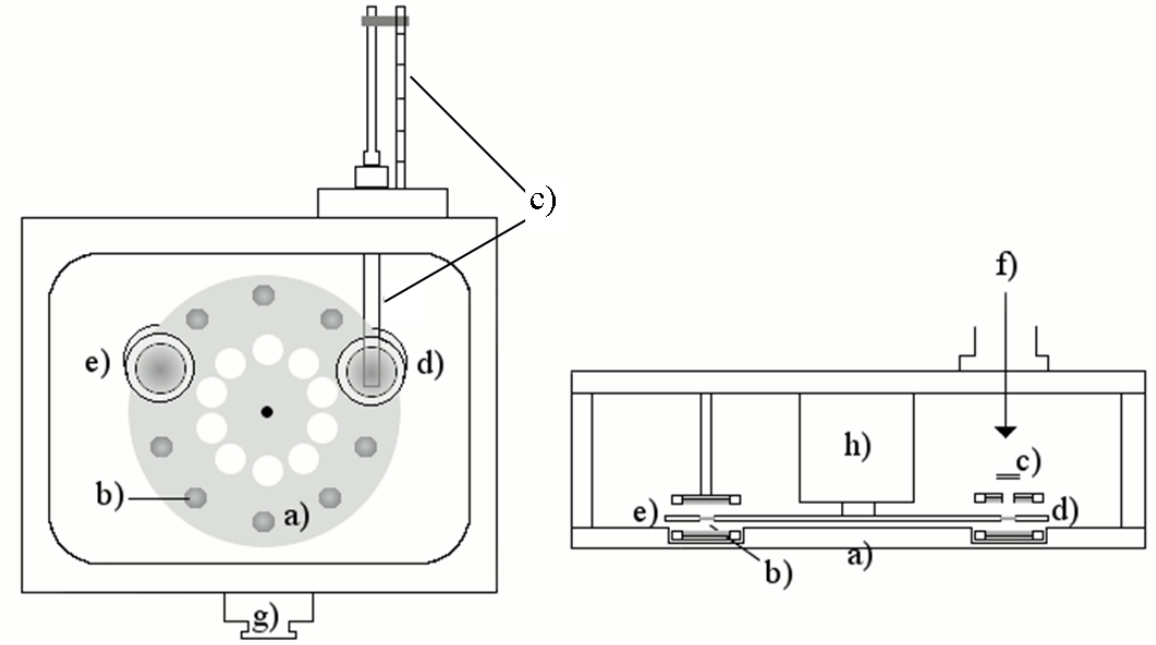

Figure 3.5: The windmill system (left: top view, right: side view): (a) rotating wheel, (b) carbon foil, (c) current measurement and collimator, (d) implantation station (with two silicon detectors), (e) decay station (with two silicon detectors), (f) separator beam, (g) pumping hole (to obtain vacuum), (h) step motor [Coc].

will have the time to decay.

The focussing of the separator beam onto the carbon foils is performed with the help of a collimator with three different holes of diameter 2, 4 and 6 mm, and a metal plate on which the transmitted beam is measured. To achieve the best focussing, the current measured on the collimator should be minimal and on the metal plate maximal, so that the full separator beam intensity is transmitted through the collimator and implanted into the carbon foil.

3.2.1 Time Structure

As mentioned in section 3.1, one supercycle consists of 21 subsequent proton pulses, giving a total time for the duration of one supercycle of 25.2 s (the proton pulses have a period of 1.2 s). The half-life $t_{1/2}$ of ^{180}Tl is about 1 s (see section 5.1) and this will determine the time structure of the measurement. Therefore, the idea is now to use two subsequent proton pulses for the production and implantation of ^{180}Tl. The mass separator (HRS) will then be opened for about 2.4 s, thus an extra 1.2 s after the second proton pulse has arrived. This to give the Tl nuclei the time to diffuse out of the target-ion source. Hence, nuclei will be implanted in the carbon foil for a time of approximately 2.4 s. During and after the implantation the radioactive decay will be measured for several seconds or about two or three half lives of ^{180}Tl. After this time, again two proton pulses are given and the nuclei are again implanted for about 2.4 s, and so on.

Different groups of such two subsequent proton pulses were received during the experiment. As an example, during roughly 11.5 hours the proton pulses 2-3 and 10-11

were given. The measured growth (implantation of ^{180}Tl) and decay (radioactive decay of ^{180}Tl) curves for these sequence of proton pulses are shown in Fig. 3.6. This curve is for one specific α decay branch of ^{180}Tl, namely the α decay which has an energy of $E_\alpha = 6.35$ MeV. In the figure the growth curves of the two subsequent proton pulses are clearly shown, as also the decay curves.

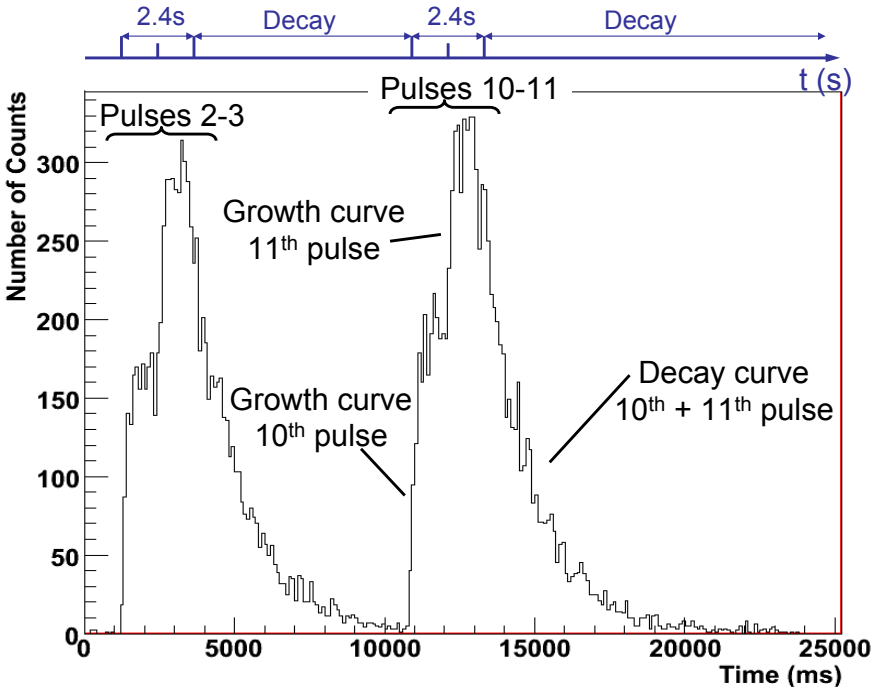

Figure 3.6: Growth and decay curves for the proton pulses 2-3 and 10-11.

After one supercycle is elapsed, the wheel is rotated to the decay station, where it is possible to look at the left-over activity of ^{180}Tl and at the decay of long-lived daughters. However, since the half-life of ^{180}Tl is only of the order of 1 s, most of the Tl nuclei will have already decayed at the implantation station. This is why it is important to be able to detect as many particles as possible at the implantation station. Therefore, two detectors are put at the implantation station, as well as a Miniball Ge cluster (see next sections). After rotation of the wheel, nuclei can be implanted into a new foil and the cycle can be restarted.

3.2.2 Particle Detectors

In total four particle detectors will be used, two at the implantation station across each other and two at the decay station, also across each other (see Fig. 3.7(a)). The advantages of positioning the detectors like this are:

- Increase in geometric efficiency (both for alpha particles and fission fragments), since more particles can be detected.
- Fission fragments can be measured in coincidence: a fissioning nucleus will always emit two particles in opposite directions, assuming the decaying nucleus is at rest

(conservation of momentum). Thus, a fission event should leave a signal in both detectors (see Fig. 3.7(b)). If both fission fragments can be detected, one can assign a total energy to the fission event, namely the sum of the energy of the two fragments, the so-called Total Kinetic Energy (TKE).

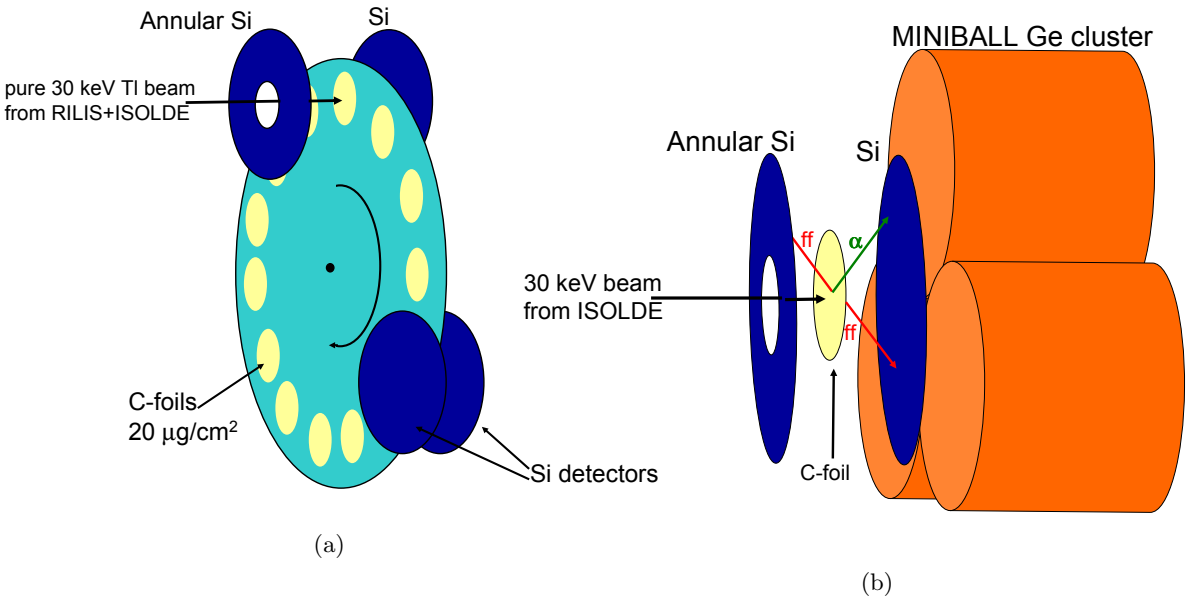

Figure 3.7: (a) Position of the particle detectors (dark blue) in the wind mill chamber. (b) Position of the gamma detectors (orange) outside the wind mill chamber. Not shown is the fourth gamma detector perpendicular to the figure.

Alpha particles and fission fragments can be distinguished by their energies. The alpha particles, in this experiment, will have energies of the order of 5 MeV, while fission fragments can have energies ranging from 40 MeV to 120 MeV. It is the aim to measure energies of both fission fragments and alpha particles, thus detectors that can cope with the large energy difference between both kind of particles are necessary. Silicon detectors are suitable for this purpose.

In the experiment two silicon detectors from Canberra [Can09] and two from Ortec [Ort09] are used. The Canberra detectors are Partially Depleted Passivated Implanted Planar Silicon (PIPS) detectors. They have an active area of 300 mm^2 and a warranted alpha energy resolution of 15 keV. One of the Ortec detectors is a Totally Depleted Silicon Surface Barrier detector and also has an active area of 300 mm^2 and has a warranted alpha energy resolution of 20 keV. The other Ortec detector is an Annular Partially Depleted Silicon Surface Barrier detector. It has a circular hole in its center with a diameter of 6 mm and will be referred to as the annular detector. This hole is necessary to allow nuclei to be implanted into the foil (see Fig. 3.7(a)). As a consequence of this hole the detector is a bit larger and has an active area of 450 mm^2. Also, because of the larger size (thus, larger capacitance and electronic noise), the warranted alpha energy resolution is a little worse, 25 keV. The alpha resolutions in all detectors are measured for the alphas of energy 5.486 MeV of ^{241}Am.

The annular detector and on of the Canberra detectors are positioned at the implantation station. The Canberra detector is placed at a distance of about 4 mm from the carbon foil. The annular detector can on the one hand not be placed too close to the carbon foil, since then all the decay products will fly through the central hole and will not be detected, but on the other hand it can also not be placed too far from the carbon foil, since then the solid angle will be too small. The optimal distance to place the annular detector was found to be 4 mm, but due to limitations in the experimental setup it was placed at about 7 mm. Taken together, both detectors at the implantation station cover a solid angle of 51% of 4π. The other two detectors are positioned at the decay station, the Canberra detector is on the same side of the wheel as the annular detector.

Silicon Detectors

The silicon detectors consist of a junction between a p-type and n-type semiconductor. The contact between these two types of material causes the diffusion of conducting electrons out of the n-type material into the p-type material, where they combine with holes, and similar for the holes of the p-type material. This diffusion results in the emergence of a so-called *depletion region*. This region can be extended by applying a reverse bias. The resultant electric field across the depletion region causes the collection of any electron-hole pairs created by an incident charged particle, since the electrons will be swept back to the n-type material and the holes to the p-type material [Kno00]. The number of electron-hole pairs created will be proportional to the energy of the incident particle.

Silicon Surface Barrier Detector A production scheme of this type of detector is shown in Fig. 3.8(a). In general silicon is used as the n-type material, on which a thin gold layer is deposited as the p-type contact. Aluminum is used at the back of the detector as the ohmic contact.

Passivated Implanted Planar Silicon Detector This type of detector uses implanted contacts, instead of the surface barrier contacts (see Fig. 3.8(b)). Multiple detectors can be made simultaneously, starting from a large silicon wafer. Typically, the leakage current in this type detector will be much lower than in the Surface Barrier detectors.

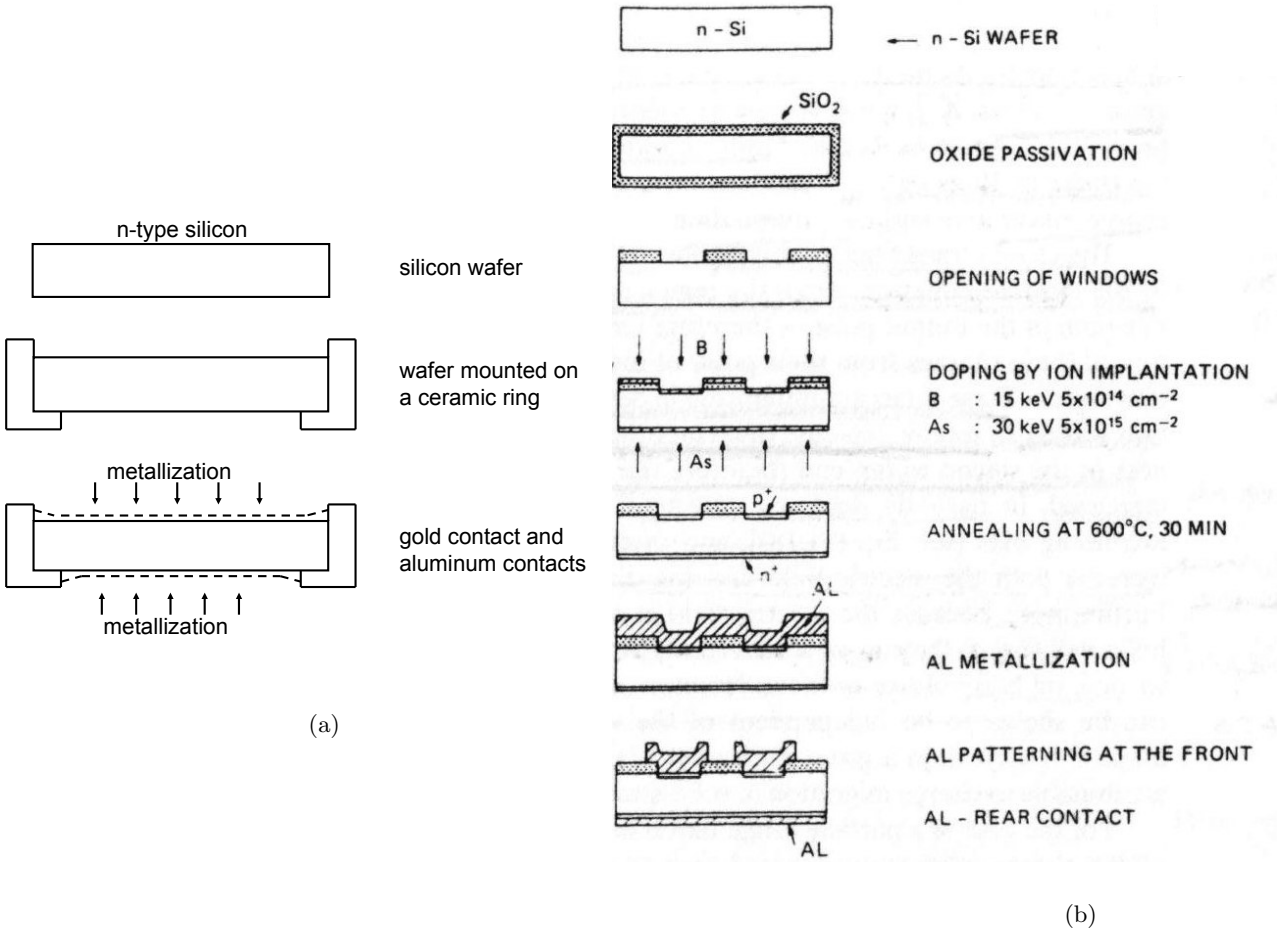

Figure 3.8: Production scheme of (a) a Silicon Surface Barrier detector [Ort09] and (b) a Pasivated Implanted Planar Silicon detector [Kno00].

3.3 Gamma Detectors

Outside the chamber, at the position of the implantation station, a Miniball Ge cluster detector is positioned (see Fig. 3.7(b)), to detect the gamma rays. Perpendicular to this Ge cluster another germanium detector, a planar low-energy X-ray detector, is placed. As such, fission-gamma coincidences and alpha-gamma coincidences can be measured, from which the decay products could be identified.

Such a Miniball Ge cluster [Ebe01] consists of three Hyper Pure Germanium (HPGe) crystals (see Fig. 3.9), each segmented in six parts. Each segment can be read out separately, which enables the determination of the position where the incident gamma ray hit the detector. This segmentation was however not used in the current experiment, and will not be discussed (more information can be found in [vdW06, Dir07]). Thus, in this experiment the cluster is only used as three separate gamma detectors.

The working principle of the Ge detectors is the same as for the silicon detectors, the incoming gamma ray will create electron-hole pairs through which it looses its energy. The number of pairs is again proportional to the gamma energy.

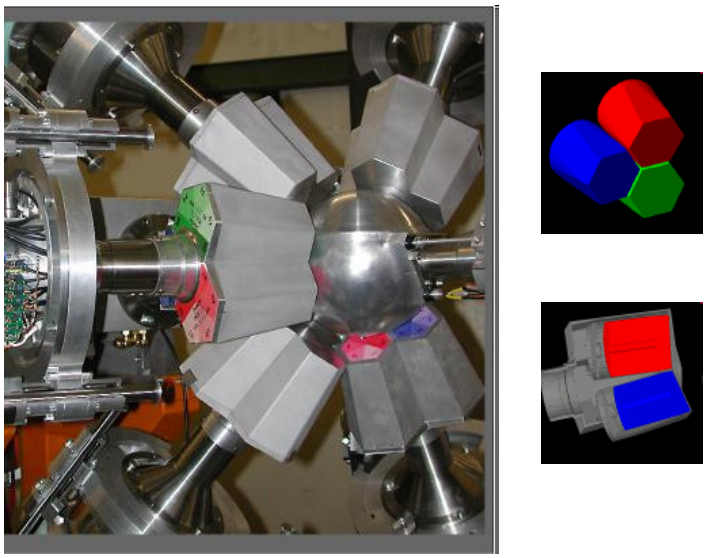

Figure 3.9: Miniball clusters (left) and the three (encapsulated) crystals of one cluster (right) [MIN09].

3.4 Electronic System

Analog or digital electronics [War00] can be used in the detection setup of the experiment. A schematic view of both setups for the case of the silicon detectors is shown in Fig. 3.10. The figure shows that both analog and digital electronics need a preamplifier for every silicon detector. The germanium detectors do not need a separate preamplifier, because these are already built in the detectors itself. Thus, in total four preamplifiers are necessary. Beside this similarity between both possible setups, there will be several advantages of using digital instead of analog electronics.

Analog Electronics The ADC (Analog to Digital Converter) used in analog electronics contains a maximum of 8192 channels. If the broad energy range of alphas and fission fragments would have to be processed by a single ADC, the energy per channel would be very large (about 15 keV per channel), which is not desirable for α-particles. Consequently, the signal coming from the preamplifier should have to be split. As is shown in Fig. 3.10, this means that two amplifiers, two ADC's and a timing logic would be necessary for every detector. Hence, the electronics system would be very complicated. Furthermore, the splitting of the signal will result in a large loss in energy resolution.

Digital Electronics If one uses digital electronics [X-r09], the electronic system will be much simplified. Only one digital module (*Digital Gamma Finder*, DGF) will be necessary, as is shown in Fig. 3.10. The DGF modules have a wide dynamical range from about 100 keV up to 200 MeV (in one module 65000 channels are available). Thus, one can use one channel of the DGF simultaneously for alpha particles and fission fragments. Further, every DGF module contains four channels, one for each detector. Also, one does not need separate amplifiers, because the amplification can be adjusted for each detector separately, within the program which is used to read out the data from the detectors.

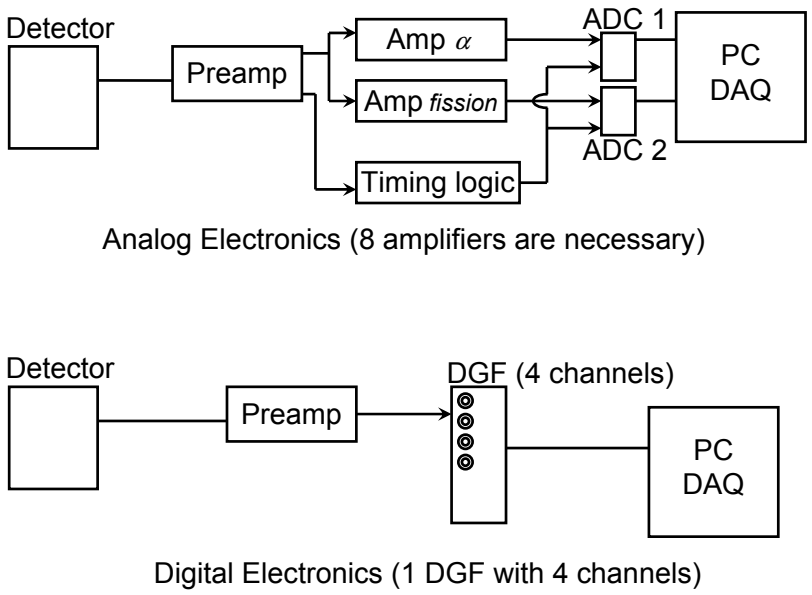

Figure 3.10: Schematic view of the difference in detection setup for the silicon detectors, using analog or digital electronics.

Tests performed by the author of this work showed that the energy resolution obtained with digital electronics is comparable to the one obtained with analog electronics. Therefore, because of the much simpler electronic setup and the comparable energy resolution, the digital electronics are used in the current experiment. Thus, in total four preamplifiers and two DGF modules were used, one for the four particle detectors and one for the four gamma detectors.

Chapter 4

Data Analysis of the Fission Events

This chapter will deal with the calibration and further analysis of the fission events measured with the experimental setup described in the previous chapter. It is important to make a distinction between singles, where only one of the fragments resulting from the fission of ^{180}Hg was detected, and coincident events, where both fragments were detected. If the so-called single events are considered, then *all* fission fragments are taken into account, and thus all the detected fragments are treated as being independent of each other. Therefore, in the single events both the singles and coincident events are included.

In total 1111 fission fragments were detected, of which 346 in coincidence. Thus, 419 (= 1111 - 2 × 346) times only one of the fragments of the fission was observed. The total amount of registered fissions is therefore equal to 765.

In the first section the concept of pulse height defect (PHD) in semiconductor detectors will be explained and will be concentrated on the calibration procedure, namely the Schmitt calibration method. Next, results obtained with this calibration method will be presented, namely the mass and energy distributions of the fragments. Finally, these distributions will be adjusted by correcting them for the energy loss the fragments suffer by moving through the carbon foil and for the possible neutron emission of the fragments.

4.1 Schmitt Calibration Method

Next to several advantages, such as e.g. the high intrinsic detection efficiency and reasonably good energy resolution for fission fragments (∼1.5 MeV), semiconductor detectors have one important drawback. They suffer from what is known as the pulse height defect. Consequently, the total collected charge in the detector, the *pulse height*, due to an incoming heavy ion (e.g. a fission fragment), is smaller than that of a light ion (e.g. an alpha particle) of the same energy. This means that the pulse height is no longer strictly proportional to the energy of the incoming heavy ion, but will also depend on its mass [Sch65, Wei86].

Three processes contribute to this observed PHD [Kno00]:

- The energy loss of the ion in the entrance window and dead layer of the detector.
- Energy loss of the heavy fragments by means other than electronic collisions, nuclear collisions become important when the ions velocity decreases.

- The high rate of electron-hole recombination in the dense plasma created along the ions path.

The PHD is thus due to physical processes and will become more pronounced the heavier the mass of the ion.

For an incoming ion of a given mass, there will still be a linear relationship between the pulse height x and the energy E:

$$E = Ax + B, \tag{4.1}$$

where A and B are constants. This equation has to be modified in experiments with heavy ions of different masses. Schmitt et al. [Sch65] studied the detectors response to ^{80}Br and ^{127}I ions of known energy and found that A and B are approximately linearly dependent on the ion mass. This gives an equation, that can be used for the energy calibration of semiconductor detectors when heavy ions are involved, of the form

$$E = (a + a'm)x + b + b'm, \tag{4.2}$$

where m is the mass (in amu) of the incoming ion and a, a', b, b' are constants for a particular detector. Due to the fact that the pulse height defect is a consequence of physical processes it can be understood that these constants are universal constants for a detector of a given type operating under the same experimental conditions. This means that if the constants can be found for a certain reference system (e.g. the spontaneous fission of ^{252}Cf), then they can also be used for other systems that use the same detectors in the same experimental conditions (e.g. the fission of ^{180}Hg).

The authors of [Sch65] showed that the constants a through b' can be determined from the mean pulse heights P_L, of the light fragment group, and P_H, of the heavy fragment group, of a reference fission fragment spectrum. The calibration constants are then given by:

$$\begin{aligned} a &= A/(P_L - P_H) \\ a' &= A'/(P_L - P_H) \\ b &= B - aP_L \\ b' &= B' - a'P_L, \end{aligned} \tag{4.3}$$

where A, A', B, B' are specific constants for each fissioning isotope. Schmitt et. al determined these constants for the spontaneous fission of ^{252}Cf. Nevertheless, when using equation (4.2) and these values for the constants the determined energies of fission fragments for all fissioning systems are systematically overestimated by 1-2% compared to the energies calculated from the time-of-flight (TOF) method[1] [Hen81, Wei86]. This discrepancy was a long standing problem in fission physics. However, about twenty years after Schmitt et al. determined their values, Weissenberger et al. [Wei86] recalculated the constants using new, modern surface barrier detectors and they found slightly different

[1] In this method the time for the particles to travel a certain distance is measured. The result from the TOF method thus yields the velocities of the fission fragments which are more straightforward to calibrate. By performing a *double-velocity* experiment, where the velocity of both fragments is measured, the mass and the sum of the energies (total kinetic energy, see further) of the fragments can be determined from mass and momentum conservation [Wag91].

values for the constants A through B'. When using these new values the discrepancy between the Schmitt calibration procedure and the TOF-method is removed. This difference in the values for A through B' can be understood by considering that the authors of [Wei86] used modern surface barrier detectors, which have been optimized compared to the initial ones used by Schmitt et al. (e.g. better basic Si material, thinner dead layer) resulting in improved performance (a.o. less energy loss of the fission fragments before they reach the depletion zone where the detection takes place). The constants calculated by Weissenberger et al. for the spontaneous fission of ^{252}Cf are equal to

$$\begin{aligned} A &= 24.300 \\ A' &= 0.0283 \\ B &= 90.397 \\ B' &= 0.1150 \end{aligned} \tag{4.4}$$

Further, Weissenberger et al. state that an accuracy of ± 250 keV can be expected for the kinetic energies of the fission fragments when using these constants and eq. (4.2).

In the current experiment a source of ^{252}Cf was used as reference fissioning system, hence the pulse heights P_L and P_H obtained from these spectra and eq. (4.4) can be used to determine the constants a through b'. A measured example of such a pulse height spectrum of ^{252}Cf for the annular detector (this will be referred to as Detector 1) is shown in Fig. 4.1. A similar spectrum was obtained for the detector behind the foil (referred to as Detector 2).

Table 4.1 gives the pulse heights P_L and P_H, obtained by fitting the two peaks in the spectrum of ^{252}Cf with a double gaussian, and the calculated values for the constants a through b'. The errors on the constants are entirely determined by the errors on P_L and P_H.

	Detector 1 ($i = 1$)	Detector 2 ($i = 2$)
P_H	35432 ± 100	36374 ± 100
P_L	49354 ± 100	51060 ± 100
a_i	$(1.7454 \pm 0.0177) \times 10^{-3}$	$(1.6546 \pm 0.0159) \times 10^{-3}$
a'_i	$(2.0328 \pm 0.0206) \times 10^{-6}$	$(1.9270 \pm 0.0186) \times 10^{-6}$
b_i	4.2526 ± 0.7617	5.9112 ± 0.7063
b'_i	$(1.4675 \pm 0.0887) \times 10^{-2}$	$(1.6607 \pm 0.0823) \times 10^{-2}$

Table 4.1: Pulse heights P_L and P_H of the spontaneous fission of ^{252}Cf and calculated constants a through b' for Detector 1 and 2.

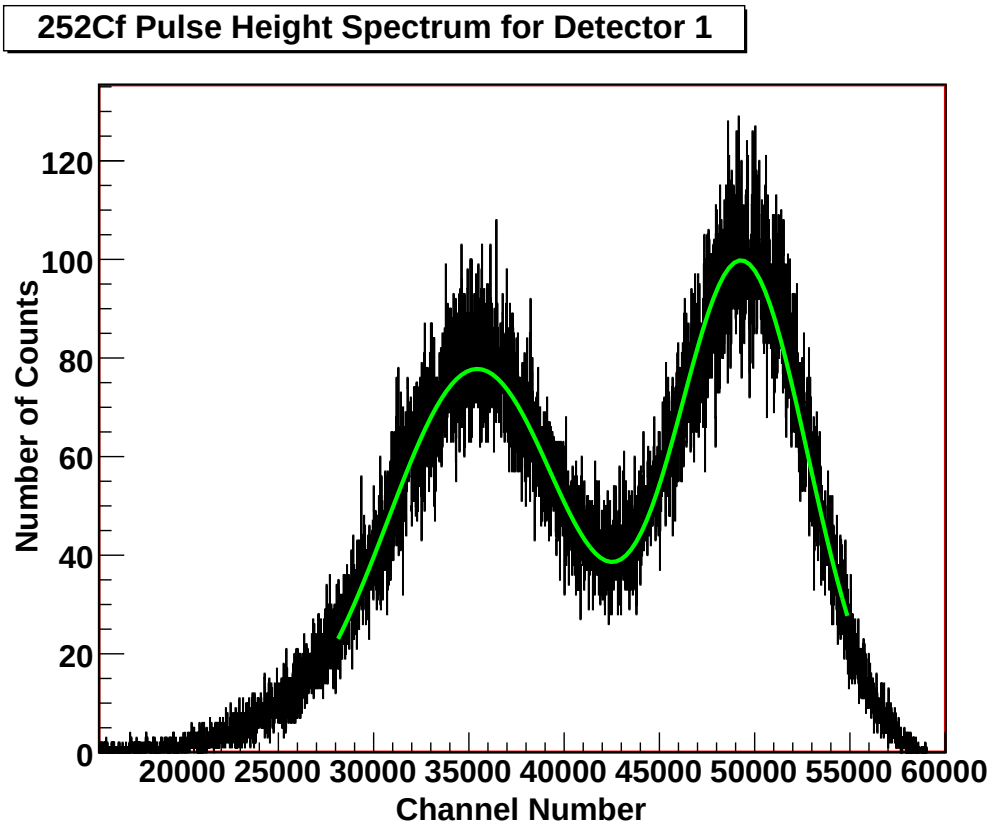

Figure 4.1: Measured pulse height spectrum of ^{252}Cf for the annular detector (Detector 1). The fit with the double gaussian is shown by the light grey line.

4.2 Calibration of Fission Spectra of ^{180}Hg

The determined values for the constants a through b' and eq. (4.2) can now be used to calibrate the fission spectra of ^{180}Hg. However, since eq. (4.2) depends not only on the pulse height x but also on the mass m of the incoming ion, additional equations have to be used, to eliminate the mass m (or the energy E) to be able to calibrate the fission spectra to energy (or mass). These additional equations can be found in the kinematics of the experiment, namely the momentum and mass conservation. These two conditions together with equation (4.2) give the following system of equations:

$$\begin{cases} E_1 = (a_1 + a_1' m_1)x_1 + b_1 + b_1' m_1 \\ E_2 = (a_2 + a_2' m_2)x_2 + b_2 + b_2' m_2 \\ m_1^* E_1^* = m_2^* E_2^* \\ m_1^* + m_2^* = A_f \end{cases} \tag{4.5}$$

In which E_i, m_i and x_i are the energy, mass and measured pulse height of the fragment incident on Detector i (i = 1, 2), the post-neutron quantities. E_i^* and m_i^* are the corresponding initial quantities, before any possible neutron emission has occurred, thus the pre-neutron quantities [Sch66]. A_f is the mass number of the fissioning nucleus. Since

there are four unknowns, the energies and masses of both fragments, the pulse height of both fission fragments (x_1 and x_2) will have to be inserted simultaneously to solve the above equations. Therefore, by using this calibration procedure it is only possible to calibrate coincident fission events.

In order to solve the system of equations (4.5) a relation between E_i and E_i^* and m_i and m_i^* has to be found. These quantities can be related by taking into account the number of neutrons emitted ν_i, the corresponding energy carried away by the neutrons $\Delta E_{i,\nu}$, and the energy loss due to the interaction of the fission fragment with matter along its trajectory $\Delta E_{i,int}$. This last contribution consists of the energy loss of the fragment in the carbon foil $\Delta E_{i,cf}$ and in the dead layer of the detector $\Delta E_{i,dl}$. By considering these factors the following relations can then be deduced:

$$\begin{cases} E_i^* = E_i + \Delta E_{i,\nu} + \Delta E_{i,int} \\ \quad\; = E_i + \Delta E_{i,\nu} + \Delta E_{i,cf} + \Delta E_{i,dl} \\ m_i^* = m_i + \nu_i \end{cases} \tag{4.6}$$

The term $\Delta E_{i,int}$ can be neglected if the fission fragments of the reference system (^{252}Cf) are detected in the same experimental conditions as the fragments of the fissioning isotope of interest (^{180}Hg). If this is the case then $\Delta E_{i,int}$ is automatically included in the calibration constants a through b'. Since the fission fragments of ^{252}Cf also have to pass the dead layer, the contribution $\Delta E_{i,dl}$ to $\Delta E_{i,int}$ is included in a through b'. However, in our case the fission fragments of ^{252}Cf did not have to penetrate the carbon foil, and thus $\Delta E_{i,cf}$ cannot simply be neglected. For the moment, this contribution to $\Delta E_{i,int}$ will not be considered but it will be taken into account later (see section 4.5).

To estimate the energy loss caused by the emitted neutrons $\Delta E_{i,\nu}$, it is beneficial to make first two statements, which are based on experimental facts:

1. Neutrons are emitted by fully accelerated fission fragments.

2. Neutrons are emitted isotropically in the center of mass system.

From the second statement it follows that the *average* velocity of the fission fragments is not changed by the emission of neutrons (the velocity distribution however will be broadened). The kinetic energy of the fragments does change when neutrons are emitted. The first statement is also correct since, as already discussed in section 1.2.3, the fission fragments reach 90% of their maximum kinetic energy after a time of the order of 10^{-20} s after separation, while the neutrons are emitted in a time of the order of 10^{-17} s. From this point it follows that the fragments emit neutrons when they are at their maximum velocity v_i^*.

The average energy of the fragments after neutron emission can then be estimated by (neglecting the recoil energy):

$$\bar{E}_i \approx \frac{1}{2} m_i v_i^2 = \frac{1}{2} m_i v_i^{*^2} = \frac{m_i}{m_i^*} E_i^* \tag{4.7}$$

With this expression $\Delta E_{i,\nu}$ is given by:

$$\Delta E_{i,\nu} = E_i^* - E_i = \frac{\nu_i}{m_i^*} E_i^* \tag{4.8}$$

Substituting eq. (4.6)(neglecting $\Delta E_{i,cf}$) and eq. (4.8) into eq. (4.5) gives:

$$\begin{aligned} E_i^* &= [a_i + a_i'(m_i^* - \nu_i)]x_i + b_i + b_i'(m_i^* - \nu_i) + \Delta E_{i,\nu} \\ &= [a_i + a_i'(m_i^* - \nu_i)]x_i + b_i + b_i'(m_i^* - \nu_i) + \frac{\nu_i}{m_i^*}E_i^* \\ &= (a_i/F_i + a_i' m_i^*)x_i + b_i/F_i + b_i^* m_i^*, \end{aligned} \tag{4.9}$$

with $F_i = 1 - \nu_i/m_i^*$. This finally gives the system of equations, that has to be solved:

$$\begin{cases} E_i^* = (a_i/F_i + a_i' m_i^*)x_i + b_i/F_i + b_i' m_i^* \\ m_1^* E_1^* = m_2^* E_2^* \\ m_1^* + m_2^* = A_f \end{cases} \tag{4.10}$$

It can be seen that the mass and energy values extracted from this set of equations will be the values before any neutron emission has occurred (m_i^* and E_i^*).

The factor F_i will be very close to one, since the neutron multiplicity ν_i is much smaller than the mass of the fragment. Furthermore, it is not clear that there are *any* neutrons emitted in the fission of ^{180}Hg. Therefore, F_i will be set equal to one by setting the number of emitted neutrons to zero. Later it will be shown how the results change when it is assumed that there are some neutrons emitted (section 4.6).

The system of equations (4.10) can now be solved with respect to $m_1^* = m_1$ (when $F_i = 1$ or $\nu_i = 0$). It follows that m_1^* must be the solution of a quadratic equation:

$$A{m_1^*}^2 + Bm_1^* + C = 0 \tag{4.11}$$

with:

$$\begin{aligned} A &= a_1' x_1 + b_1' - a_2' x_2 - b_2' \\ B &= a_1 x_1 + b_1 + a_2 x_2 + b_2 + 2A_f a_2' x_2 + 2A_f b_2' \\ C &= -A_f(a_2 x_2 + a_2' A_f x_2 + b_2 + A_f b_2') \end{aligned}$$

This equation can be solved and gives the mass of the fragments detected in Detector 1. The energy can now easily be deduced from equation (4.2). The mass of the fragments detected in Detector 2 can be obtained by exchanging the labels 1 and 2 in the above equation, or simply from $m_2^* = A_f$ - m_1^*.

4.3 Mass and Energy Distributions

By solving equation (4.11) for m_1^* a mass spectrum can be constructed. However, to be able to work with the raw data from the experiment a program had to be written, as such that the data could be analyzed using the ROOT package [ROO09]. ROOT makes it possible to plot and analyze all the necessary spectra.

By doing this, the spectrum for the masses m_1^* detected in Detector 1 shown in Fig. 4.2(a) results. The mass spectrum for m_2^* is exactly the mirror image of this figure due to the condition $m_2^* = A_f$ - m_1^*. This condition also leads to the existence of a mirror plane at A = 180/2 = 90, when the spectra of both detectors are taken together,

see Fig. 4.2(b). In the right top corner of Fig. 4.2(a) the number of counts in the spectrum is given, which shows that there are 346 coincident fission events measured in the experiment. By fitting both peaks in Fig 4.2(b) with a gaussian, the mean values for the fragment masses and standard deviation can be determined (see Table 4.2).

If the masses of the fragments are known, their energies can be calculated using eq. (4.2). Fig. 4.3(a) and (b) give the energy distribution measured in both detectors separately, while Fig.4.3(c) shows the distribution of the summed spectrum from both detectors together. The total kinetic energy (TKE) can be calculated by adding the energies of the coincident events, see Fig. 4.3(d). The mean values and standard deviations of the energies and total kinetic energy are also given in Table 4.2.

Fig. 4.3(a) through (c) show that the energy distribution of the heavy fragment is broader than that of the light fragment. This is indeed expected, since the heavy fragment should lose more energy in the carbon foil, which results in a larger energy spread. It is only a minor difference however, and if neutron emission is included this argument might change.

		Light Fragment	Heavy Fragment
Mass (amu)	μ	80.7 ± 0.6	99.3 ± 0.6
	σ	4.4 ± 0.6	
Energy (MeV)	μ	73.2 ± 0.7	59.8 ± 0.8
	σ	4.2 ± 0.7	4.7 ± 0.7
TKE (MeV)	μ	132.0 ± 0.7	
	σ	5.4 ± 0.8	

Table 4.2: Mean values μ and standard deviations σ of the mass, energy and total kinetic energy (TKE) for the light and heavy fragment group resulting from the fission of ^{180}Hg, measured by taking the spectra of Detector 1 and 2 together.

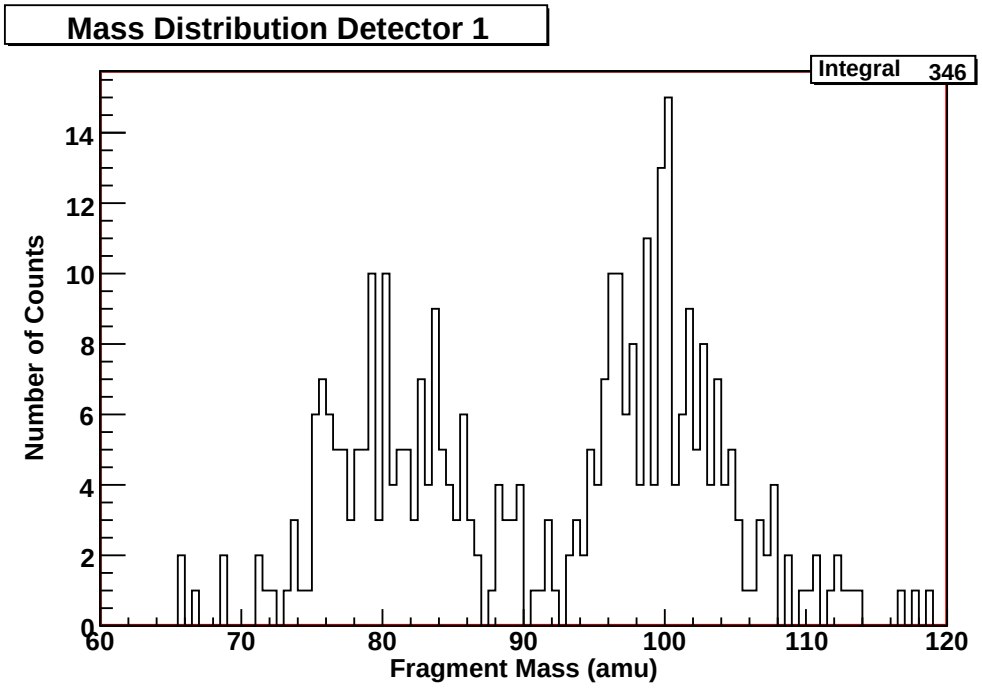

(a) Detector 1

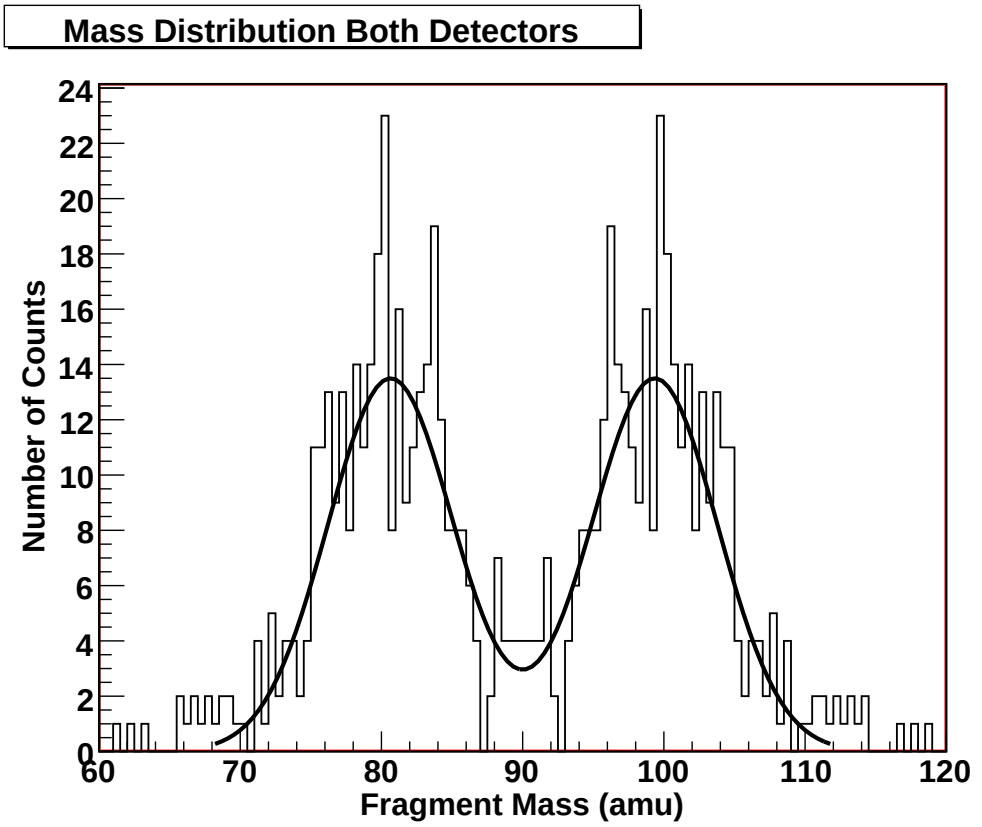

(b) Both Detectors

Figure 4.2: Calculated mass distribution of the fragments resulting from the fission of ^{180}Hg. (a) Fragments incident on Detector 1, (b) spectra of both detectors taken together.

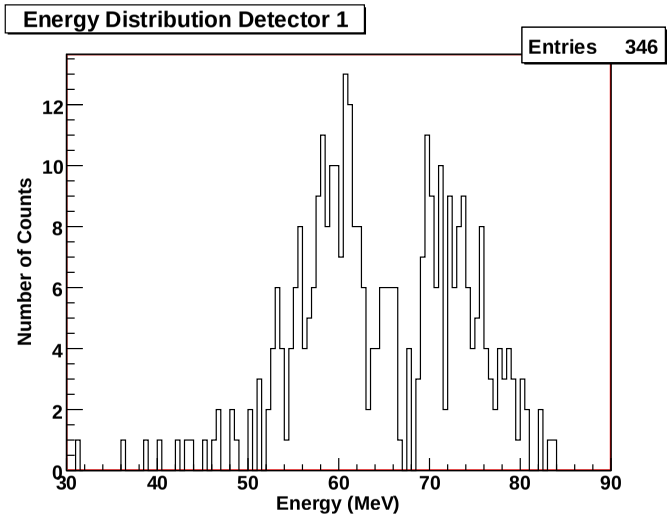

(a) Detector 1

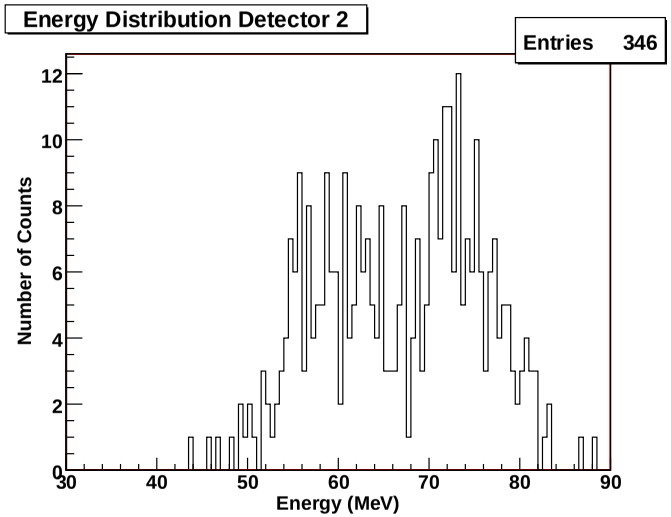

(b) Detector 2

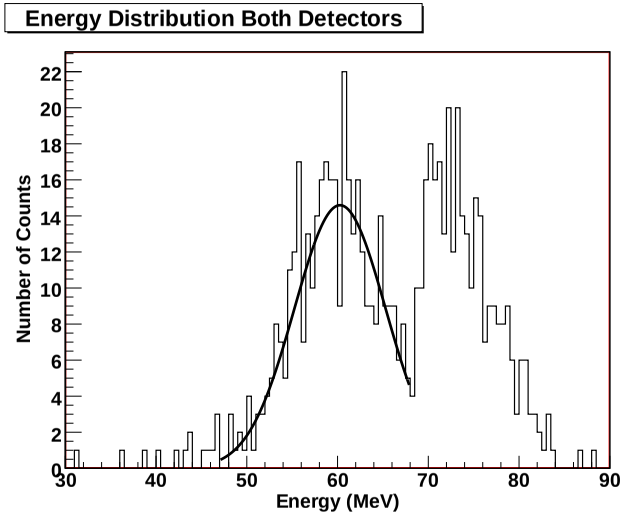

(c) Both Detectors

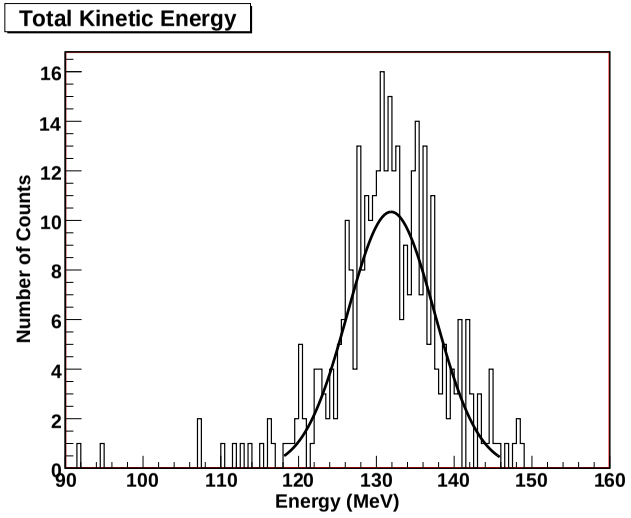

(d) TKE

Figure 4.3: Calculated energy distribution of the fragments, resulting from the fission of ^{180}Hg. (a) Energy distribution measured in Detector 1, (b) in Detector 2, (c) summing the spectra of both detectors and (d) the total kinetic energy (TKE).

4.3.1 Systematics of Mass Distribution

Before the experiment was performed a symmetrical mass split of the fission fragments was expected (see section 2.3). This would lead to fragments with a mass around N = 50 and Z = 40 or ^{90}Zr, to conserve N/Z = 1.25 of ^{180}Hg. However, as is shown in Fig. 4.2(b), an asymmetric mass distribution was observed. This mass distribution as a function of the total kinetic energy is again shown in Fig. 4.4 for the spectra of both detectors together.

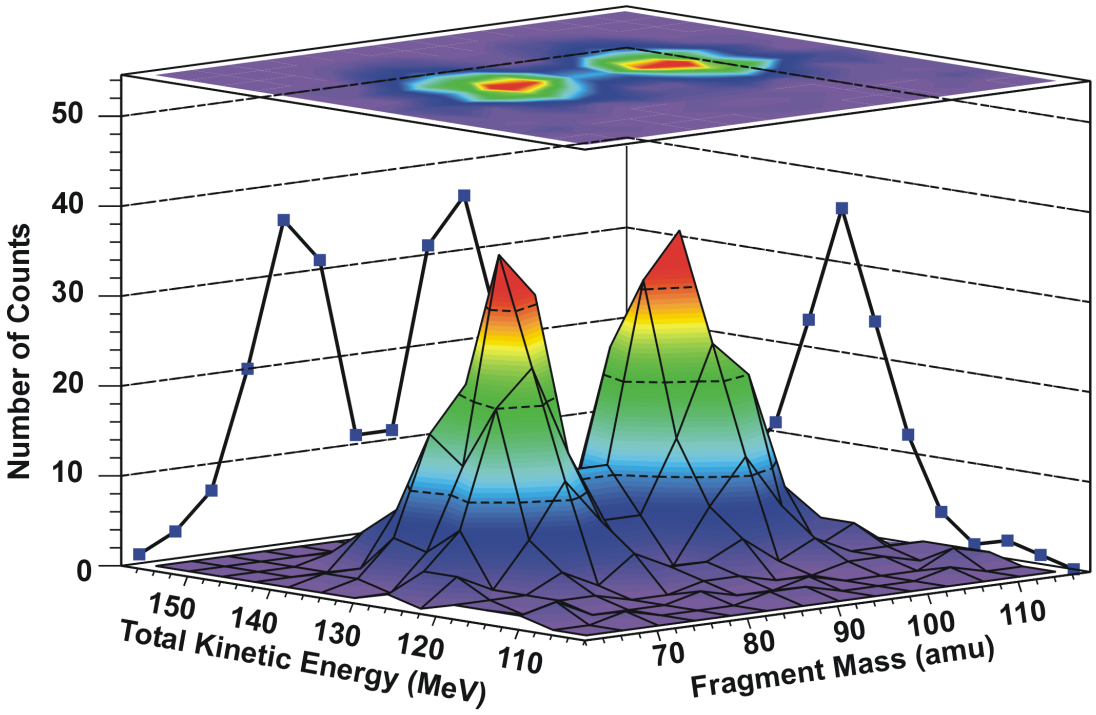

Figure 4.4: Total kinetic energy as a function of fragment mass for the fission of ^{180}Hg, after the electron capture of ^{180}Tl.

From the data of the current experiment itself, it is not possible to deduce the Z value of the formed fission fragments. However, a first guess for the mean Z values can be done by considering first of all that the N/Z ratio of the fragments needs to be approximately equal to N/Z = 1.25, the N/Z value of the fissioning nucleus ^{180}Hg. Secondly, from the analysis of the data it is known that the mean mass numbers are approximately equal to A_L = 80 and A_H = 100, for the light and heavy fragment respectively. Further, the fissioning nucleus is an even-even nucleus, therefore it is expected that the fission fragments will also be even-even nuclei, if no neutrons are emitted. These considerations lead to the nuclei ^{80}Kr, which has N/Z = 1.22 and ^{100}Ru, N/Z = 1.27, which are both stable nuclei.

4.4 Calibration of Single Events

In this section an energy calibration for the single events will be developed. The advantage of trying to find a method to calibrate these single events is an increase in the statistics, since in total 1111 fission fragments were detected of which only 692 (2 × 346) in coincidence.

In this case, it is not possible to use the method described in section 4.2, since it is only applicable to fission fragments that were measured in coincidence. Thus, another approach needs to be developed. In the mass spectrum (Fig. 4.2(b)) both fission fragment peaks can be approximated by a gaussian. This allows to determine the probability for a certain mass to occur. These probabilities can then be used as a weight factor w_i in calculating the energy of the fragment (see below). These weight factors are determined for mass m from 70 to 90, in steps of one, for the light, and m from 90 to 110 for the heavy fragment.

For each pulse height x it is checked if it lies in the light or in the heavy fragment group. This cannot be done very accurately, since it has to be assumed that if the pulse height is lower than a certain value, it belongs to the heavy fragment group, and if it is higher, it belongs to the light fragment group. Then, an energy can be found by using equation (4.2) and by taking a mass value m ranging from 70 until 90 for the light and 90 until 110 for the heavy fragment group. Thus, for each pulse height 21 energies are calculated. Finally, it is then possible to determine an average energy value, by using the different weight factors. For the light group (and completely analog for the heavy group) this gives:

$$\begin{aligned} E_x &= w_{m=70}E_{m=70} + w_{m=71}E_{m=71} + \ldots + w_{m=90}E_{m=90} \\ &= \sum_{i=70}^{90} w_{m=i}E_{m=i}, \end{aligned}$$

where E_x is the average energy for a certain pulse height x, w_i are the weight factors for a certain mass m and E_i are the energies calculated using eq. (4.2), x and m.

The spectrum of the average energy is shown in Fig. 4.5(a), for the registered fission fragments of both detectors together. Roughly twice more fragments were registered in Detector 2 than in Detector 1 (724 in Detector 2 compared to 387 in Detector 1). This difference can be attributed to the hole in Detector 1.

In order to check if this method to calibrate the single events is justified, it was also applied to the coincident events. The obtained results can then be directly compared to the (correct) Schmitt calibration method described in section 4.2. The difference between both methods is shown in Fig. 4.5(b). In the right top corner of the figure it is shown that the method for the single events deviates on average by about 200 keV from the (correct) method for the coincident events. Therefore, it is shown, that the calibration of the single events is allowed, even though it is only a rough approximation.

The TKE for the coincident fragments calibrated with the calibration method for the single events is shown in Fig. 4.6. The mean value of the TKE deduced from the fit is given by

$$\mu_{TKE} = (131.9 \pm 0.6)\ \text{MeV},$$

and the standard deviation

$$\sigma_{TKE} = (5.1 \pm 0.7)\ \text{MeV}$$

in good agreement with the result deduced by using the correct Schmitt calibration method.

As mentioned above, to increase the statistics it is beneficial to calibrate also the single events. However, this method is only a rough approximation and does not make it possible to deduce anything new from the spectra, and will therefore not be used further. In the further analysis, only the coincident events will be considered.

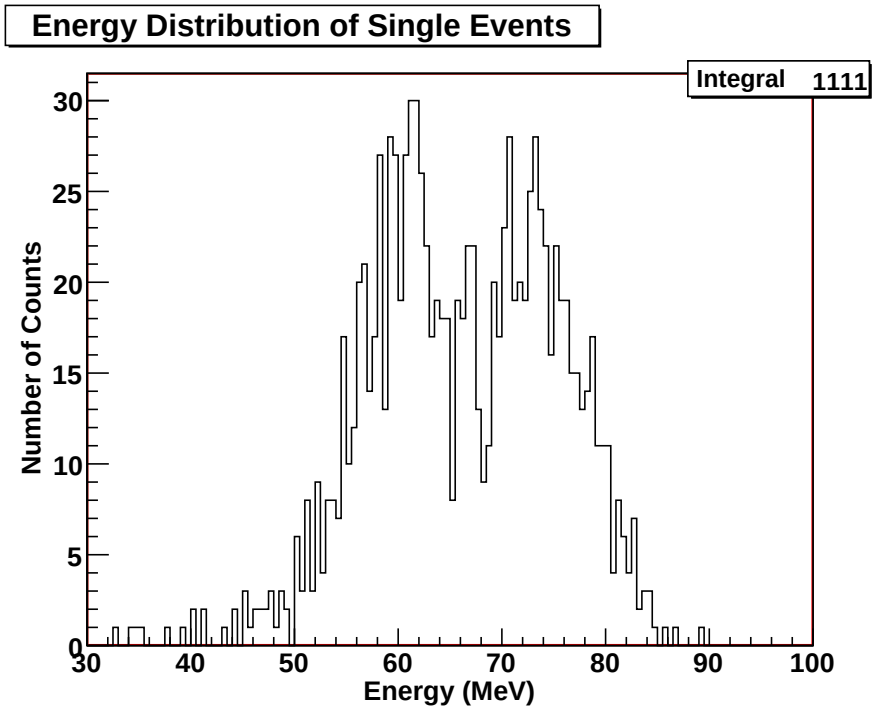

(a)

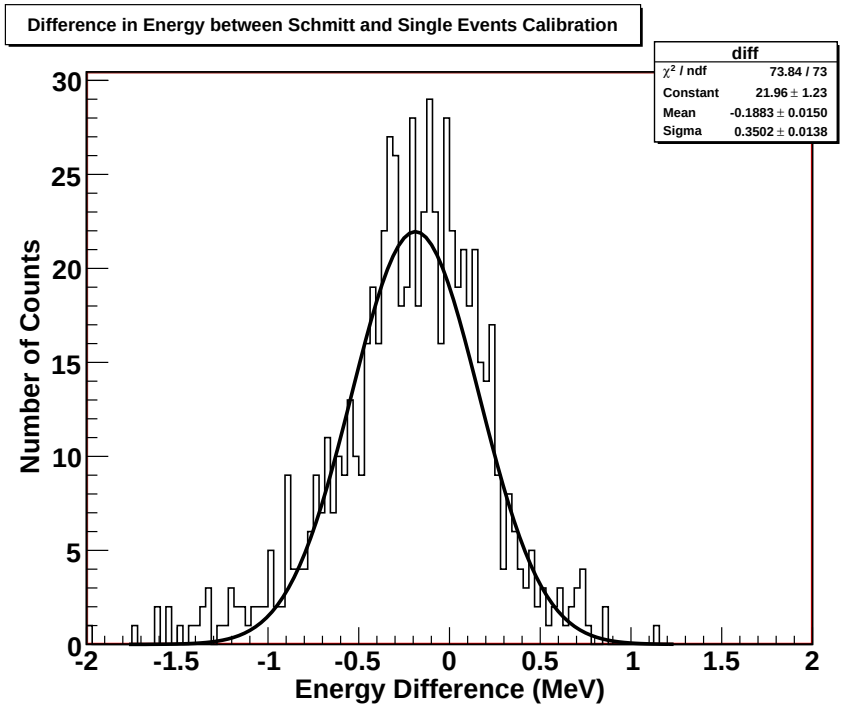

(b)

Figure 4.5: (a) Energy distribution of the single events, taking the spectra of both detectors together. (b) Energy difference between the Schmitt calibrated coincident events and the coincident events that were calibrated using the method for the single events.

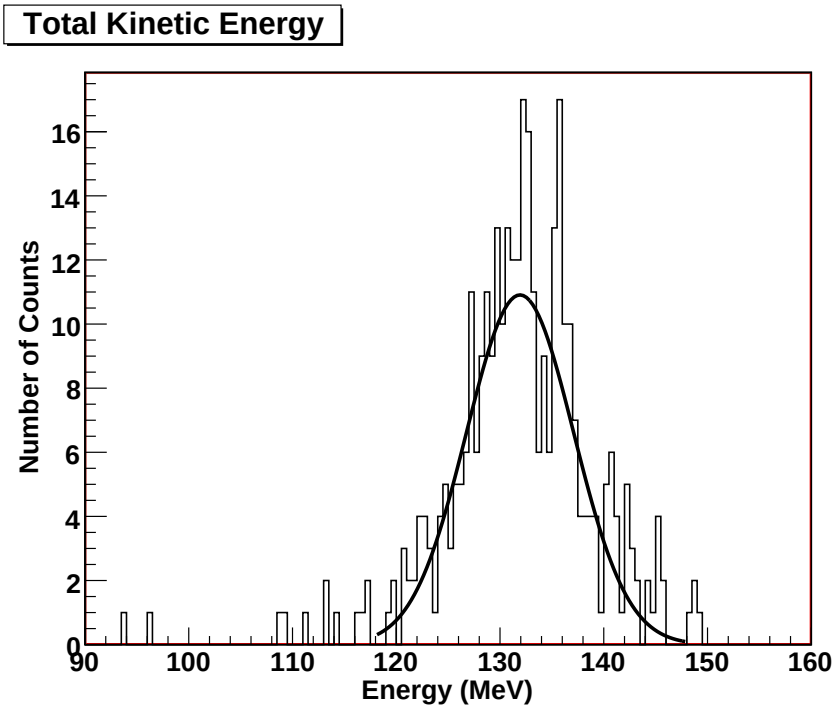

Figure 4.6: Total kinetic energy of the coincident events using the calibration method for the single events.

4.5 Energy Loss in the Carbon Foil ($\Delta E_{i,cf}$)

To make a correct energy calibration the energy loss of the fission fragments in the carbon foil, namely the term $\Delta E_{i,cf}$ in eq. (4.6), has to be estimated. This can be done with the computer program SRIM [SRI08]. First, the depth of implantation of the ^{180}Tl beam in the carbon foil has to be determined. The energy of the beam is 30 keV and the stopping power S (nuclear + electronic) for the beam in the carbon foil is $S = 13.149$ keV/(μg/cm^2), which results in a mean implantation depth d of

$$d = 2.281 \mu\text{g/cm}^2 = 101 \text{ Å}$$

Since the carbon foil has a thickness of $t = 20$ μg/cm^2 = 888 Å, the nuclei will be implanted in the first 1/9 part of the foil.

The program TRIM, a package of SRIM, can calculate the distribution of the depth of implantation of the Tl nuclei in the carbon foil. If this is known and it is assumed that the light fragment is ^{80}Kr with an energy of 73 MeV (see Table 4.2) and that the fragments are randomly emitted in 4π, then SRIM can calculate the energy loss of those emitted light fragments. The result of the SRIM calculations are two files, one with the energy loss of the transmitted fragments, thus those that fly in the direction of Detector 2, and one with the energy loss of the fragments flying towards Detector 1. The energy of the fragments, after passing through the carbon foil, is shown in Fig. 4.7(a) and (b). Exactly the same can be done for the heavy fragment, assuming ^{100}Ru with an energy of 59 MeV. The result is shown in Fig. 4.7(c) and (d).

The size of the detectors (including the hole in Detector 1) was taken into account in

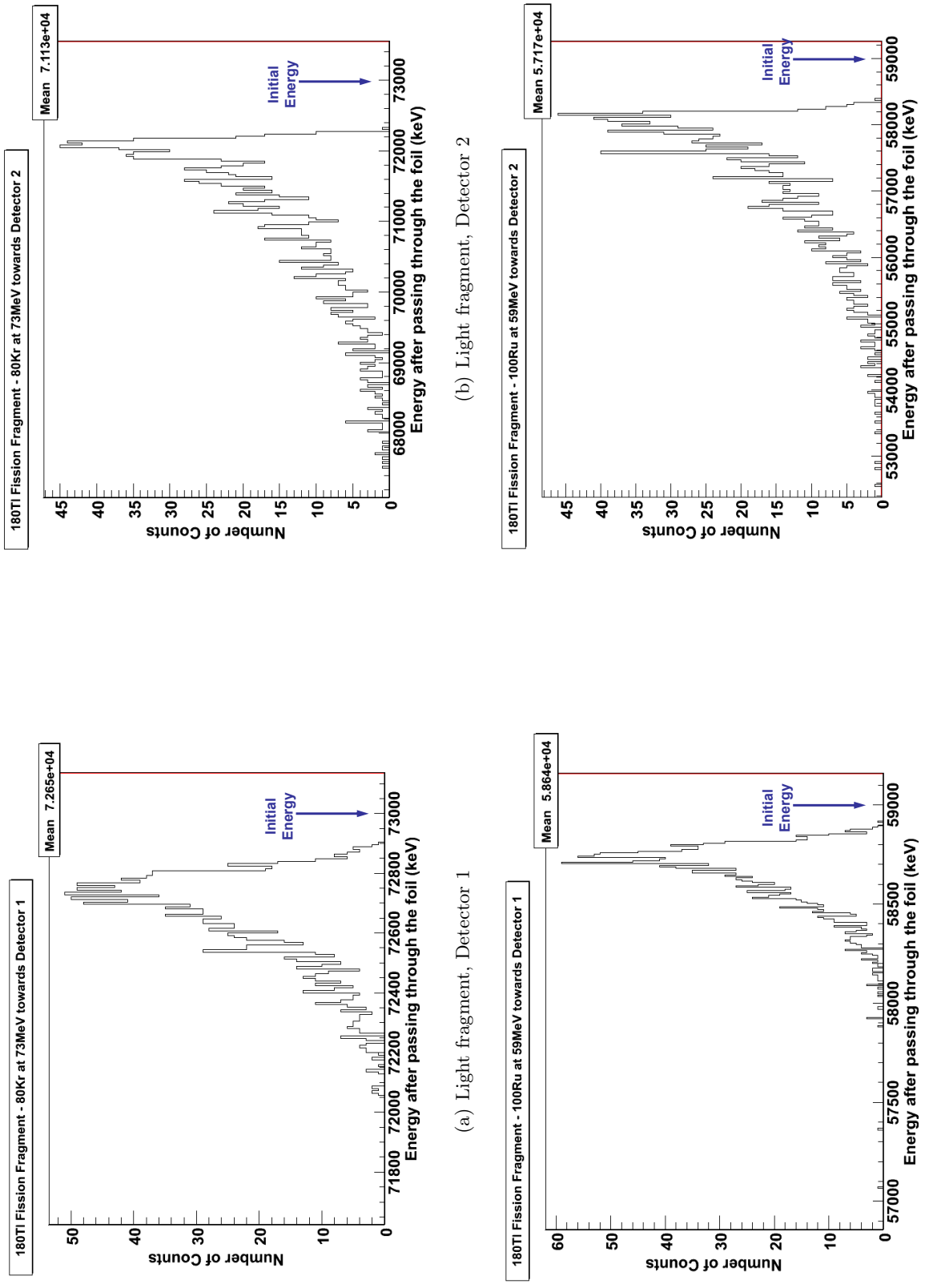

(a) Light fragment, Detector 1

(b) Light fragment, Detector 2

(c) Heavy fragment, Detector 1

(d) Heavy fragment, Detector 2

Figure 4.7: Distribution of the energy loss of the light ((a) and (b)) and heavy ((c) and (d)) fragment in Detector 1 and 2. The figures show the energy of the fragments after penetration through the carbon foil.

the calculations. This is the reason why really high energy losses of the fragments do not occur, as can be seen in Fig 4.7. Due to the finite size of the detectors, fragments that are emitted at large angles will not hit the detector, and thus will not be registered. These fragments need to pass the largest distance through the carbon foil, and thus would have the largest loss in energy.

For the fragments flying towards Detector 1 the mean energy loss will be about 0.5 MeV (see Fig. 4.7(a) and (c)). The fragments do not need to pass a great distance through the carbon foil in this direction. However, because of the hole in the detector, only fragments emitted at angles larger than a certain minimum angle can be detected. As a consequence, fragments flying in the direction of Detector 1 will even so lose some energy. The energy loss of fragments flying towards Detector 2 can reach about 2 MeV (Fig. 4.7(b) and (d)).

The only way to take these energy losses into account is to assume that every fragment flying in the direction of Detector 2 loses 2 MeV and every fragment flying towards Detector 1 loses 0.5 MeV. This is of course not entirely correct, because not all particles will lose that energy, this is more an extreme case. By taking these energy losses into account it is now possible to recalculate the mass and energy distributions, which are shown in Fig. 4.8 for the spectra of both detectors together. The recalculated mean values μ and standard deviations σ are given in Table 4.3. The mean mass values do not change, within error bars, as is expected, since the carbon foil only introduces a loss in energy, and not a change in mass. The energy and total kinetic energy, however do change and are shifted to higher energies. Since the carbon foil introduces an energy loss, the original energy of the fragments will be higher than the energy that is measured. The mean TKE increases by about 2.5 MeV, as it should, since a total energy loss of 2.5 MeV in the carbon foil was introduced (compare Table 4.2 and Table 4.3).

		Light Fragment	Heavy Fragment
Mass (amu)	μ	80.5 ± 0.5	99.5 ± 0.5
	σ	4.0 ± 0.3	
Energy (MeV)	μ	74.2 ± 0.6	60.8 ± 0.6
	σ	4.6 ± 0.8	4.6 ± 0.6
TKE (MeV)	μ	134.6 ± 0.7	
	σ	5.6 ± 0.8	

Table 4.3: Recalculated mean values μ and standard deviations σ of the mass, energy and total kinetic energy (TKE) for the light and heavy fragment group when the energy loss in the carbon foil is taken into account, measured by taking the spectra of Detector 1 and 2 together.

4.6 Correction for the Possible Neutron Emission

If neutrons are emitted the previous results will of course change. Unfortunately, there is no way, in the current experiment, to measure if there are or are not neutrons emitted. However, it is possible to infer the maximum number of neutrons emitted in each fission event by comparing the Q-value of the fission to the total kinetic energy. Since the Q-value is the total released energy, the TKE can never be larger than the Q-value. This Q-value

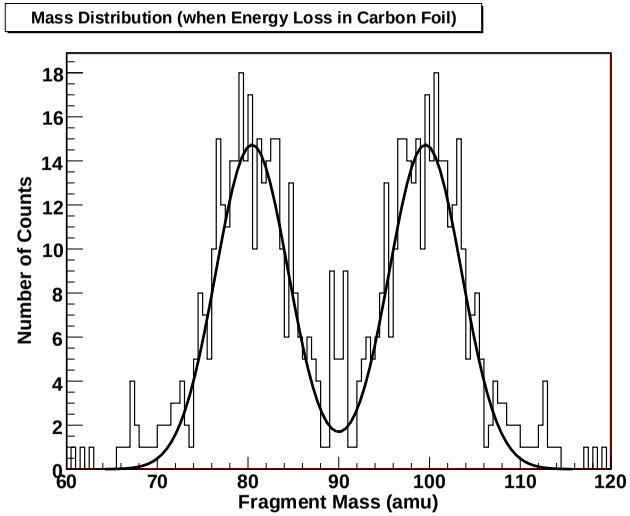

(a) Mass Distribution

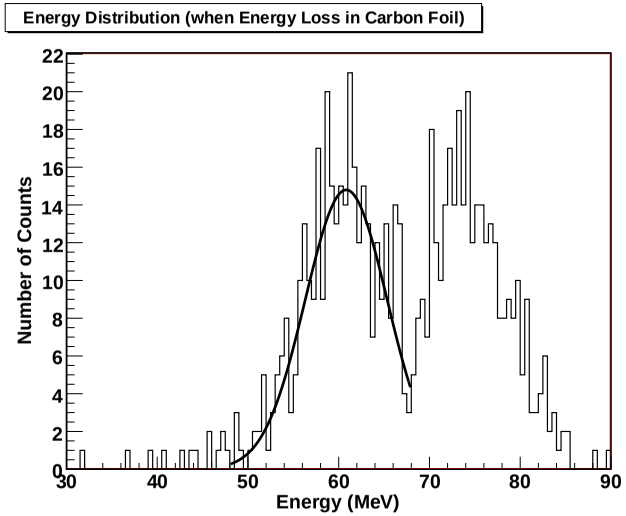

(b) Energy Distribution

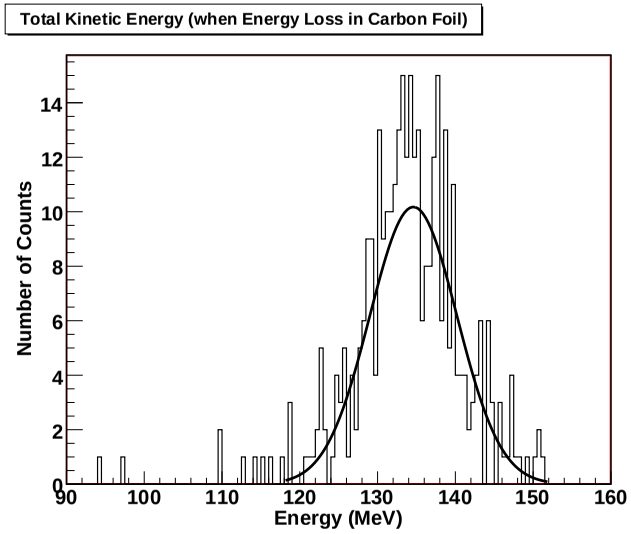

(c) TKE

Figure 4.8: Recalculated (a) mass, (b) energy and (c) total kinetic energy distribution when the energy loss in the carbon foil is taken into account, for the spectra of both detectors together.

for different N/Z ratios as a function of the mass fraction for the light and heavy fragment is shown in Fig. 4.9. In the case of the fission of ^{180}Hg the most probable N/Z ratio is 1.25 (the blue triangles in the figures). The measured mean TKE = (134.6 ± 0.7) MeV in the fission of ^{180}Hg (the horizontal line) and the most probable mass fraction (the vertical line), defined as $m_f = 100/180 = 0.556$ for the heavy and $m_f = 80/100 = 0.444$ for the light fragment, are denoted by the dashed lines.

Fig. 4.9(a) shows that the TKE lies well beneath the Q-values (blue triangles) in the neighborhood of $m_f = 0.556$ and $m_f = 0.444$, when no neutrons are emitted. The excitation energy E^* of the fission fragments can then be calculated as

$$E^* = Q - TKE$$

This excitation energy can be calculated for the most probable mass split resulting from the fission of ^{180}Hg, namely the fission which results in the fragments ^{100}Ru and ^{80}Kr. The Q-value for this fission is then given by (m are the atomic mass values)

$$Q_{fis} = m(^{180}Hg) - m(^{100}Ru) - m(^{80}Kr) \approx 147 \text{ MeV}$$

which is indeed shown in Fig. 4.9(a). The excitation energy would then be $E^* \approx 147$ MeV - 135 MeV = 12 MeV. However, the Q_{EC}-value for the electron capture of ^{180}Tl leading to ^{180}Hg is about 11 MeV. Thus the highest excited state that can be reached in ^{180}Hg is ∼11 MeV. This would add an extra 11 MeV to the total Q-value in the fission of ^{180}Hg, $Q_{tot} = Q_{fis} + Q_{EC} \approx 158$ MeV. This extra 11 MeV will go into excitation energy of the fragments and thus the total excitation energy is then given by $E^* \approx 23$ MeV. This is shared between both fragments which will then each end up with an excitation energy of ∼10-12 MeV.

To see if a neutron can be emitted the neutron separation energy of the fragments has to be taken into account. This is the minimal energy required to remove a neutron from the nucleus. The neutron separation energies S_n of ^{80}Kr and ^{100}Ru are $S_n(^{80}\text{Kr}) =$ 11.5 MeV and $S_n(^{100}\text{Ru}) = 9.6$ MeV [ENS08]. The excitation energy of the fragments will thus lie in the order of the neutron separation energies, as such one neutron could be emitted by the fragments. However, it is important to note that the emission of one neutron can only happen at the limit, since also γ-rays in coincidence with the fission fragments were observed. These γ-rays will remove some of the excitation energy of the fission fragments and thus will lower the energy available for neutron emission. Also the kinetic energy of the neutron will further lower the available energy. By taking these energy contributions into account, it could be that the excitation energy becomes too low to emit a neutron. Of course, also other fragments than ^{80}Kr and ^{100}Ru will be formed, perhaps with a lower neutron separation energy, as such that the excitation energy can again overcome the neutron separation energy.

From this discussion it could be concluded that both fragments can emit a neutron, and thus that in total two neutrons can be emitted in the fission process. This will however not be the case as can be deduced from the following considerations. The possibility for the emission of one neutron in the fission of ^{180}Hg can be deduced by considering the most probable mass split where ^{100}Ru or ^{80}Kr emits a neutron:

$$^{180}\text{Hg} \rightarrow {}^{100}\text{Ru} + {}^{79}\text{Kr} + {}^{1}\text{n} \qquad Q \approx 135 \text{ MeV}$$

$$^{180}\text{Hg} \rightarrow {}^{99}\text{Ru} + {}^{80}\text{Kr} + {}^{1}\text{n} \qquad Q \approx 137 \text{ MeV}$$

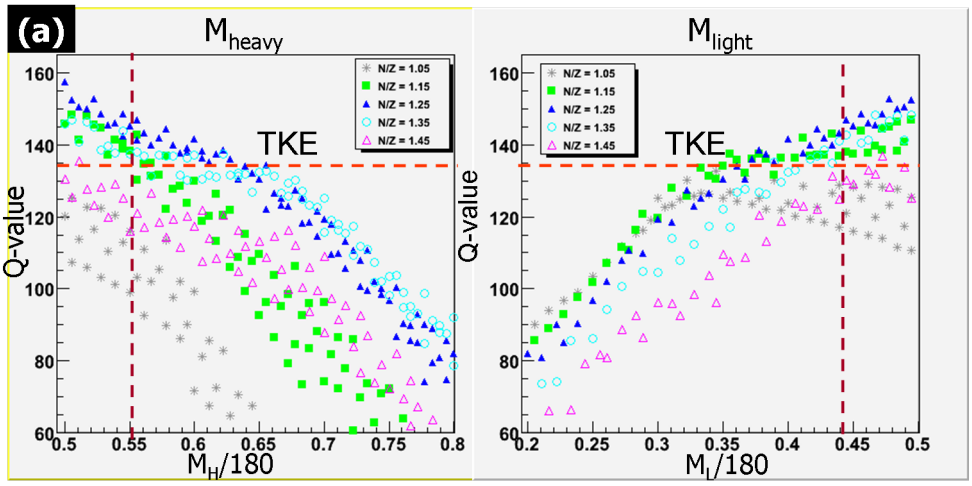

(a) No neutron emitted

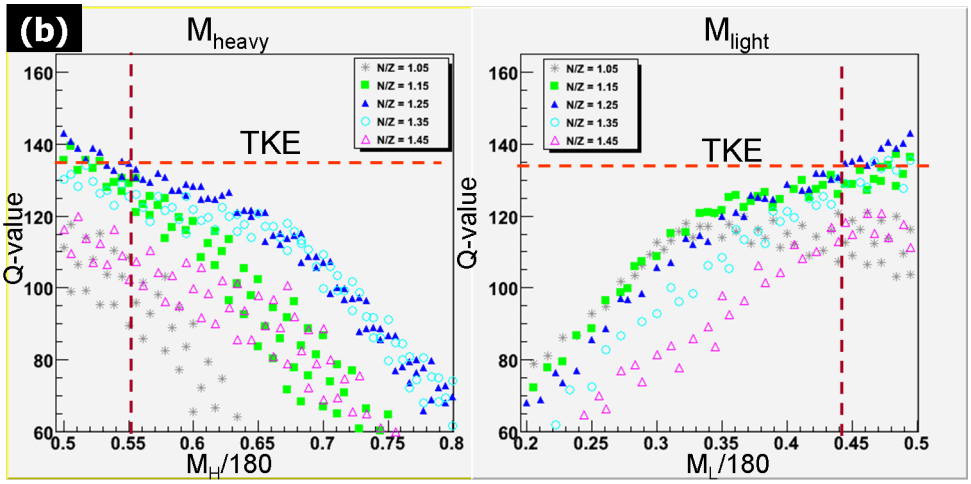

(b) One neutron emitted

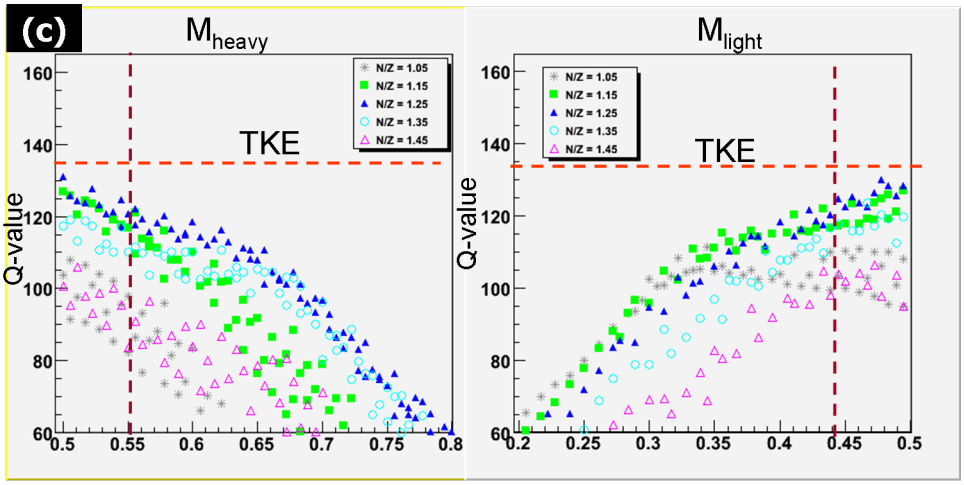

(c) Two neutrons emitted

Figure 4.9: Q-values for fission of ^{180}Hg for different N/Z ratios as a function of mass fraction, when (a) no neutrons are emitted, (b) one neutron is emitted and (c) two neutrons are emitted [Ant]. The total kinetic energy in the fission of ^{180}Hg is also shown.

This shows that the TKE = (134.6 ± 0.7) MeV now lies in the order of the Q-value when the emission of one neutron is taken into account, which can also be seen in Fig. 4.9(b). This means that most of the Q-value will be converted to TKE, and not much energy will be available for the excitation of the fragments. However, the 'extra' 11 MeV of the EC of ^{180}Tl has again to be considered. As a result, after neutron emission the fission fragments will end up with an excitation energy of ∼5-6 MeV. This will be too low for the emission of a second neutron. This can be deduced from Fig. 4.9(c), where it is clearly shown that two neutron emission is impossible since then the Q-value is smaller than the TKE.

Overall, on the basis of this discussion, it can be concluded that it cannot be excluded that one neutron is emitted.

To calculate the effect on the mass and energy distributions when one neutron is emitted, equation (4.10) has to be solved for $F_i \neq 1$. This can be done through an iteration and by replacing a_i and b_i by a_i/F_i and b_i/F_i respectively in eq. (4.11). Start from the solution of eq. (4.11) with $F_i = 1$, which gives the masses m_i^* when no neutrons are emitted. These can be used to calculate new factors F_i, which can then be used to solve eq. (4.11) again, now with $F_i \neq 1$. This process is iterated until a stable solution is obtained for m_i^*. This typically will take only a few iterations. In this section the energy loss in the carbon foil will not be taken into account, this will be done in the following section.

According to the above discussion maximum one neutron can be emitted, thus the calculations will be limited to this case ($\nu_i = 1$). In the Schmitt calibration method the pre-neutron mass m_i^* is calculated (see e.g. eq. (4.10)). Therefore, the mass distribution will not be affected when neutron emission is introduced. The new deduced mean mass values and the standard deviation are shown in Table 4.4, and indeed, within the error bars they are not different from the ones given in Table 4.2 for no neutron emitted.

The energy distribution however does change, since the detected energy is that after neutron emission, but the Schmitt calibration method determines the energy before any neutrons are emitted. A comparison between the energy distribution without any neutrons emitted and with one neutron emitted is shown in Fig. 4.10(a) and calculated mean values are given in Table 4.4. There is a little shift in energy, especially the light fragment gains roughly 1 MeV in energy compared to the energy values given in Table 4.2. The difference in TKE is shown in Fig. 4.10(b) and the mean value also in Table 4.4. The mean value in the TKE increases by about 1.2 MeV when one neutron is emitted compared to the TKE of (132.0 ± 0.7) MeV when no neutrons are emitted. This lies in the range of what is expected, since the average energy carried away by a prompt neutron in fission should be of the order of 2 MeV [Kra88]. Of course, it is still not possible to deduce if there are *any* neutrons emitted, but it is also not possible to make a clear distinction between the two cases, as can be seen from the spectra. The TKE value for the case when one neutron is emitted, is still, within error bars, in agreement with the value when no neutron is emitted.

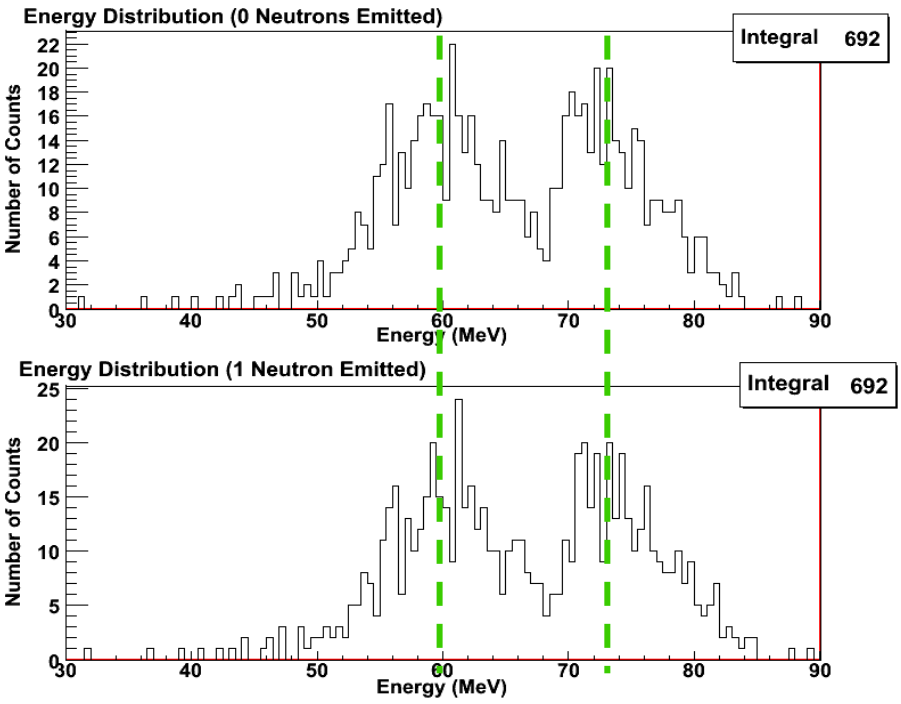

(a)

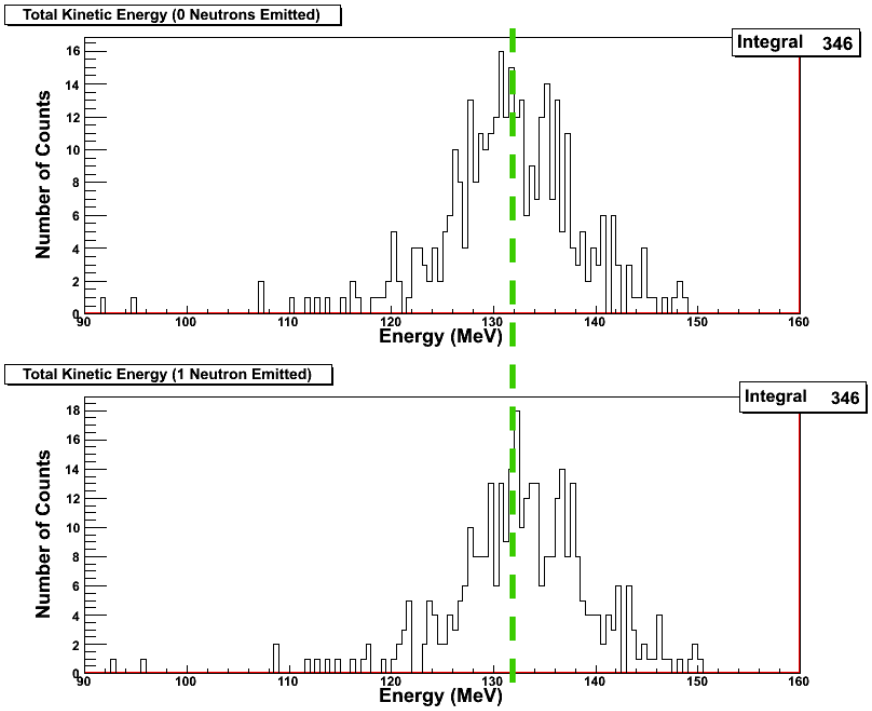

(b)

Figure 4.10: Comparison between the (a) energy distribution and (b) total kinetic energy when one and zero neutrons are emitted.

		Light Fragment	Heavy Fragment
Mass (amu)	μ	80.8 ± 0.6	99.2 ± 0.6
	σ	4.3 ± 0.3	
Energy (MeV)	μ	74.2 ± 0.8	60.2 ± 0.8
	σ	4.3 ± 0.8	4.6 ± 0.8
TKE (MeV)	μ	133.2 ± 0.7	
	σ	5.9 ± 0.8	

Table 4.4: Recalculated mean values μ and standard deviations σ of the mass, energy and TKE for the light and heavy fragment group when one neutron is emitted, calculated by taking the spectra of both detectors together and neglecting the energy loss in the carbon foil.

To calculate the mass of the fragments after one neutron is emitted a different approach has to be considered. The mass and energy after, m_i and E_i, and before, m_i^* and E_i^*, a neutron is emitted can be related as follows (neglecting the energy loss in the carbon foil $\Delta E_{i,cf}$):

$$\begin{cases} m_i^* = m_i + \nu_i \\ E_i^* = E_i + \Delta E_{i,\nu} \end{cases} \tag{4.12}$$

where ν_i is the number of neutrons emitted by the fragment of mass m_i^* and $\Delta E_{i,\nu}$ is the energy carried away by those neutrons. It is well known that the average energy carried away by a neutron is of the order of $\sim$2 MeV [Kra88]. In the present calculation it is assumed that the total number of emitted neutrons $\nu_{tot} = \nu_1 + \nu_2 = 1$ and thus the total energy carried away by the neutrons is 2 MeV. Thus, on average the number of neutrons emitted by a fragment of mass m_i^* is $\nu_i = 0.5$ and the average energy taken away by this is $\Delta E_{i,\nu} = 1$ MeV. This is of course unphysical, but this is the only possible estimate that can be made. By using eq. (4.5) and eq. (4.12) the following equation can be obtained that has to be solved for m_1:

$$Am_1^2 + Bm_1 + C = 0 \tag{4.13}$$

with:

$$\begin{aligned} A &= a_1'x_1 + b_1' - a_2'x_2 - b_2' \\ B &= a_1x_1 + a_1'x_1\nu_1 + b_1 + b_1'\nu_1 + a_2x_2 \\ &\quad +2a_2'x_2A_f + a_2'x_2(\nu_2 - 2\nu_{tot}) + b_2 \\ &\quad +b_2'(2A_f - 2\nu_{tot} + \nu_2) + \Delta E_{1,\nu} + \Delta E_{2,\nu} \\ C &= \nu_1(a_1x_1 + b_1) - (a_2x_2 + b_2)(A_f - \nu_{tot} + \nu_2) \\ &\quad -(a_2'x_2A_f + b_2'A_f)(A_f - 2\nu_{tot} + \nu_2) \\ &\quad -(a_2'x_2\nu_{tot} + b_2'\nu_{tot})(\nu_{tot} - \nu_2) - \Delta E_{2,\nu}(A_f - \nu_{tot}) \end{aligned}$$

For one emitted neutron the result is shown in Fig. 4.11. Hardly any difference can

be seen with the mass distribution when no neutrons are emitted. Thus, it is not possible to distinguish between the mass spectra of no and one emitted neutron. The recalculated mean mass values $\mu_{m_{L,H}}$ and standard deviation σ_m are given by

$$\mu_{m_L} = (80.4 \pm 0.6)\ \text{amu} \qquad \mu_{m_H} = (98.6 \pm 0.6)\ \text{amu}$$

$$\sigma_m = (4.2 \pm 0.6)\ \text{amu}$$

and indeed only a small deviation from the result when no neutrons are emitted is seen (compare with the mass values in Table 4.2 or Table 4.4). Even though the mean mass value of the heavy fragment seems to decrease by almost one compared to the value of Table 4.2, within the error bars the result is still consistent with the one where no neutrons are emitted. Of course, the sum of the mean mass values now equals 179 and not 180.

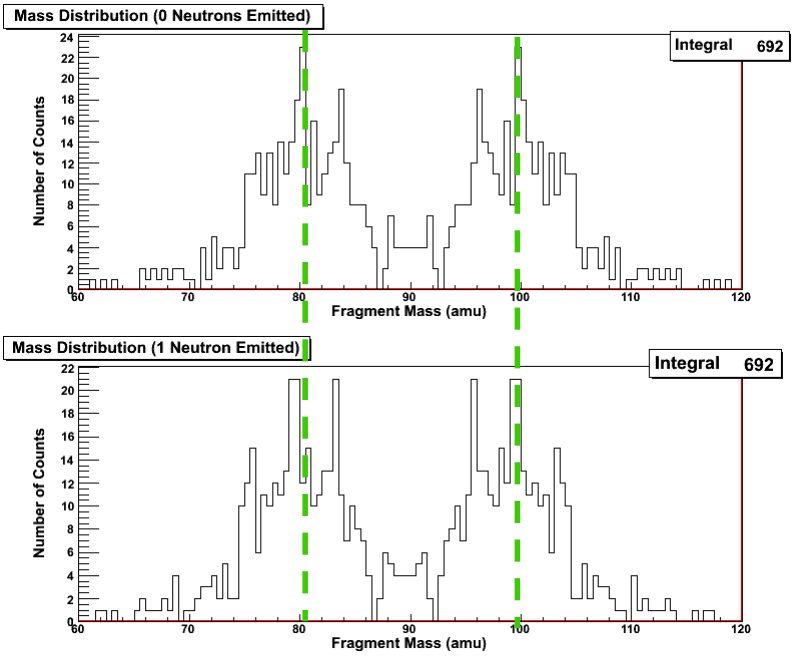

Figure 4.11: Comparison of the mass distribution when no and one neutron is emitted. Note that the bottom figure represents the mass values *after* neutron emission has occurred.

4.7 Correction for Neutron Emission and Energy Loss in the Carbon Foil

Now it is appropriate to put the results of the previous two sections together, as such to see how the results change when one neutron is emitted *and* the energy loss in the carbon foil is taken into account. This is shown in Fig. 4.12 and Table 4.5. The mean mass values in Table 4.5 do almost not change compared to the values when no neutrons are emitted (Table 4.3), as they should. Due to the neutron emission the total kinetic energy increases again by about 1.2 MeV compared to the value of Table 4.3, as expected. However, also

in this case it is difficult to distinguish between the cases where no and one neutron is emitted.

		Light Fragment	Heavy Fragment
Mass (amu)	μ	80.4 ± 0.5	99.6 ± 0.5
	σ	3.9 ± 0.3	
Energy (MeV)	μ	75.1 ± 0.8	61.3 ± 0.7
	σ	4.7 ± 0.8	4.5 ± 0.7
TKE (MeV)	μ	135.7 ± 0.8	
	σ	5.9 ± 0.8	

Table 4.5: Recalculated mean values μ and standard deviations σ of the mass, energy and TKE for the light and heavy fragment group when one neutron is emitted and the energy loss in the carbon foil is taken into account, deduced by taking the spectra of Detector 1 and 2 together.

The mean mass values $\mu_{m_{L,H}}$ and standard deviation σ_m after a neutron is emitted can also now be deduced:

$$\mu_{m_L} = (80.0 \pm 0.5) \text{ amu} \qquad \mu_{m_H} = (99.0 \pm 0.5) \text{ amu}$$

$$\sigma_m = (3.9 \pm 0.3) \text{ amu}$$

These mass values do again not differ much from the values when no neutron is emitted (Table 4.3) and are still in agreement within error bars. However, of course the sum of the mean mass values now equals again 179 and not 180.

4.8 Discussion

In the ECDF of ^{180}Tl a symmetric mass distribution, centered around the nucleus ^{90}Zr, was expected in the fission of the daughter nucleus ^{180}Hg. Instead it was observed that ^{180}Hg, after the EC of ^{180}Tl, fissions in two fragments of unequal mass around mass number A = 80 and 100. Thus an asymmetric mass distribution was measured, see e.g. Fig. 4.4. The most probable fission fragments were determined to be ^{100}Ru and ^{80}Kr.

The asymmetric mass distribution can now be compared to other mass distributions of low energy fissioning systems throughout the nuclear chart, see Fig. 4.13. Until the discovery of the asymmetric mass distribution of ^{180}Hg, fissioning nuclei lighter than Ra showed in general a symmetric mass distribution. The actinide region and heavier elements show an asymmetric mass distribution, with some exceptions (e.g. ^{258}Fm).

The mean total kinetic energy of the fission fragments was calculated to be (134.6 ± 0.7) MeV, when the energy loss in the carbon foil is taken into account. This high average TKE, $\langle E_k \rangle$, of the fission fragments, compared to other decay modes, is the result of the high Coulomb repulsion between the fragments. There is indeed a relation between the average TKE and the Coulomb parameter $Z^2/A^{1/3}$. Intuitively, this can be deduced as follows: At the moment of scission the fissioning system can be imagined as two touching spherical fragments with charge $Z_i e$ and radius $r_i = R_0 A_i^{1/3}$, where $i = L$, H for the light

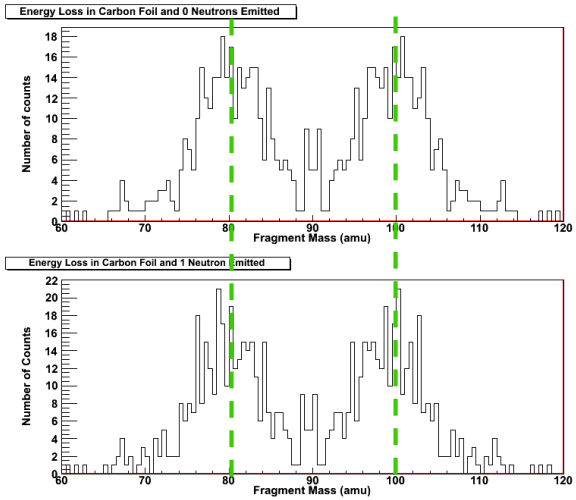

(a) Mass Distribution

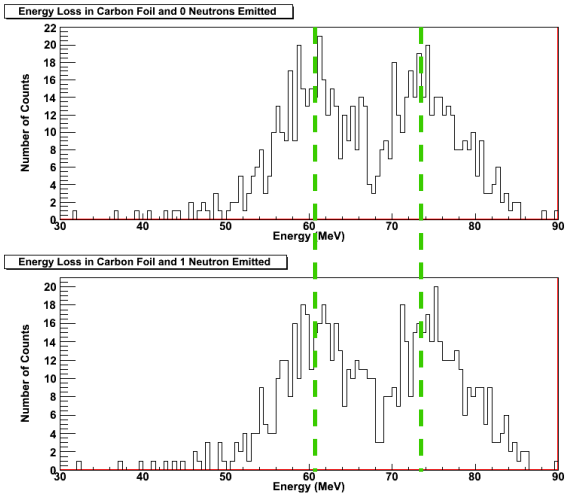

(b) Energy Distribution

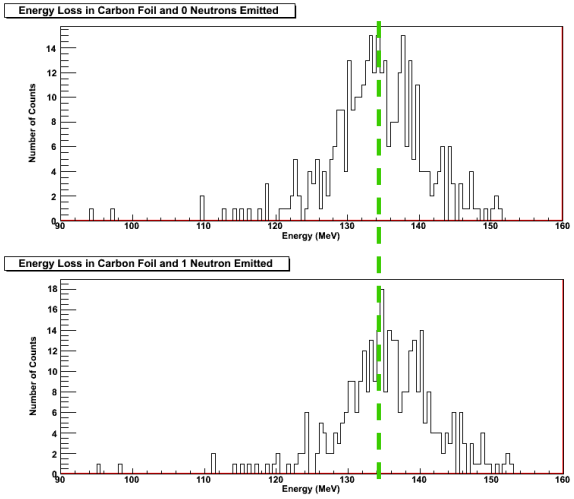

(c) TKE

Figure 4.12: Comparison between (a) mass (after neutron emission), (b) energy and (c) total kinetic energy distribution when no and one neutron is emitted and when the energy loss in the carbon foil is taken into account, for the spectra of both detectors together.

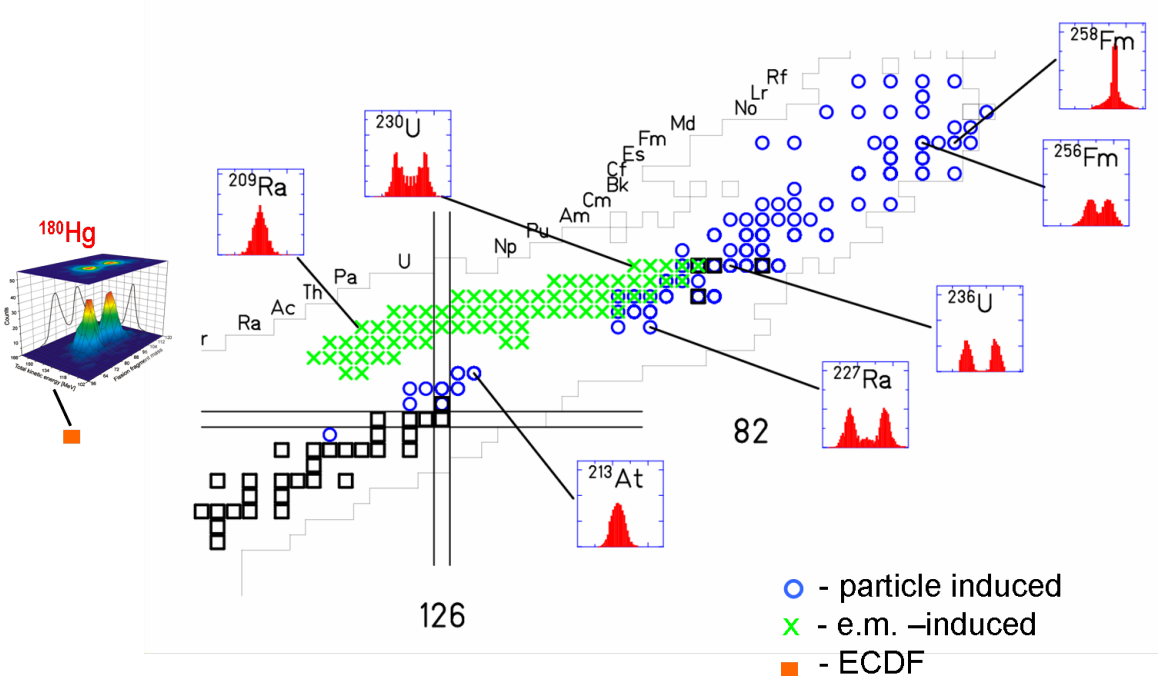

Figure 4.13: Mass distributions for different low energy fissioning nuclei [Col07].

and heavy fragment respectively. The Coulomb repulsion between the fragments is then given by

$$E_C = \frac{Z_L Z_H e^2}{4\pi\epsilon_0 R_0 (A_L^{1/3} + A_H^{1/3})}$$

where ϵ_0 is the permittivity of free space. Now, imagine symmetric fission, $Z_L = Z_H = Z/2$ and $A_L = A_H = A/2$, then $E_C \sim Z^2/A^{1/3}$, with Z and A of the fissioning nucleus. This Coulomb repulsion energy will be fully converted to kinetic energy when the fragments are infinitely far apart, and this shows that indeed a relation between $\langle E_k \rangle$ and the Coulomb parameter is expected. However, inserting numerical values and taking $R_0 = 1.2$ fm too high values for the Coulomb repulsion E_C are obtained compared to the measured TKE. This is due to the simplicity of the assumed model. In reality, the fission fragments are deformed and are joined by a thin neck (see Fig. 1.6(a)). The deformation and larger separation will decrease the Coulomb repulsion [Wag91].

Viola et al. determined a linear relationship between the average TKE and the Coulomb parameter for the first time in 1966. However, about 20 years later, many new data of fissioning systems were known and Viola et al. adjusted their original equation to [Vio85]

$$\langle E_k \rangle = (0.1189 \pm 0.0011) Z^2/A^{1/3} + 7.3(\pm 1.5) \text{ MeV} \tag{4.14}$$

This relation of $\langle E_k \rangle$ as a function of $Z^2/A^{1/3}$ is called a Viola-plot and is shown in Fig. 4.14, together with the calculated average value of the TKE of the fission fragments of ^{180}Hg, deduced in the current work. Equation (4.14) predicts a value of $\langle E_k \rangle = (142.1 \pm 2.8)$ MeV. The measured mean value of $\langle E_k \rangle = (134.6 \pm 0.7)$ MeV is in agreement with the Viola-plot within two standard deviations σ. Hence, with the current low

statistics it cannot be stated that the TKE does not follow the Viola-plot.

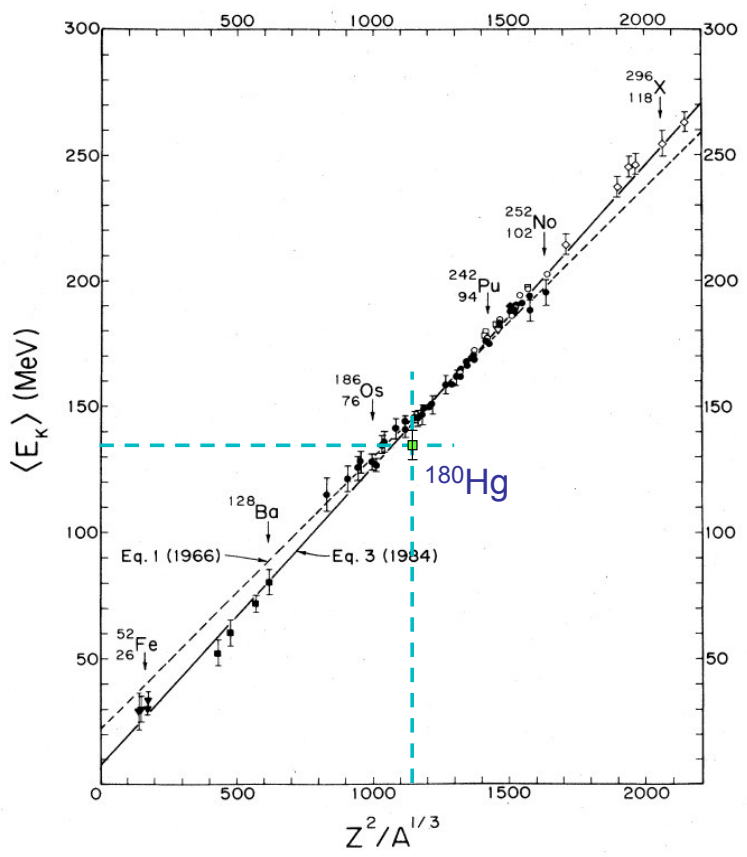

Figure 4.14: Average total kinetic energy, $\langle E_k \rangle$, as a function of $Z^2/A^{1/3}$ of the fissioning nucleus [Vio85]. The dashed line gives the linear equation from 1966, the solid line the adjusted equation (eq. (4.14)) from 1984 (see the text for details).

Several considerations led to the conclusion that it cannot be excluded that one neutron can be emitted in the fission of ^{180}Hg. If it is assumed that one neutron is emitted, the total kinetic energy increases to (135.7 ± 0.8) MeV. Nevertheless, it is not possible to make a clear distinction between the cases were no and one neutron is emitted. The mass distribution does not change noticeably when one neutron is emitted. Also the total kinetic energy is still in agreement, within error bars, with the result when no neutrons are emitted.

Chapter 5

Determination of Half-Life and Branching Ratios

In this chapter the half-life of ^{180}Tl will be deduced, both from the α decay of ^{180}Tl as from the fission of ^{180}Hg, after EC of ^{180}Tl. Further, the branching ratio for the electron capture of ^{180}Tl will be determined. Finally, the ECDF probability P_{ECDF} is calculated.

5.1 Half-Life of ^{180}Tl

The half-life $t_{1/2}$ can be deduced from the growth and decay curves (see e.g. Fig. 3.6). As mentioned in section 3.2.1, the ^{180}Tl nuclei are implanted for about 2.4 s (the growth curve). 1.2 s after the second proton pulse is arrived the mass separator is closed and thus the implantation of nuclei stops. After the mass separator is closed, a radioactive decay will follow (the decay curve) without the complication of simultaneous implantation, until new nuclei are implanted. From this decay, it is quite easy to determine the half-life. Assume that at time t there are N ^{180}Tl nuclei present, which will decay in time. The number of nuclei dN decaying in a time dt is proportional to N

$$\frac{dN}{dt} = -\lambda N$$

where λ is the decay constant. Integrating this equation leads to the *exponential law of radioactive decay*

$$N(t) = N_0 e^{-\lambda t} \tag{5.1}$$

where N_0 is the number of nuclei present at time $t = 0$. The decay constant λ can be related to the *mean life time* τ of the nuclei, according to

$$\tau = \frac{1}{\lambda}$$

The half-life $t_{1/2}$ gives the time at which half of the nuclei have decayed. Thus setting $N(t) = N_0/2$, this gives $t_{1/2} = \frac{ln(2)}{\lambda}$ or

$$N(t) = N_0 e^{-\ln(2)t/t_{1/2}} \tag{5.2}$$

This equation can be used to fit the decay curve and as such the half-life can be determined [Kra88].

It is very difficult to include the growth curve in this equation, since due to the diffusion, effusion and ionization processes in the target-ion source it is hard to model the time behavior of the implantation of the Tl nuclei. Furthermore, during the implantation also decay of ^{180}Tl will already occur. This makes it very challenging to determine an equation that can model the growth curve. Therefore, in this thesis only the decay curve was used to determine the half-life, which is not a problem if the statistics are high.

5.1.1 Half-Life of ^{180}Tl from Alpha Decay

To be able to fit the decay curve in a reliable manner, the decay needs to proceed over several half-lives, thus there has to be a long enough period between two consecutive implantation periods. Therefore, with an idea to deduce the half-life of ^{180}Tl, $t_{1/2}(^{180}Tl)$, the proton pulses 2-3 and 10-11 were given for a time of about 11.5 hours during the experiment. With this proton sequence the time between two proton bunches (each consisting of two proton pulses) is 8.4 s, and the decay curve will then occur over 7.2 s, which is a long enough time to let the major part of the Tl nuclei decay before the next implantation period (see Fig. 3.6). Therefore, only the data containing this sequence of pulses are used do determine the half-life.

Fig. 5.1 shows the α-spectrum of ^{180}Tl and its products. The α-peaks are indicated by the energy and isotope. These nuclei result from a decay chain that starts with ^{180}Tl, see Fig.1.3. The four α-lines of ^{180}Tl have an energy of E_α = 6.21, 6.26, 6.35 and 6.55 MeV.

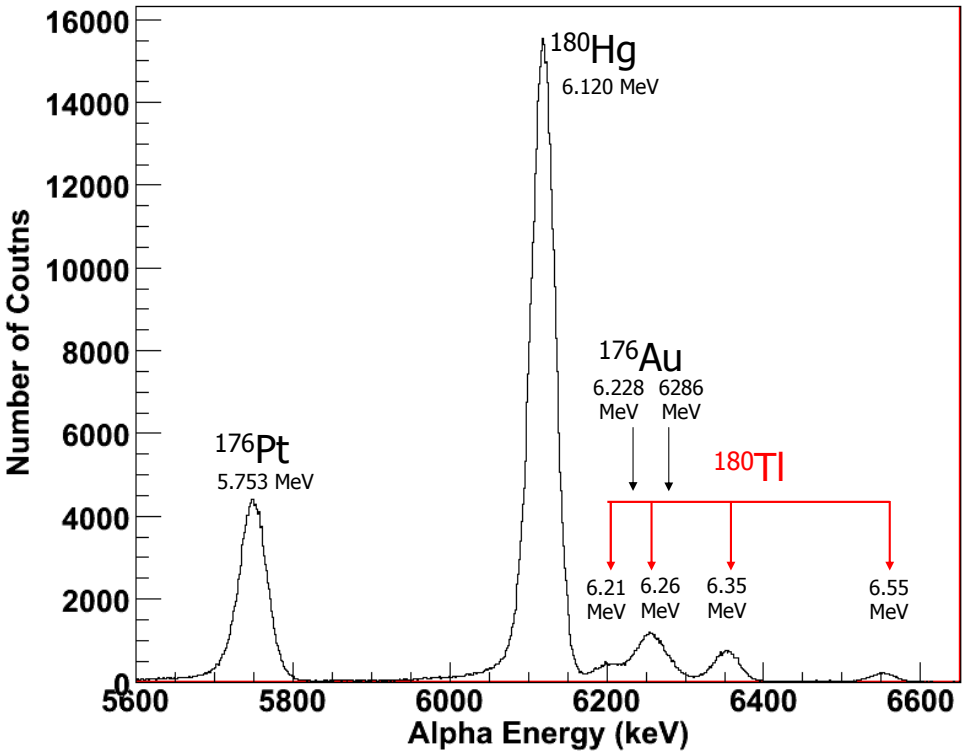

Figure 5.1: Alpha spectrum resulting from the decay chain that starts with ^{180}Tl.

To determine the half-life of ^{180}Tl, the decay curve for every α-line separately will be fitted with equation (5.2). All these half-lives should be the same, unless the α decay happens from two different isomers.

An example of the fitted decay curve for E_α = 6.35 MeV is shown in Fig. 5.2. The fit will start after 3.6 s for the first and after 13.2 s for the second decay curve, because after these times the implantation stops and the decay curve of ^{180}Tl starts. Since two decay curves can be fitted for one α-line, in total eight measurements for the half-life are possible. The calculated half-lives for the different alpha energies are shown in Table 5.1.

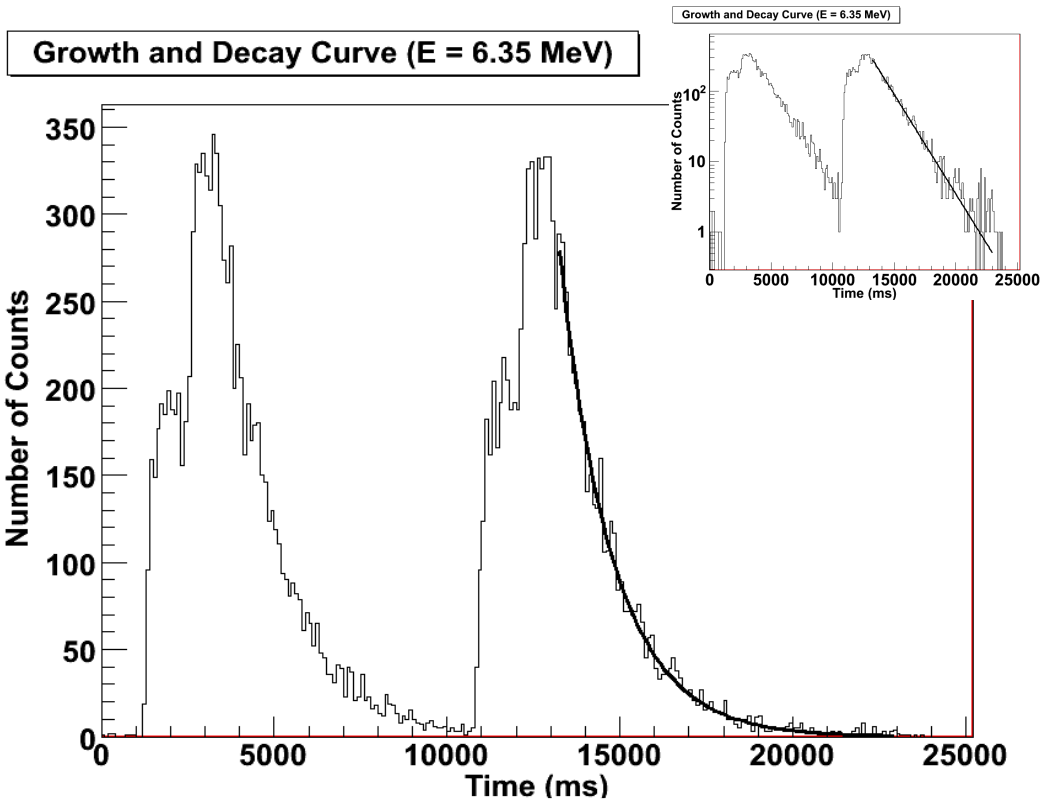

Figure 5.2: Growth and decay curve for E_α = 6.35 MeV of the decay of ^{180}Tl. The second decay curve is fitted with equation (5.2). In the inset the same figure is shown on log-scale.

All these half lives are, within error bars, in agreement with each other, except for the half-lives deduced for the α-line of energy E_α = 6.26 MeV. However, by looking at Fig. 5.1, it is noticed that this α-line has a contribution due to ^{176}Au. If this contribution is significant, it will influence the measured half-life of this α-line. Therefore, the ^{176}Au contamination to this α-peak has to be eliminated. Since only ^{180}Tl has α-γ-coincidences [Anda], this can be done by looking at an α-γ-coincidence spectrum, which is shown in Fig. 5.3. This figure shows that the α-particle of energy E_α = 6.26 MeV, should for example be in coincidence with the γ-rays of energy E_γ = 205, 210 keV. These coincidences can be used to deduce the correct half-life of this α-line. Namely, by fitting the decay curves for the alpha particle E_α = 6.26 MeV again, but now with the extra condition that it should be coincident with γ-rays, the correct half-life for this alpha particle could be obtained. Indeed, the new half-life for the two decay curves now reads $t_{1/2}$ = (1.10 $\pm$ 0.06) s, when

E_α (MeV)	Half-Life $t_{1/2}$ (s)
6.21 ± 0.03	1.14 ± 0.08
	1.15 ± 0.10
6.26 ± 0.02	1.42 ± 0.04
	1.37 ± 0.03
6.35 ± 0.02	1.10 ± 0.02
	1.07 ± 0.02
6.55 ± 0.02	1.02 ± 0.05
	1.04 ± 0.04

Table 5.1: Half-lives deduced from the fits of the decay curves of the different α-lines of ^{180}Tl.

both curves are fitted together (see below). This is in excellent agreement with the half-lives obtained for the other α-particles of ^{180}Tl.

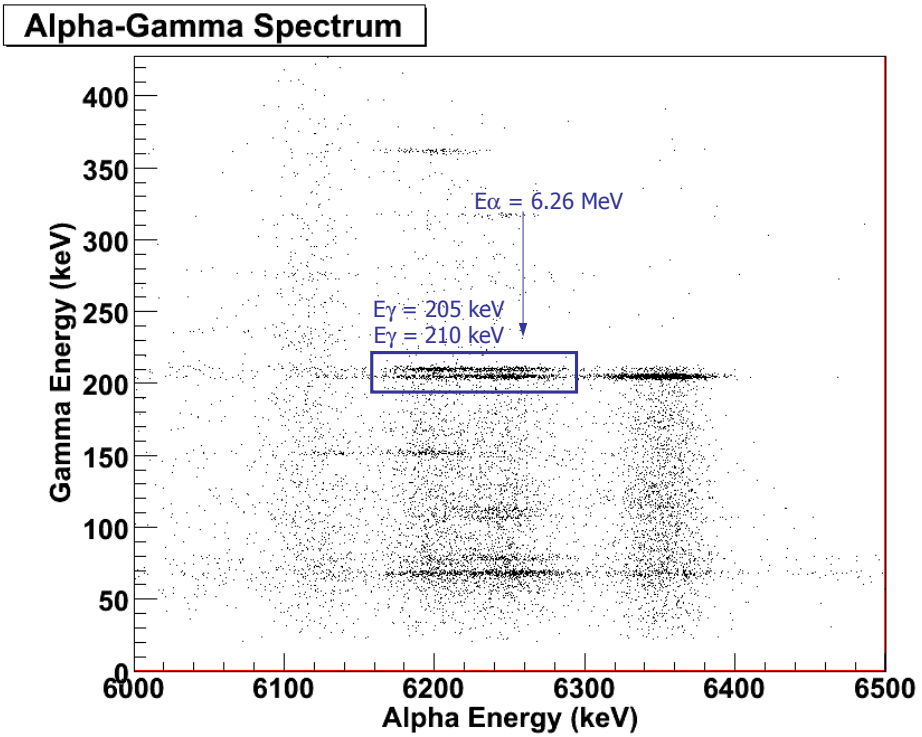

Figure 5.3: α-γ spectrum, for α-energies in the range of the α-particles resulting from the decay of ^{180}Tl.

Further, Table 5.1 shows that the error on the half-life of the α-line at $E_\alpha = 6.21$ MeV is larger than that of the other half-lives. As can be seen from Fig. 5.1 this α-line is not a distinct line, which will result in the larger error on the half-life, and it could also have

a small contribution due to ^{176}Au.

It is also possible to fit both decay curves in Fig. 5.2 simultaneously, as to increase the statistics. This possibility to increase the statistics will be important when the half-life of ^{180}Tl will be deduced from the ECDF process in the following section. An example using this method is shown in Fig. 5.4 for the α-particle of energy $E_\alpha = 6.35$ MeV. The resultant half-life is $t_{1/2} = (1.08 \pm 0.01)$ s, which is in very good agreement with the half-lives obtained above and the larger statistics result in a smaller error bar.

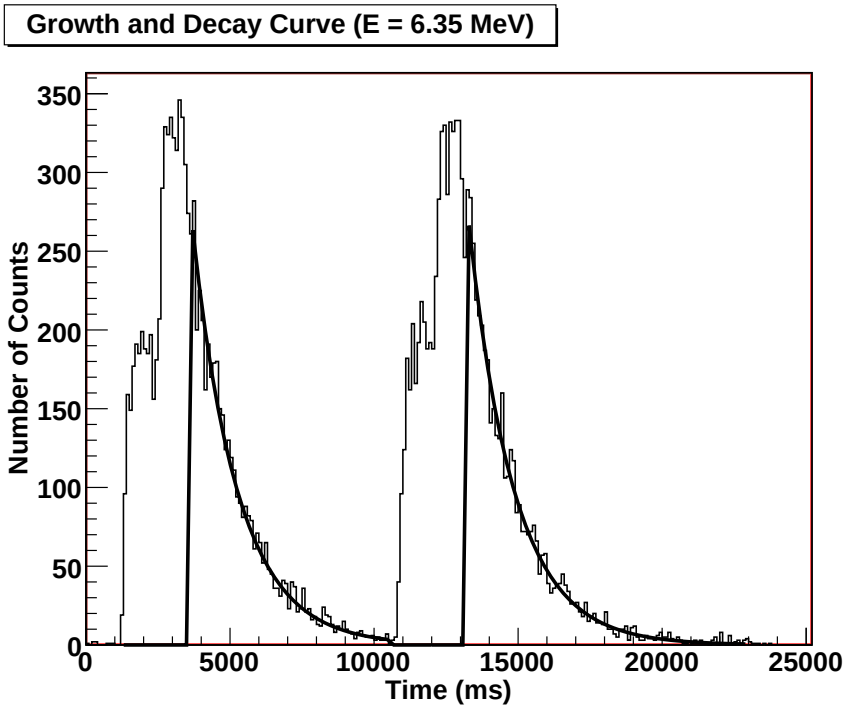

Figure 5.4: Growth and Decay curve for $E_\alpha = 6.35$ MeV, where both decay curves are fitted simultaneously with equation (5.2).

Still another way to determine the half-life is by shifting the different decay curves in time, so that the position (in time) of the implantation cycle is the same. The different decay curves then overlap onto one curve, and in this way the statistics are increased. An example of this method is shown in Fig. 5.5 for the α-line $E_\alpha = 6.35$ MeV. The calculated half-life gives the same value as before, as it should, $t_{1/2} = (1.09 \pm 0.01)$ s.

To conclude this section, the half-life of ^{180}Tl according to the α decay is equal to

$$t_{1/2} = (1.09 \pm 0.01) \text{ s}$$

and the α decay of ^{180}Tl does not happen from different isomeric states. This deduced half-life can be compared to previously reported measurements in literature. Two measured values for the half-life of ^{180}Tl can be found: $t_{1/2} = 0.7^{+0.12}_{-0.9}$ s [Laz87] and $t_{1/2} = (1.5 \pm 0.2)$ s [Tot98]. The average of this two values is in good agreement with the deduced half-life in the present work.

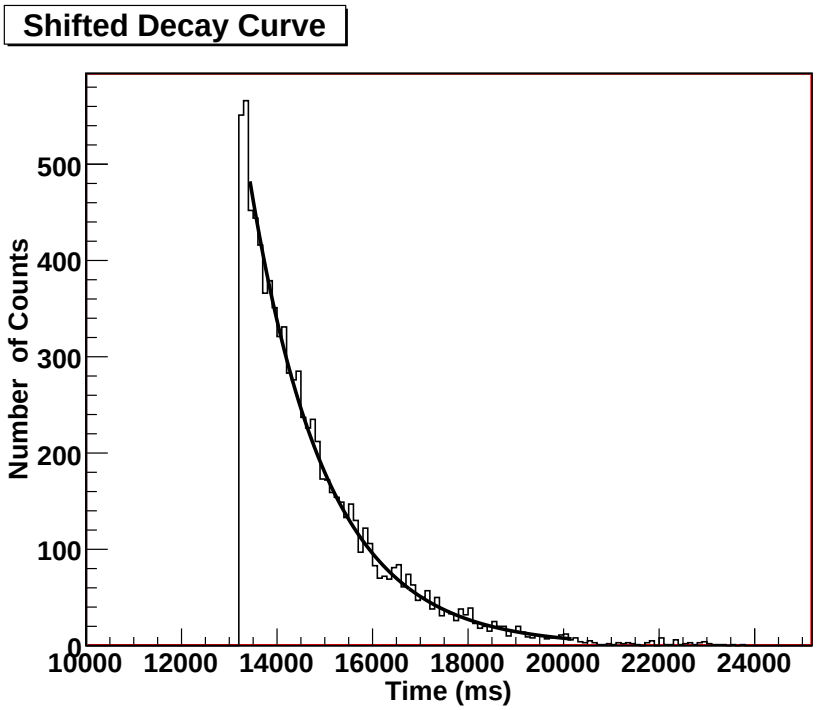

Figure 5.5: Decay curve of $E_\alpha = 6.35$ MeV, where the original two decay curves are shifted onto one curve.

5.1.2 Half-Life of ^{180}Tl from ECDF

Since the fission of ^{180}Hg, after the EC decay of ^{180}Tl, can be regarded as instantaneous ($t_{1/2} \lesssim 10^{-15}$ s), this fission can also be used to determine the half-life of ^{180}Tl. The same methods as described for the α decay can be used here, however the statistics will be much lower. Indeed, in the data that contain the pulses 2-3 and 10-11 only 52 fission fragments were detected, and by considering only the decay curve only nine fission events remain. Of this nine detected fragments, three were measured in coincidence. These coincident fragments can of course be counted only once in the determination of the half-life, thus in fact only six fissions remain. Hence, it is not possible to fit these decay curves. Nevertheless, these six fissions can be used to determine the mean life time of ^{180}Tl, by using

$$\tau = \frac{\sum^n t_i}{n}$$

where t_i is the life time of one fission event. The error bars can be calculated according to [Sch84] as follows

$$\tau_u \approx \frac{\tau}{1 - 1/\sqrt{n}}$$

$$\tau_l \approx \frac{\tau}{1 + 1/\sqrt{n}}$$

where τ_u is the upper and τ_l lower limit. For the six fission events this leads to

$$\tau = 1.44^{+2.43}_{-1.02} s$$

The error bars are still very large, due to the very low statistics. This life time can be used to calculate the half-life

$$t_{1/2} = \ln(2) \cdot \tau = 1.00^{+1.68}_{-0.71} s$$

Even though the very low statistics, this agrees well with the result obtained for the α decay. This indicates that, within the current low statistics, the state in ^{180}Tl that feeds the fissioning state in ^{180}Hg is the same as the one that undergoes the α decay, and thus that only one isomer of ^{180}Tl is involved.

However, it would be better to increase the statistics of the fission events. This can be done by considering other data. To be able to construct the growth and decay curves, it is important that the data have the same time structure. The first 34.5 hours of the experiment the proton pulses 4-5, 8-9, 12-13 and 16-17 were received. This longer time of the total measurement will increase the statistics significantly, however the shorter time between the consecutive proton bunches, decreases the time in which the decay of ^{180}Tl is observed. This will limit the accuracy of the fit. For these data in total 270 fissions were observed out of which only 126 in the decay curve.

To achieve the highest possible statistics, the four decay curves are shifted onto one curve. The result is shown in Fig. 5.6 for two different binnings of the spectra. Fig. 5.6(a) has a binning of 100 ms per bin, while Fig. 5.6(b) 200 ms per bin. In the case of low statistics it sometimes helps to change to a larger binning. The deduced half-lives are $t_{1/2} = (0.88 \pm 0.20)$ s for Fig. 5.6(a) and $t_{1/2} = (1.04 \pm 0.28)$ s for Fig. 5.6(b). Both values are in good agreement with the half-life deduced from the α decay of ^{180}Tl. Hence, it can be concluded, that, within the current precision, the α decay and the electron capture that feeds the fissioning state in ^{180}Hg arise from the same isomer in ^{180}Tl.

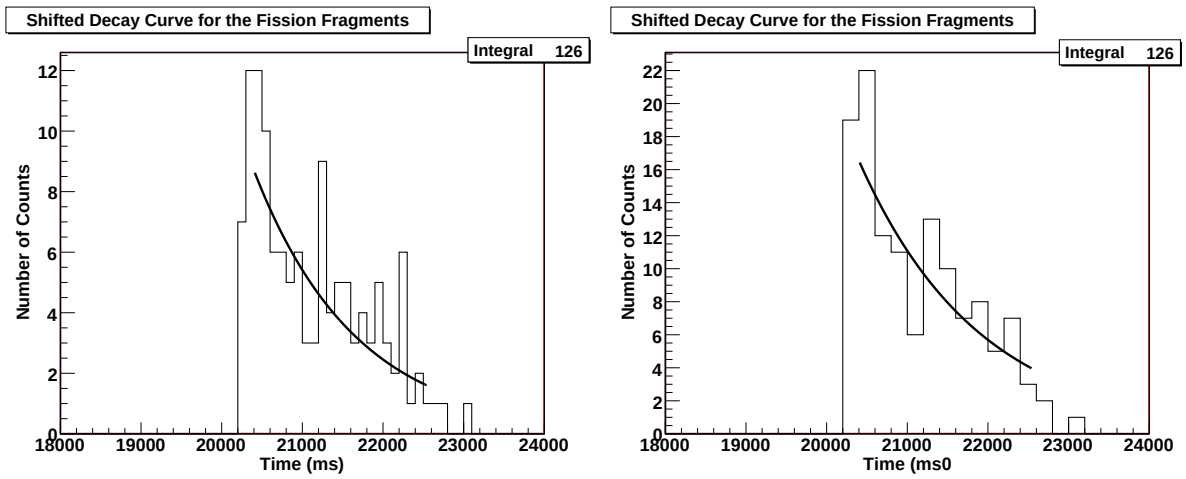

(a) (b)

Figure 5.6: Decay curves, shifted in time, for the fissions of ^{180}Hg detected during the first 34.5 hours of the experiment, for a binning of (a) 100 ms per bin and (b) 200 ms per bin.

5.2 Electron Capture Branching Ratio of ^{180}Tl

The electron capture branching ratio of ^{180}Tl, $b_{EC}(^{180}Tl)$, can easily be deduced from the α decay branching ratio $b_\alpha(^{180}Tl)$:

$$b_{EC}(^{180}Tl) = 1 - b_\alpha(^{180}Tl) \tag{5.3}$$

with

$$b_\alpha(^{180}Tl) = \frac{N_\alpha(^{180}Tl)}{N_\alpha(^{180}Tl) + N_{EC}(^{180}Tl)}, \tag{5.4}$$

where e.g. $N_\alpha(^{180}Tl)$ is the number of Tl nuclei that decayed through α decay. The number of Tl nuclei that decay through EC, $N_{EC}(^{180}Tl)$, can be related to the total number of ^{180}Hg nuclei, $N(^{180}Hg)_{tot}$. Since there is no direct production of ^{180}Hg in the current experiment, which was checked by comparing laser-on and laser-off measurements, $N_{EC}(^{180}Tl)$ is equal to the total number of Hg nuclei that is produced (see also Fig.1.3). The total number of ^{180}Hg nuclei can be calculated if the total number of α-particles due to the decay of ^{180}Hg, $N_\alpha(^{180}Hg)$, can be deduced, through

$$N_{EC}(^{180}Tl) = N(^{180}Hg)_{tot} = \frac{N_\alpha(^{180}Hg)}{b_\alpha(^{180}Hg)}$$

where the branching ratio $b_\alpha(^{180}Hg) = (48 \pm 2)\%$ [ENS08]. The α decay branching ratio $b_\alpha(^{180}Tl)$ can then be written as:

$$b_\alpha(^{180}Tl) = \frac{N_\alpha(^{180}Tl)}{N_\alpha(^{180}Tl) + \frac{N_\alpha(^{180}Hg)}{b_\alpha(^{180}Hg)}} \tag{5.5}$$

Approximate values for $N_\alpha(^{180}Tl)$ and $N_\alpha(^{180}Hg)$ are $\approx 10^5$ and $\approx 5\times10^5$, respectively. From these values it can be seen that the error on the branching ratio $b_\alpha(^{180}Tl)$ will be dominated by the error on $b_\alpha(^{180}Hg) = (48 \pm 2)\%$, which is about 4%.

By again considering only the data that contain the pulses 2-3 and 10-11, all the necessary values to determine $b_\alpha(^{180}Tl)$ can be deduced from Fig. 5.1, by just calculating the number of counts (*integrals*) in the different α-lines. This will however result in an upper limit for $b_\alpha(^{180}Tl)$. First of all the α-peak at 6.26 MeV of ^{180}Tl contains a contamination due to ^{176}Au and hence the true number of α-particles coming from the decay of ^{180}Tl in that α-peak will be lower. Secondly, not all the Hg nuclei will have decayed by the time the windmill is rotated, due to the longer half-life of 2.56 s. This can be seen in Fig. 5.7, where it is shown that the second decay curve of the Hg nuclei does not fall back to zero after the supercycle has ended. The correct number of α-particles coming from the decay of Hg will therefore be higher. Correcting the branching ratio $b_\alpha(^{180}Tl)$ for these contributions will lower its value.

To find the correction for the Hg nuclei, it is necessary to estimate the total number of α-particles that would be counted when Hg fully decayed. Thus the number of 'missing' α-particles has to be found. This can be done by fitting the growth and decay curve in Fig. 5.7.

Notice first that it can be assumed that the Hg nuclei that are the result of the decay of ^{180}Tl that was produced with the proton pulses 2-3, have fully decayed by the time the

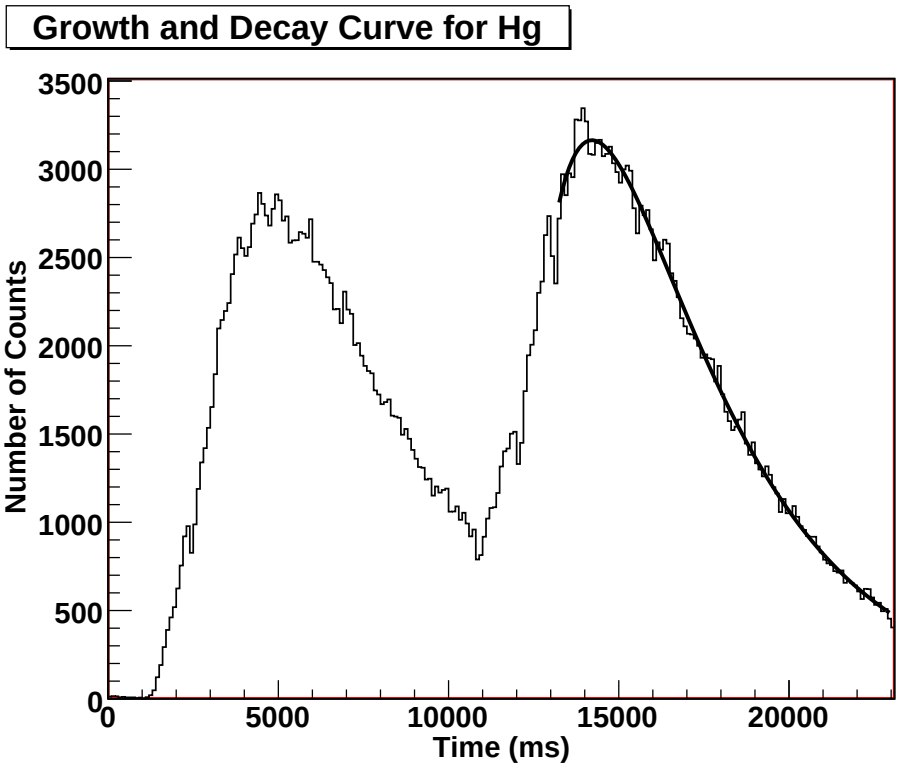

Figure 5.7: Growth and decay curve for the α decay of ^{180}Hg, fitted with equation (5.6).

windmill is rotated. The Hg nuclei resulting from proton pulses 10-11 however, have not all decayed after one supercycle.

The equation to fit the growth and decay curve of ^{180}Hg will be more complicated than equation (5.2). Since the Hg nuclei are produced through the decay of ^{180}Tl a *mother-daughter* decay has to be taken into account. To simplify the form of this mother-daughter decay equation, the time $t = 0$ s in the equation will be set at the time the second growth curve of ^{180}Tl has ended. This is thus at the beginning of the second decay curve of ^{180}Tl, namely after 13.2 s. If the mother-daughter equation only starts after the decay of ^{180}Tl starts, it can be assumed that no new Tl nuclei will be implanted. This means that at time $t = 0$ s in the equation, thus actually the real time minus 13.2 s, an initial number of Tl nuclei was present. Furthermore, Hg nuclei that were produced through the decay of ^{180}Tl resulting from the proton pulses 2-3 and in the second growth curve of ^{180}Tl will still be present when the second growth curve of ^{180}Hg starts. Therefore, also an exponential decay curve, equation (5.1), has to be taken into account. The resultant equation is the following

$$N_{Hg}(t) = \underbrace{\frac{\lambda_{Tl}}{\lambda_{Hg} - \lambda_{Tl}} N_{Tl}(e^{-\lambda_{Tl}t} - e^{-\lambda_{Hg}t})}_{\text{mother-daughter decay}} + \underbrace{N_{Hg}e^{-\lambda_{Hg}t}}_{\text{exponential decay}} \tag{5.6}$$

where N_{Hg} and N_{Tl} are the initial number of Hg and Tl nuclei at the end of the second growth curve of ^{180}Tl resulting from the pulses 10-11, after 13.2 s.

The fit using this equation is shown in Fig. 5.7. With the parameters from the fit

and equation (5.6) the number of missing α-particles can be estimated, by calculating the integral under the function (5.6) from $t = 0$ s to infinity. By comparing this number with the number of α-particles in the α-line of ^{180}Hg in Fig. 5.1, it can be calculated that a correction of $(4.1 \pm 0.4)\%$ is needed to find the total number of α-particles resulting from the decay of all the Hg nuclei. The integral of the α-peak of Hg in Fig. 5.1 thus has to multiplied by 1.041, to get the correct number of α-particles.

The correction for the contamination due to ^{176}Au is less straightforward or even impossible to calculate with the current data. The only possibility is to estimate an upper limit for the contribution of ^{176}Au, namely that the whole α-line at $E_\alpha = 6.26$ MeV is due to ^{176}Au. This will then result in a lower limit for the branching ratio $b_\alpha(^{180}Tl)$. It is also possible to assume that the ^{176}Au contamination is negligible, and hence that the α-line at $E_\alpha = 6.26$ MeV is fully due to ^{180}Tl, which will result in an upper limit for $b_\alpha(^{180}Tl)$. The calculated upper and lower limit for the branching ratios b_α and b_{EC} of ^{180}Tl are shown in Table 5.2.

b_{EC} (%)	b_α (%)
95.72 ± 0.17	4.28 ± 0.17
91.95 ± 0.31	8.05 ± 0.31

Table 5.2: Upper and lower limits for the branching ratios b_α and b_{EC} of ^{180}Tl.

By taking an average of the upper and lower limit of $b_{EC}(^{180}Tl)$ it can be stated that

$$b_{EC}(^{180}Tl) = (94 \pm 4)\%$$

The error on this value is larger than the errors given in Table 5.2. The errors in the table are calculated values, but since the error on $b_\alpha(^{180}Hg)$ is, as mentioned above, about 4%, the error on the calculated $b_{EC}(^{180}Tl)$ cannot be smaller.

This calculated branching ratio $b_{EC}(^{180}Tl)$ is in agreement with the estimation of $b_\alpha(^{180}Tl) = (2\text{-}12)\%$, or $b_{EC}(^{180}Tl) = (88\text{-}98\%)$, deduced in [And03].

5.3 ECDF Probability P_{ECDF}

The ECDF probability P_{ECDF} of ^{180}Tl is determined as the ratio of the number of fissions $N_{fission}$ to the total number of ^{180}Hg nuclei $N(^{180}Hg)_{tot}$

$$P_{ECDF} = \frac{N_{ECFD}}{N_{EC}} = \frac{N_{fission}}{N(^{180}Hg)_{tot}}$$

This is true, since, as noted above, the number of Tl nuclei that undergo electron capture N_{EC} equals the total number of Hg nuclei that is produced.

In the data containing the pulses 2-3 and 10-11 52 fragments resulting from the fission of ^{180}Hg were detected. However, 17 of these events were measured as coincident pairs, thus actually only 35 fissions happened. The resulting ECDF probability is then

$$P_{ECDF} = (3.6 \pm 0.7) \times 10^{-5} = (3.6 \pm 0.7) \times 10^{-3}\%$$

Due to the small number of fissions, the error bar on this branching ratio is still rather large. Therefore, it would be beneficial to include more data, as to obtain a larger statistics

on the number of fissions. To be able to estimate the number of 'missing' α-particles of ^{180}Hg it is again important that these data have the same time structure. Hence, again, as in section 5.1.2, the data that contain the pulses 4-5, 8-9, 12-13 and 16-17 would be good to use. In these data 270 fissions were observed. However, due to the much smaller decay time, fitting these growth and decay curves with equation (5.6) does not give good results. As a consequence, the errors on the parameters from the fit will be rather large, and although the higher statistics the error bar on P_{ECDF} will not decrease. Hence, it is not useful to use these other data.

It is now time to look again at Fig. 2.3, to see if the new value for the ECDF probability P_{ECDF} of ^{180}Tl fits the general trend of P_{ECDF} in function of Q_{EC}-B_f better than the previous value of $3 \times 10^{-7\pm1}$ [Laz87]. An adjusted figure, with the new P_{ECDF} value is shown in Fig 5.8. And indeed, the new value fits the general trend very well.

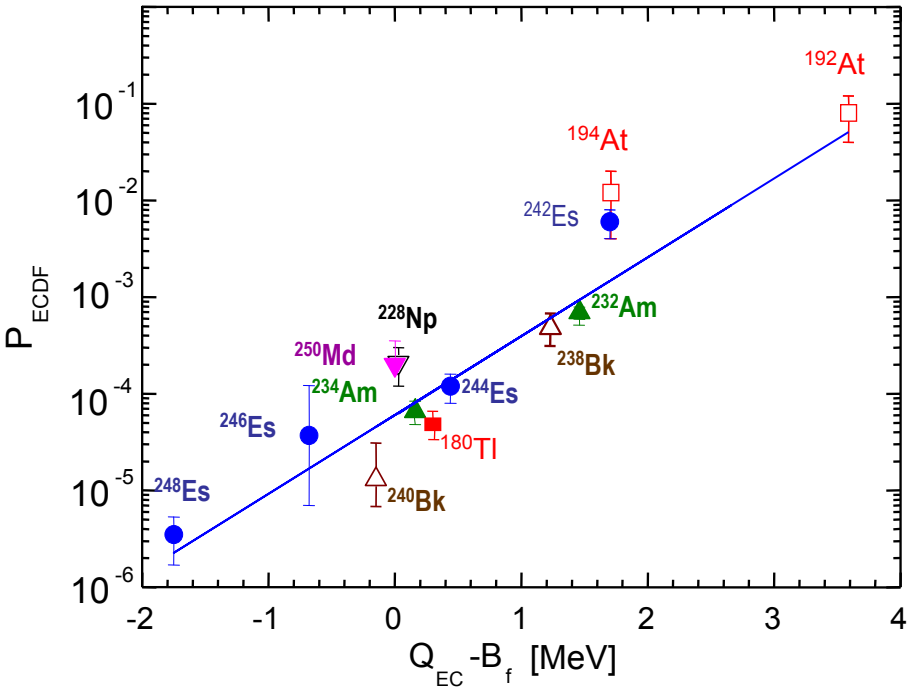

Figure 5.8: ECDF probability P_{ECDF} as a function of (Q_{EC}-B_f). The data are marked by the parent nuclei. The Q_{EC} values are taken from [Möl95] and the B_f values from [Mey99]. The newly deduced value for P_{ECDF} of ^{180}Tl is indicated by a red square.

Conclusion

This thesis concentrated on the radioactive decay properties of the very neutron deficient nucleus ^{180}Tl, which can undergo α-decay or electron capture, by which the nuclei ^{176}Au and ^{180}Hg are formed, respectively. The specific decay mode Electron Capture Delayed Fission (ECDF) was investigated in more details. In this decay process the nucleus of interest first undergoes an electron capture, whereby it populates an excited state in the daughter nucleus. If this state has an excitation energy comparable to or even higher than the fission barrier of the daughter, fission of the latter may occur.

The experiment was performed at the ISOLDE facility in CERN. To detect the radioactive decay of ^{180}Tl the windmill chamber was used, together with four silicon detectors, a Miniball Ge cluster and a planar low-energy X-ray detector.

The first part of the analysis consisted of constructing a mass and energy calibration for the fission fragments, using the Schmitt calibration method. This method assumes that the pulse height registered in the silicon detector due to an incoming heavy ion does not only depend on the energy of the ion, but also on its mass. Mass and energy distributions, together with the total kinetic energy of the fission of ^{180}Hg could then be determined. The surprising fact was that an asymmetric mass distribution was observed. Before the experiment it was thought that the mass distribution would be dominated by the N = 50 shell closure, which would lead to a symmetric mass distribution around the isotope ^{90}Zr. Instead, a mass distribution was deduced that was spread around the mass numbers $A_L = 80$ and $A_H = 100$. From the data of the current experiment, it was not possible to deduce the Z value of the fragments, however several considerations led to the estimation that the most probable resultant isotopes are ^{80}Kr and ^{100}Ru. The mean total kinetic energy was calculated to be (132.0 $\pm$ 0.7) MeV. This result however changes when the energy loss the fragments suffer when they pass through the carbon foil is taken into account. The mean total kinetic energy then increases to (134.6 $\pm$ 0.7) MeV. This result is in agreement with the Viola-plot, which shows the mean total kinetic energy as a function of the Coulomb parameter $Z^2/A^{1/3}$, within two standard deviations.

Several considerations led to the conclusion that it cannot be excluded that one neutron can be emitted in the fission of ^{180}Hg. There is no way however in the current experiment to determine if there are *any* neutrons emitted. The only possibility is to see how the previous results change when it is assumed that a neutron is emitted by one of the fragments. If one neutron is emitted the total kinetic energy further increases to (135.7 $\pm$ 0.8) MeV. Nevertheless, it is not possible to make a clear distinction between the cases when no and one neutron is emitted. The mass distribution does not change noticeably when one neutron is emitted. The total kinetic energy seems to increase, but even this is still in agreement within error bars, with the result when no neutrons are emitted.

In a second part the half-life $t_{1/2}$ of ^{180}Tl was determined from its α decay, and it

was found to be equal to $t_{1/2} = (1.09 \pm 0.01)$ s. Since the fission of ^{180}Hg, after electron capture of ^{180}Tl, can be treated as instantaneous, the ECDF process can also be used to deduce the half-life of ^{180}Tl. The calculated half life $t_{1/2} = (1.04 \pm 0.28)$ s is in agreement with the half-life of ^{180}Tl deduced from its α decay. Both values are in agreement, this suggests that, within the current precision, the α decay and the ECDF arise from the same isomer in ^{180}Tl.

The deduced half-life is approximately equal to the average of the two previously reported values in literature: $t_{1/2} = 0.7^{+0.12}_{-0.9}$ s [Laz87] and $t_{1/2} = (1.5 \pm 0.2)$ s [Tot98].

Finally, the electron capture branching ratio b_{EC} of ^{180}Tl and the ECDF decay probability P_{ECDF} were deduced. The deduced electron capture branching ratio is equal to $b_{EC} = (94 \pm 4)\%$, which is in good agreement with the value of (88-98)% previously estimated by [And03].

The calculated ECDF decay probability equals $P_{ECDF} = (3.6 \pm 0.7)\times10^{-5}$. This value is two orders of magnitude higher than the previous reported value of $3 \times 10^{-7\pm1}$ by [Laz87], and fits the general trend of P_{ECDF} as a function of Q_{EC}-B_f, observed for the other known nuclei that can undergo ECDF, very well.

It would be very interesting to extend the study of the electron capture delayed fission to other nuclei in the Pb region. From these measurements, general features of the beta delayed fission could be deduced, which could be used in r-process calculations. Also, it would be interesting to further investigate how for example the fission barrier behaves outside the beta stability line. Two new experiments concerning the ECDF process are already approved.

Bibliography

[Aer06] C. Aerts. *Sterrenkunde*. Katholieke Universiteit Leuven, Faculteit Wetenschappen, 2006.

[Anda] A.N. Andreyev. private communication.

[Andb] A.N. Andreyev et al. To be published.

[And03] A.N. Andreyev et al. *Eur. Phys. J. A*, 18 (2003) 55.

[Ant] S. Antalic. private communication.

[Ber69] E.Ye. Berlovich and Yu.N. Novikov. *Phys. Lett.*, 29B (1969) 155.

[Can09] Canberra. `http://www.canberra.com`, 2009.

[Cas90] R. F. Casten. *Nuclear Structure from a Simple Perspective*. Oxford University Press, 1990.

[Coc] T.E. Cocolios. private communication.

[Col07] Collaboration for High-Accuracy Experiments on Nuclear Reaction Mechanisms with Magnetic Spectrometers. `http://www-wnt.gsi.de/charms/exp.htm`, 2007.

[Cow91] J.J. Cowan, F.K. Thielemann, and J.W. Truran. *Phys. Rep.*, 208 (1991) 267.

[Cow04] J. J. Cowan and F.K. Thielemann. *Phys. Today*, 57 (2004) 47.

[Den92] P. Dendooven. *Reflektieassymmetrie in het Actinidegebied: α-Vervalstudies met behulp van de Ionengeleidertechniek*. PhD thesis, University of Leuven, Faculteit Wetenschappen, 1992.

[Dir07] J. Diriken. *Coulombexcitatiemetingen van neutronrijke koperisotopen*. Master's thesis, University of Leuven, Faculteit Wetenschappen, 2007.

[Ebe01] J. Eberth et al. *Progr. Part. Nucl. Phys.*, 46 (2001) 389.

[ENS08] ENSDF-Evaluated Nuclear Structure Data File. `http://www.nndc.bnl.gov/useroutput/AR_240346_1.html`, 2008.

[Fed00] V.N. Fedoseyev et al. *Hyperfine Interactions*, 127 (2000) 409.

[Fed03] V.N. Fedoseyev et al. *Nucl. Instr. Meth. B*, 204 (2003) 353.

[Fir99] R.B. Firestone, V.S. Shirley, C.M. Baglin, S.Y.F. Chu, and J. Zipkin. *Table of Isotopes*. John Wiley & Sons, 1999.

[Fly72] K.F. Flynn, E.P. Horwitz, C.A.A. Bloomquist, R.F. Barnes, R.K. Sjoblom, P.R. Fields, and L.E. Glendenin. *Phys. Rev. C*, 5 (1972) 1725.

[Gal83] D. Galeriu. *J. Phys. G: Nucl. Phys.*, 9 (1983) 309.

[Gan80] Yu.P. Gangrskii et al. *Yad. Fiz.*, 31 (1980) 307.

[Hal90a] H.L. Hall et al. *Phys. Rev. C*, 41 (1990) 618.

[Hal90b] H.L. Hall et al. *Phys. Rev. C*, 42 (1990) 1480.

[Hen81] H. Henschel, A. Kohnle, H. Hipp, and G. Gönnenwein. *Nucl. Instr. Meth.*, 190 (1981) 125.

[Hey90] K.L.G. Heyde. *The nuclear shell model*. Springer-Verlag, 1990.

[IKS09] IKS website. `http://fys.kuleuven.be/iks/`, 2009.

[ISO09] ISOLDE website. `http://isolde.web.cern.ch/isolde/`, 2009.

[Kno00] G.F. Knoll. *Radiation Detection and Measurement*. John Wiley & Sons, 2000.

[Kra88] K.S. Krane. *Introductory Nuclear Physics*. John Wiley & Sons, 1988.

[Kre94a] S.A. Kreek et al. *Phys. Rev. C*, 49 (1994) 1859.

[Kre94b] S.A. Kreek et al. *Phys. Rev. C*, 50 (1994) 2288.

[Kug00] E. Kugler. *Hyperfine Interactions*, 129 (2000) 23.

[Kuz66] V.I. Kuznetzov and N.K. Skobelev. *Yadernaya Fizika*, 4 (1966) 279.

[Laz87] Yu.A. Lazarev, Yu.Ts. Oganessian, I.V. Shirokovsky, S.P. Tretyakova, V.K. Utyonkov, and G.V. Buklanov. *Europhys. Lett.*, 4 (1987) 893.

[Mey99] W.D. Meyers and W. Swiatecki. *Phys. Rev. C*, 60 (1999) 014606.

[MIN09] MINIBALL website. `http://www.miniball.york.ac.uk/`, 2009.

[Möl95] P. Möller, J.R. Nix, W.D. Myers, and W. Swiatecki. *At. Data and Nucl. Data Tables*, 59 (1995) 185.

[Möl08a] P. Möller, 2008. private communication.

[Möl08b] P. Möller, 2008. submitted to Phys. Rev. C.

[Nor09] Northern Arizona University. `http://www4.nau.edu/meteorite/Meteorite/Images/Rprocess.jpg`, 2009.

[Ort09] Ortec. `http.//www.ortec-online.com`, 2009.

[Pan05] I.V. Panov, E. Kolbe, B. Pfeiffer, T. Rauscher, K.L. Kratz, and F.K. Thielemann. *Nucl. Phys. A*, 747 (2005) 633.

[Ref06] Reference Input Parameter Library. `http://www-nds.iaea.org/ripl-2/`, 2006.

[ROO09] ROOT website. `http://root.cern.ch/root/`, 2009.

[Sch65] H.W. Schmitt, W.E. Kiker, and C.W. Williams. *Phys. Rev.*, 137 (1965) B837.

[Sch66] H.W. Schmitt, J.H. Neiler, and F.J. Walter. *Phys. Rev.*, 141 (1966) 1146.

[Sch84] K.H. Schmidt, C.C. Sahm, K. Pielenz, and H.G. Clerc. *Z. Phys. A - Atoms and Nuclei*, 316 (1984) 19.

[Sha00] D.A. Shaughnessy et al. *Phys. Rev. C*, 61 (2000) 044609.

[Sha01] D.A. Shaughnessy et al. *Phys. Rev. C*, 63 (2001) 037603.

[Sha02] D.A. Shaughnessy et al. *Phys. Rev. C*, 65 (2002) 024612.

[SRI08] SRIM-The Stopping and Range of Ions in Matter. `http://www.srim.org/SRIM/SRIM2008.htm`, 2008.

[Sta90] A. Staudt, M. Hirsch, K. Muto, and H.V. Klapdor-Kleingrothaus. *Phys. Rev. Lett.*, 65 (1990) 1543.

[Ter62] J. Terrell. *Phys. Rev.*, 127 (1962) 880.

[Tot98] K.S. Toth et al. *Phys. Rev. C*, 58 (1998) 1310.

[vdW06] J. van de Walle. *Coulomb excitation of neutron rich Zn isotopes.* PhD thesis, University of Leuven, Faculteit Wetenschappen, 2006.

[Vio85] V.E. Viola, K. Kwiatkowski, and M. Walker. *Phys. Rev. C*, 31 (1985) 1550.

[Wag91] C. Wagemans. *The Nuclear Fission Process.* CRC Press, 1991.

[War00] W.K. Warburton, M. Momayezi, B. Hubbard-Nelson, and W. Skulski. *Applied Radiation and Isotopes*, 53 (2000) 913.

[Wei86] E. Weissenberger, P. Geltenbort, A. Oed, F. Gönnenwein, and H. Faust. *Nucl. Instr. Meth. A*, 248 (1986) 506.

[X-r09] X-ray Instruments Associates. `http://www.xia.com`, 2009.